UNIVERSITÀ
DEGLI STUDI
DI PADOVA

Administrative unit: **University of Padova**

Department: **Land, Environment, Agriculture and Forestry (LEAF)**

_____

PhD Program: **Land, Environment, Resources and Health (LERH)**

Batch: **XXX**

Analysis and modelling of surface runoff triggering debris flows

PhD Program Coordinator: Prof. Davide Matteo Pettenella

Supervisor: Dr. Carlo Gregoretti

PhD candidate: Martino Bernard

Sede Amministrativa: **Università degli Studi di Padova**

Dipartimento: **Territorio e Sistemi Agro-Forestali (TESAF)**

Corso di Dottorato di Ricerca: **Territorio, Ambiente, Risorse e Salute (TARS)**

Ciclo: **XXX**

Analysis and modelling of surface runoff triggering debris flows

Coordinatore: Prof. Davide Matteo Pettenella

Supervisore: Dr. Carlo Gregoretti

Dottorando: Martino Bernard

Abstract

In the Dolomites, short-duration and high-intensity rainfalls produce abundant surface runoff in headwater catchments. These discharges often trigger debris flows on the scree slopes placed at the base of rock cliffs. With the aim to quantify the discharges delivered by these headwater catchments and associated rainfalls, we built a measuring facility at the outlet (elevation 1770 m a.s.l.) of a rocky channel incised on the Dimai Peak, near Cortina d'Ampezzo (Belluno province) in the Venetian Dolomites (North Eastern Italian Alps). The channel delivers surface runoff gathered by a small impervious headwater catchment (area $\sim$ 0.032 km^2, average slope $\sim$ 320 %). The facility consists of a monitoring station equipped with a rain gauge, and trapezoidal-shape waterproof basin, closed by a sharp-crested weir. The recorded rainfalls allow us to verify the features that lead to runoff discharges or mass transport events. In the period 2011-2017, among the measured discharges, about fifteen runoff events were considered as significant. These observations provide a unique opportunity for improving knowledge about the hydrological response of a rocky headwater catchment. The recorded hydrographs show impulsive shapes, with a sudden raise up to the discharge peak, generally followed by a likewise rapidly decreasing tail. Furthermore, the discharges can be used to calibrate and validate hydrological models. We show that the observations can be modelled by means of a distributed hydrological model, assuming that the excess rainfall is accurately evaluated. More specifically, we show that the combination of the Soil Conservation Service Curve-Number (SCS-CN) procedure with constant

routing velocities results in an underestimation of the flow peak and a delayed time of peak. Better predictions of the peak of discharge, its timing, and the impulsive shape of the hydrographs could be obtained by coupling the SCS-CN method with a simplification of the Horton equation, and simulating the routing of runoff along the channel network by means of a matched diffusivity kinematic-wave model. The reliability of the method is tested by comparing simulated and observed timings of hyper-concentrated runoff or debris flow triggering in two neighbouring dolomitic watersheds.

Riassunto

In ambiente dolomitico, gli eventi di precipitazione di tipo convettivo, caratterizzati da brevi durate ed alte intensità, sono in grado di generare abbondanti deflussi superficiali alla base delle pareti rocciose. Questi deflussi incidono i ghiaioni presenti al piede dei bacini di testata e sono spesso responsabili dell'innesco di fenomeni di colata detritica. Con l'obiettivo di stimare le precipitazioni e portate dei deflussi superficiali, abbiamo installato una stazione di monitoraggio alla base del Campanile Dimai (gruppo del Pomagagnon - Dolomiti), nei pressi di Cortina d'Ampezzo (provincia di Belluno). La stazione è dotata di pluviometro e registra i dati di un misuratore di portata costruito in prossimità della sezione di chiusura (quota 1770 m s.l.m.) del canale roccioso inciso sul Campanile Dimai stesso. La struttura consiste in una piccola vasca impermeabilizzata di forma trapezoidale delimitata da uno stramazzo in parete sottile che raccoglie i deflussi generati dalle pareti rocciose del bacino di testata sovrastante (area ~ 0.032 km^2, pendenza media ~ 320 %). Le precipitazioni registrate nel periodo 2011-2017 hanno permesso di capire quali caratteristiche portano alla

formazione di deflusso e/o di trasporto solido nel bacino. Fra i vari idrogrammi registrati, è stato possibile considerarne significativi, sia in termini di valore di picco che di volume defluito, una dozzina. Queste misure sono un'occasione più unica che rara per approfondire la conoscenza riguardo alla risposta idrologica di questo tipo di bacini. Gli idrogrammi mostrano una risposta di tipo impulsivo, con un aumento improvviso del deflusso superficiale fino al valore di picco, seguito generalmente da un'altrettanto rapida decrescita. Queste misure di deflusso, inoltre, permettono di calibrare e validare i modelli idrologici. In questo lavoro, infatti, mostriamo come queste caratteristiche di deflusso possano essere riprodotte usando un modello idrologico distribuito, premesso che la precipitazione efficace venga valutata correttamente. L'utilizzo del metodo Curve Number del Soil Conservation Service (SCS-CN), combinato con la propagazione del deflusso a velocità costante, produce una sottostima del picco di deflusso ed un ritardo nel tempo di picco rispetto a quanto registrato. Per ottenere una riproduzione soddisfacente del valore di picco, del tempo di picco e della forma dell'idrogramma, il metodo SCS-CN deve essere accoppiato con una versione semplificata dell'equazione di Horton per la valutazione del deflusso generato. Inoltre, bisogna utilizzare un modello di onda cinematica, in cui la diffusività numerica è uguagliata a quella idraulica, per la propagazione della portata nel canale. Ad ulteriore conferma dell'affidabilità della metodologia sviluppata, vengono confrontate le tempistiche osservate e simulate per alcuni eventi di colata detritica/flusso iperconcentrato avvenuti in due bacini dolomitici in prossimità del bacino oggetto di studio.

Contents

List of Figures

List of Tables

Chapter 1

Introduction

In the recent past, various authors observed the increase of extreme rainfall events by frequency and intensity (Easterling et al., 2000; Frei and Schär, 2001; Fowler and Kilsby, 2003; Sillmann and Roeckner, 2008). Therefore, phenomena typically caused by short and torrential rainfalls such as debris flows, floods and debris floods, become less unusual (Floris et al., 2010). In the Alpine environment, a very dangerous phenomenon is debris flow because of its large destruction power against each obstacle it comes across and for its impulsive nature that makes it difficult to predict its occurrence and alert people of incoming hazard (Jakob and Hungr, 2005). In the period between 2015 and 2017, many debris flows occurred along the Upper Boite Valley (Belluno Dolomites, Eastern Italian Alps), in the municipalities of Vodo di Cadore, Borca di Cadore, San Vito di Cadore and Cortina d'Ampezzo. Debris flows in the alpine environment are triggered when abundant runoff generated on rocky low permeability surfaces after extreme rainfalls can dislocate the sediments in the channel at their base: the small size and high relief of the headwater basins gather exceptionally intense rainfall and deliver enough discharge to mobilize loose debris along these ephemeral channels (Coe and Godt, 2003; Berti and Simoni, 2005; Cannon et al., 2008; Coe et al., 2008; Gregoretti and Dalla Fontana, 2008; Theule et al., 2012; Hürlimann et al., 2014; Tiranti and Deangeli, 2015). The runoff

discharge of headwater basins is therefore the principal factor controlling debris flow initiation and magnitude. Debris availability represents the other requisite for triggering and may also constitute a factor limiting the overall magnitude of the event. The increasing frequency of this kind of phenomena in the Dolomites (Armento et al., 2008) highlights the need for improved knowledge of debris flow triggering processes (Bacchini and Zannoni, 2003); however, a lack of field observations of debris flow initiation has made it difficult to isolate the triggering processes (Kean et al., 2013). An approach to overcome the missing of field observations is the establishment of empirical critical rainfall thresholds to forecast the occurrence of an event (Godt et al., 2006; Gregoretti and Dalla Fontana, 2007; Guzzetti et al., 2007, 2008; Godt and McKenna, 2008; Borga et al., 2010; Brunetti et al., 2010; Staley et al., 2013; Marra et al., 2014; Staley et al., 2017). On the other hand, on monitored sites, rainfall-runoff models can be calibrated to provide estimates of critical discharge for debris flow initiation (Orlandini and Lamberti, 2000; Berti and Simoni, 2005). The prediction of runoff discharge assumes great interest also in risk assessment and mitigation. It allows the calibration of the solid-liquid input hydrograph for numerical models that simulate the downstream routing of debris flows (Rickenmann et al., 2006; Armanini et al., 2009; Pudasaini, 2012; Frank et al., 2015; Gregoretti et al., 2016a; Han et al., 2017). Despite its importance, runoff simulation in small rocky headwater basins is rarely supported by good quality experimental data. Existing data are gauged in channels downstream of impervious surfaces (Moody et al., 2008; Kean et al., 2012; Bouvier et al., 2015; Wei et al., 2017) or on hillslope forested zones (Sheridan et al., 2007). Furthermore the variance of hydrological behaviours is enhanced with decreasing drainage area (Uchida et al., 2005), making generalizations more uncertain and not entirely reliable (Wagener and Montanari, 2011). Therefore, as pointed out by Berti and Simoni (2005), "*debris flows initiated by channel bed mobilization are far less studied and poorly understood compared to landslide-induced debris flows. In particular, a framework to adequately characterize runoff generation, erosion processes, and*

debris flow generation is still missing".

1.1 Debris flow: general features

Gregoretti et al. (2016a) defined debris flows as "*rapid, gravity-induced mass movements consisting of a mixture of water, sediment, wood and anthropogenic debris that propagate along channels incised on mountain slopes and onto debris fan*", that can occur all over the world. An event of debris flow is unsteady and non-uniform, and usually consists of several pulses separated by lower depth and less concentrated flows. Each pulse is characterized by a front, a body, and a tail. The front is partially saturated, with a variable concentration by volume between 30% and 60% (Rickenmann and Zimmermann, 1993). Furthermore, it can reach velocities up to 30 m/s and it has significant erosion capacity and power to transport huge boulders, with a volume often greater than ~ 10 m^3 (Costa, 1984; Rickenmann, 1999; Berger et al., 2011; Iverson et al., 2011). The body is generally saturated, with a quasi-parallel free surface to the underlying bed (Davies, 1988). Its erosion capability was initially valued in the Illgraben basin in Switzerland by Berger et al. (2010), but its role in the overall erosion-deposition processes remains poorly understood (Iverson et al., 2011). The size of body transported sediments ranges from small particle to boulders. The tail assumes hyper-concentrated streamflow behaviour, with low concentration by volume and the presence of small size sediments (Iverson, 1997). Considering the debris flow cross section, it is generally observed the presence of lateral levees. Levees can be deposited on the side slopes of channels, when the debris flow bursts its banks, or it begins to deposit on the alluvial fan or on low slope areas (Iverson, 2003).

Looking at the rehologic features, debris flows have intermediate properties between water floods and rock avalanches: the differences with these related phenomena lie on influences on motion by solid and fluid forces (Iverson, 2005; McCoy et al., 2010). The fluid phase velocity is similar to the velocity of the solid
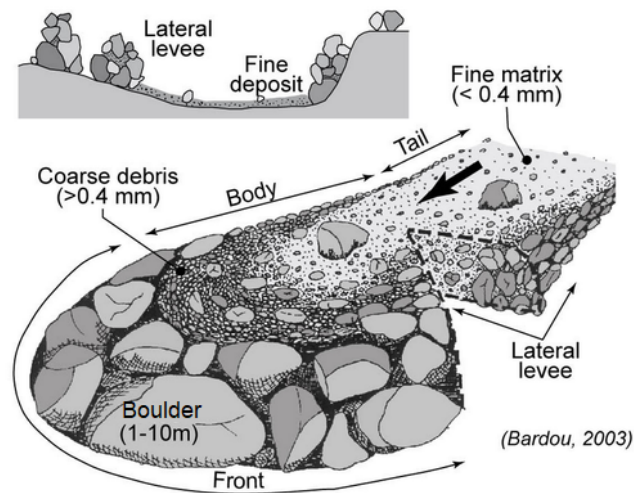
Figure 1.1: Representation of a typical debris flow, adapted from Bardou et al. (2003).

part, in contrast to stream flow sediment transport (Iverson, 1997). Therefore, on first approximation, the phenomenon can be described as a monophasic viscoplastic fluid (Johnson and Rodine, 1984; Remaître et al., 2005). Furthermore, the solid phase does not conserve its original shape; the fluid phase handles and mixes sediments. This behaviour is typical in a debris flow and distinguishes it from landslides (Jakob, 2005). Nevertheless, the distinction between these kinds of phenomenon is not clearly defined, and categorizations are numerous.

Generally, classifications are based on triggering processes and rate, morphology, type of material, geometry, and duration (Varnes, 1978; Cruden and Varnes, 1996; Hungr et al., 2001, 2014), or on dimensionless numbers (Takahashi, 2007; Lanzoni et al., 2017). Volumetric sediment concentration is the most significant parameter to define a phenomena as debris flow (Costa, 1984; Takahashi, 2007; Julien and Paris, 2010). The difficulty to evaluate sediment concentration during an event typically requires empirical classification on the basis of parameter estimates. Starting from Varnes' and Hutchinson's subdivisions (Hutchinson, 1968; Varnes, 1978; Hutchinson, 1989; Cruden and Varnes, 1996), Hungr et al. (2001) created a classification for gravity-induced movements with few categories, introducing new terminologies to enrich older classes. Adopted criteria

Table 1.1: Gravity-induced movement categorization made by Hungr et al. (2001).

Material	Water Content	Special Condition	Velocity	Name
Silt, Sand, Gravel, Debris	Dry, moist or saturated	no excess pore-pressure;limited volume	Various	Non-liquified sand (silt, gravel, debris) flow
Silt, Sand, Debris, Weak rock	Saturated at rupture surface content	liquefiable material; constant water	Ex. Rapid	Sand (silt, debris, rock) flow slide
Sensitive clay	At or above liquid limit	liquefaction in situ; constant water content	Ex. Rapid	Clay flow slide
Peat	saturated	excess pore-pressure	Slow to Very Rapid	Peat flow
Clay or Earth	Near plastic limit	slow movements; plug flow (sliding)	< Rapid	Earth flow
Debris	saturated	established channel; increased water content	Ex. Rapid	Debris flow
Mud	At or above liquid limit	fine-grained debris flow	> Very Rapid	Mud flow
Debris	free water present	flood	Ex. Rapid	Debris flood
Debris	partly or fully saturated	no established channel; relatively shallow;steep source	Ex. Rapid	Debris avalanche
Fragmented rock	various, mainly dry	intact rock at source; large volume	Ex. Rapid	Rock avalanche

to distinguish classes are movement mechanics and velocity, material properties, water content and plasticity index (Table 1.1).

When a phenomenon is classified as a debris flow, other categorizations need to be consulted to better understand its typology. Subdivisions can be based on macroscopic behaviour of flow (triggering typology, moved debris volume, inundated areas, flow discharge), or on microscopic internal parameter (as grain size, volumetric concentration, viscosity, velocity gradient). The classification of Jakob (2005) belongs to the first category. Jakob (2005) proposed a size classing (reported on Table 1.2), based on peak discharge, total volume and area inundated by the event. As reported by the author, "*this system will be useful for regional debris-flow studies such as those conducted to evaluate the effects of a landslide-triggering storm or for hazard overview studies along infrastructure corridors*".

The classification made by Takahashi (2007) is part of the second category, and it is based on dimensionless parameters, as Reynolds and Bagnold numbers. The Reynolds number N_{Re} is the ratio of momentum stresses τ_t to viscous stresses τ_v and it is used to classify flow as laminar or turbulent; the Bagnold number N_{Ba} is the ratio of grain collision stresses τ_c to viscous stresses τ_v and

Table 1.2: Size classification for debris flows, from Jakob (2005): V is the total volume, Q_b and Q_v are the peak discharge for bouldery and volcanic debris flows respectively,B_b and B_v are the area inundated by bouldery and volcanic debris flows, N/A signifies that boulder debris flows of this magnitude have not been observed.

Size class	V, range (m^3)	Q_b, range (m^3/s)	Q_v, range (m^3/s)	B_b (m^2)	B_v (m^2)	Potential consequences
1	$<10^2$	<5	<1	$<4\times10^2$	$<4\times10^3$	Very localized damage, known to have killed forestry workers in small gullies, damage small buildings
2	10^2–10^3	5–30	1–3	4×10^2–2×10^3	4×10^3–2×10^4	Could bury cars, destroy a small wooden building, break trees, block culverts, derail trains
3	10^3–10^4	30–200	3–30	2×10^3–9×10^3	2×10^4–9×10^4	Could destroy larger buildings, damage concrete bridge piers, block or damage highways and pipelines
4	10^4–10^5	200–1500	30–300	9×10^3–4×10^4	9×10^4–4×10^5	Could destroy parts of villages, destroy sections of infrastructure corridors, bridges, could block creeks
5	10^5–10^6	1500–12,000	300–3×10^3	4×10^4–2×10^5	4×10^5–2×10^6	Could destroy parts of towns, destroy forests of 2 km^2 in area, block creeks and small rivers
6	10^5–10^6	N/A	3×10^3–3×10^4	$>2\times10^5$	2×10^6–3×10^7	Could destroy towns, obliterate valleys or fans up to several tens of km^2 in size, dam rivers
7	10^6–10^7	N/A	3×10^4–3×10^5	N/A	3×10^7–3×10^8	Could destroy parts of cities, obliterate valleys or fans up to several tens of km^2 in size, dam large rivers
8	10^7–10^8	N/A	3×10^5–3×10^6	N/A	3×10^8–3×10^9	Could destroy cities, inundate large valleys up to 100 km^2 in size, dam large rivers
9	10^8–10^9	N/A	3×10^6–3×10^7	N/A	3×10^9–3×10^{10}	Vast and complete destruction over hundreds of km^2
10	$>10^9$	N/A	3×10^7–3×10^8	N/A	$>3\times10^{10}$	Vast and complete destruction over hundreds of km^2

it is helpful to subdivide flow regimes (macroviscous, collision-dominated):

$$N_{Re} = \frac{\tau_t}{\tau_v} = \frac{\rho_m U h}{\mu}; \qquad N_{Ba} = \frac{\tau_c}{\tau_v} = \frac{\rho_s d^2 \lambda^{1/2} \gamma}{\mu} \qquad (1.1)$$

where ρ_m indicates the density of the entire debris flow mixture, U the cross-sectional mean velocity, h the flow depth, μ the apparent viscosity, ρ_s indicates the particle density, d the grain diameter, λ the linear concentration, γ the shear rate and μ the apparent viscosity of the debris flow. λ is defined by $\lambda = [(CC^*)^{1/3} - 1]^{-1}$, where C is the grain concentration and C^* the maximum possible concentration. The last dimensionless parameter characterizing this classification is the flow relative depth h/d, namely the ratio of the flow depth h to the representative particle diameter of bed d. On the basis of values of these parameters, Takahashi (2007) subdivided debris flows into three classes, as reported in Figure 1.2. Viscous debris flows are those dominated by viscoplastic stress τ_v, the stony debris flows are dominated by particle collisions (stress τ_c) and those controlled by turbulent mixing stress τ_t are termed turbulent muddy debris flow. This kind of classification is useful to highlight the differences between debris flows. Small variations of parameters, which can be volumetric
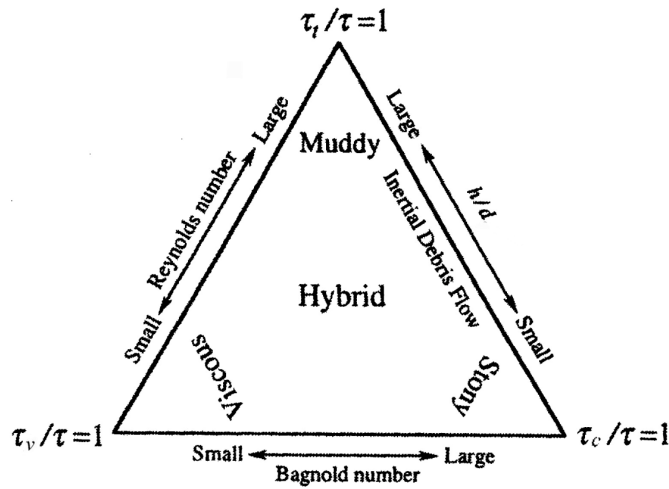
Figure 1.2: Sketch from Takahashi (2009) of debris flow subdivision made by Takahashi (2007): τ is the total shear stress, τ_v the viscous shear stress, τ_c the shear stress due to particle collision, τ_t the turbulent mixing stress, h the flow depth and d the representative particle diameter of bed.

concentration, grain size, or debris geology, heavily influence debris flow behaviour, particularly the travel distance and the deposition area. Starting from the classification of Takahashi (2007) that followed the works of Iverson (1997) and Iverson and Vallance (2001), Lanzoni et al. (2017) explained how to use dimensionless numbers to categorize debris flows, and introduced other well-known dimensionless groups for having a more complete classification (Figure 1.3).

1.2 Debris flow triggering mechanism

A debris flow watershed is generally subdivided into three zones: an initiation or triggering area, an intermediate area improperly called transportation zone, and a deposition area (Figure 1.4).

Talking about runoff-generated debris flows, the triggering area is characterized by significant slope gradients and loose sediments, easily removable by a water flow. The sediment recharge is guaranteed by a slow but continuous
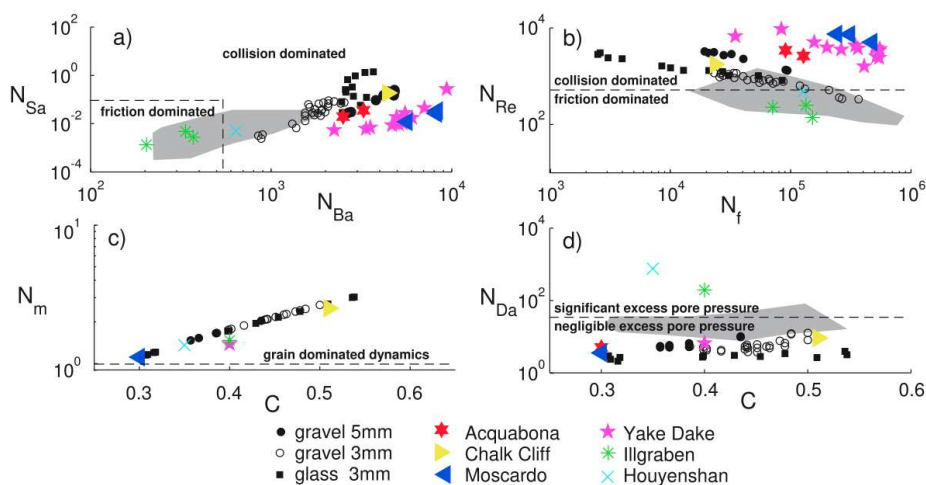
Figure 1.3: Experimental and occurred debris flow data plotted in four dimensionless number spaces. N_{Sa} is the Savage number, N_{Ba} is the Bagnold number, N_{Re} is the Reynolds number, N_f is the friction number, N_m is the mass number, N_{Da} is the Darcy number, and C is the linear concentration. In panel (a), dashed lines delimit area where solid friction and fluid viscosity dominate; in panels (b-d), dashed lines separate the different rheological regimes. From Lanzoni et al. (2017).

erosional process or by slope failures (Marchi and D'Agostino, 2004). The transportation zone is the part of the basin subject to the debris flow routing. In the transportation zone, the dynamic of debris flow is less studied due to difficulties on research: difficulties could be the installation and the maintenance of monitoring stations near the unstable channels where debris flows occurs, the possible damaging of sensors that need contact with debris flow, the inaccuracy on measures or the indirect measurements of non-contact instruments. Recent studies (Hürlimann et al., 2006; Brayshaw and Hassan, 2009; Iverson et al., 2011) highlight its importance for the development of flood risk maps: in this area, debris flows can vary their magnitude, concentration, or rheology due to erosion/deposition of bed or banks, sediment supply from side source areas, and lateral inflow. The deposition zone generally corresponds to an alluvial fan, characterized by lower slopes and non-confined area. The size, shape and the stopping slopes of deposits mainly depend on debris flow rheology and volumetric concentration, in addition to local topographic conditions (Bardou
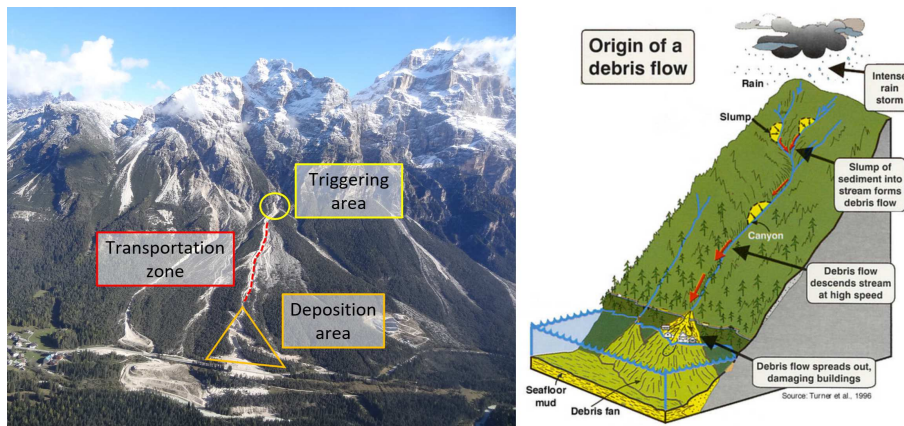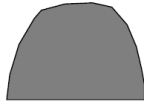
Figure 1.4: Zones within a debris flow watershed. The figure shows on the left the Acquabona Punta Nera basin (Dolomites, North-eastern Italy), on the right a schematic representation of a debris flow phenomenon given by Turner and Schuster (1996)).

et al., 2003), as reported on Table 1.3.

Focusing on the initiation area, a debris flow could initiate when determined conditions are satisfied. A sufficient sediment availability and a slope gradient adequate to debris properties could promote a debris flow in presence of a critical water input. The most relevant sources of water are extreme rainfalls and/or a rapid snowmelt (Rickenmann and Zimmermann, 1993; Iverson, 1997). More common triggering processes are initiation from landslide, dam break, and channel-bed failure. Recent studies (Brayshaw and Hassan, 2009; Berger et al., 2010) highlighted significant parameters for initiation of debris flows from landslide entering low-order channels. They found that "*steeper channels, low angles of entry, lower volumes of in-channel sediment, and larger initial failures were more likely to result in debris flows*" (Brayshaw and Hassan, 2009). Natural dams can be classified into moraine dams, glacier-ice dams and landslide dams. While in some cases dam break occurrence could be dissociated from rainfalls (Gregoretti et al., 2010; Sattler et al., 2011), debris flows are the gravity-induced mass movements most influenced by precipitation. By comparing field surveys and outcomes of numerical modelling, McGuire et al. (2017) affirmed that debris flow initiation in post-wildfire sites seems occurring through the mass failure of

Table 1.3: Deposition appearance considering rheophysical properties of debris flows, from Bardou et al. (2003).

		viscoplastic	collisional-frictional	frictional-viscous
Mechanics	**Scientific name**	viscoplastic	collisional-frictional	frictional-viscous
	Appropriate rheophysical model	Herschel-Bulkley Bingham	Coulomb-like, collisional-frictional constitutive equation	Coulomb-like at low speed Newton-like (or power-law) at high speed
Field observation	**Common name**	muddy	granular	fluid
	Deposit appearance	smooth with clear limits in the field, very cohesive once dry levee cross-section	rough with no clear deposits limits in the field, non cohesive once dry levee cross-section	terrace-like deposit, very cohesive once dry whole body cross-section (not the same scale as levee cross-section sketch)
	Stopping slope	$< 2°$	$< 10°$	$< 1°$
	Grain size	grains + + matrix + + clays +	grains + + matrix- clays - -	grains - / + matrix + + silts + clays -

The following notation is adopted :
 − − very little content
 − little content
 + high content
 + + very high content

in-channel sediments rather than for the progressive grain-by-grain bulking. In the Dolomites, instead, the most common triggering process is by channel-bed failure through grain-by-grain bulking (Berti et al., 1999; Berti and Simoni, 2005; Gregoretti and Dalla Fontana, 2008). It is due to hydrodynamic forces exerted by the runoff discharge on the surface sediment layer (as highlighted in Figure 1.5). The water flow predisposition for entraining large quantities of sediments depends on channel bed slope, on geometrical and geomorphological characteristics of the site, and on availability and grain size of material (Gregoretti and Dalla Fontana, 2008). To explain the fundamental role of the sediment amount, Figure 1.6 illustrates debris supply processes into two different typologies of basin, weathering-limited (or supply-limited) and transport-limited (or supply-unlimited). While there are always enough available sediments into a transport-limited basin, into a supply-limited system, sediment deposits have to exceed a triggering threshold before rainfall could initiate a debris flow (Bovis and Jakob, 1999). The hypothesis made by Bovis and Jakob (1999), of critical

Figure 1.5: Example of erosional process due to surface runoff in the Dolomites (Rovina di Cancia catchment), before (panels (a) and (b)) and after (panels (c) and (d)) a small debris flow occurred (July 29th, 2012). The panels show upstream (on the left) and downstream (on the right) views of the initiation area. The evident sediment deposit in panel (a) and (b) was scoured by water discharge, which longitudinally eroded the bottom of channel (visible in the inserts (c) and (d)).

sediment threshold constant in time, was partially revised by Brayshaw and Hassan (2009), who observed that this triggering threshold increases over time, i.e. the probability of occurrence of a new debris flow decreases with time. On the other hand, into a supply-unlimited watershed, sufficient water supply for the saturation of the sediment layer is required to trigger and propagate the debris flow (Iverson, 1997; Marchi and D'Agostino, 2004). In fact, many studies highlighted as debris flows could initiate after the sediment layer saturation due to the development of positive interstitial pressure (Reid et al., 1997; Berti and Simoni, 2005; Iverson et al., 2011). This can result following a vertical direct infiltration or a lateral groundwater inflow from adjacent soils. Factors such as inclined water tables, or the convergence of topography can funnel flows laterally (Anderson and Burt, 1978). The general description of pore-pressure development is the generation of a saturated region at the base of the slope, that progressively rises with prolonged rainfall. When complete saturation is

weathering-limited system (supply-limited)

transport-limited system (supply-unlimited)
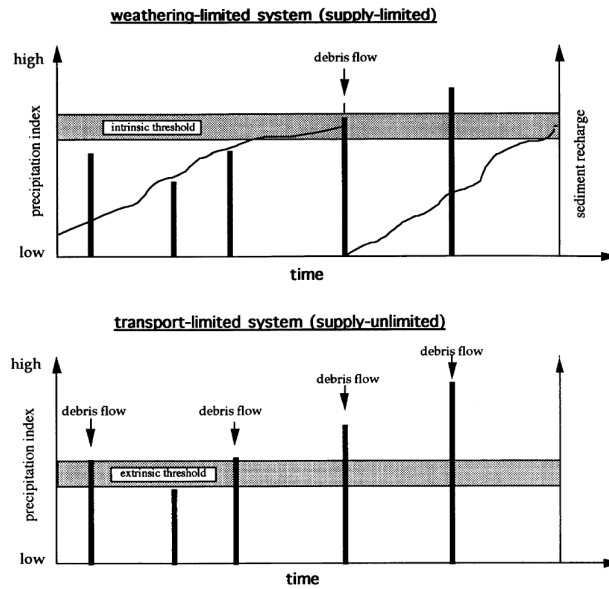
Figure 1.6: Mechanism of channel recharge/discharge into weathering-limited or transport-limited basins. Bars indicate rainfalls, rising lines indicate sediment recharge. From Bovis and Jakob (1999).

reached, slopes begin to collapse. To determine interstitial pressure, antecedent soil moisture conditions (AMC) need to be considered. Being an indicator about the degree of saturation of the soil, AMC directly influences slope stability, but its evaluation is problematic. AMC is generally derived by using indirect estimation, as antecedent cumulative rainfalls, and water table heights. The first attempt to standardize AMC was made by the Soil Conservation Service (1972). Considering the previous 5-days cumulative rainfall, they divided AMC in three classes, from dry (I) to wet (III) conditions (Table 1.4). However, it is essential to remark that AMC could also be directly estimated: in instrumented catchments, pore pressure and soil moisture can be assessed by means of pressure transducers and soil moisture meter probes (Coe et al., 2008; Kean et al., 2011).

1.3 Analysis of triggering rainfalls

As highlighted before, rainfall is the most significant factor for debris flow triggering. Critical triggering thresholds can be reached by short heavy rainfall

Table 1.4: AMC classification from Soil Conservation Service (1972).

| AMC class | 5-days prior rainfall (mm) | |
	Dormant season	Growing season
I	h< 12.7	h<35.6
II	12.7<h<27.9	35.6<h<53.3
III	h>27.9	h>53.3

or extended low intensity precipitation. In the Dolomites context, triggering precipitations are generally short, localized and high-intensity summer storms (Berti et al., 2000; Underwood et al., 2016). This kind of precipitation quickly saturates the terrain upper layer, so that water cannot further infiltrate. Runoff flows rapidly downhill and fills up the drainage network. Flash floods are extremely dangerous, they combine destructive power of flood and difficult forecasting (Lin, 1999). The flood peak occurs immediately after the rainfall event: differences in timing range from between a few minutes to a few hours, according to the catchment scale (Creutin and Borga, 2003; Kean et al., 2012). For the forecasting of debris flows, a common largely-used tool is the development of empirical rainfall thresholds (Caine, 1980; Innes, 1983; Moser and Hohensinn, 1983; Bacchini and Zannoni, 2003; Crosta and Frattini, 2003; Gregoretti and Dalla Fontana, 2007; Guzzetti et al., 2008; Salciarini et al., 2012; Staley et al., 2013; Marra et al., 2014; Peruccacci et al., 2017; Staley et al., 2017), defined as the conditions that, exceeded, result in the occurrence of a debris flow (Figure 1.7). Thresholds can be subdivided by means of process-based (physical) or empirical approaches (Aleotti, 2004; Godt et al., 2006; Guzzetti et al., 2007), and usually link rainfall duration with other precipitation features, as mean or maximum intensity, or cumulative rainfall (Crosta and Frattini, 2000). In the past, empirical thresholds were generally defined as minimum thresholds, i.e. obtained enveloping the critical points with the lowest values. Nowadays, empirical thresholds are usually defined by means of statistical methods (Brunetti et al., 2010). The typical critical threshold (ID equation) links rainfall duration
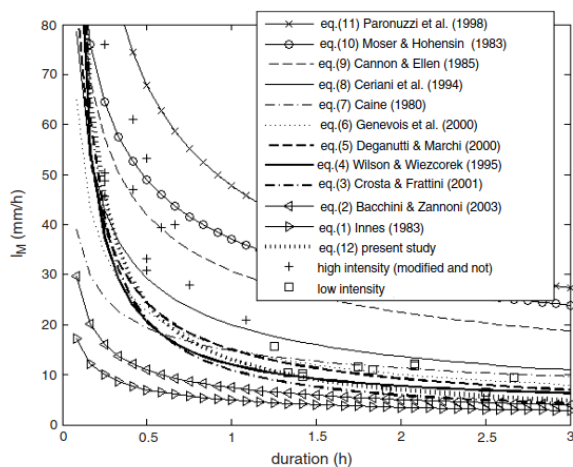
Figure 1.7: Example of empirical critical intensity-duration thresholds, extracted from different studies (for equations and references, see Gregoretti and Dalla Fontana (2007)). The Figure highlights the variability between rainfall thresholds mainly due to local factors. From Gregoretti and Dalla Fontana (2007).

D to mean rainstorm intensity I and assumes the general form:

$$I = \alpha D^{-\beta} \tag{1.2}$$

with α and β parameters of the equation. Comparing different thresholds, a significant variability is evident: it is due to the selection of rainfall parameters, the magnitude of the triggered events, and the variability in hydrological, geological and meteorological conditions (Gregoretti and Dalla Fontana, 2007) and it emphasizes the empiricism of this triggering forecasting method (Figure 1.7). Furthermore, uncertainties related to each threshold may not be defined.

The main source of uncertainty is the large spatio-temporal variability of precipitations in mountainous areas (Marra et al., 2014). Generally, the rainfall that triggers one or more debris flows is unknown. Estimations of triggering rainfall are acquired by means of rain gauges, weather radars or satellites. Using rain gauges, the principal cause of uncertainty is the distance of the reference rain gauge from the initiation zone of the debris flow, both planimetrically and

on elevation (rain gauges are usually placed in the valley bottoms). Weather radar estimates are affected by various errors, like the attenuation of the signal for long distances or intense rains, or the occlusion of the radar beam (typical in mountain areas) (Germann et al., 2006), and need to be calibrated by using ground truths. Satellites are useful for monitoring global-scale dynamics, but the coarse spatio-temporal resolution does not permit to use them for watershed analysis, whereas it seems to become less uncertain for a regional approach (Nikolopoulos et al., 2017).

Another remarkable issue that arises using critical thresholds is the occurrence of false positives or negatives (Staley et al., 2013, 2017). False positives arise when rainfall conditions forecast a debris flow that does not occur, whereas in false negative, rainfall conditions, leading to a real debris flow, are not detected. These errors are related to each factor, that could be hydrological or geological, that has a role in the variability of the thresholds and in the specificity of each watershed. For this reason, to overcome the limitations of using empirical formulas, a less empirical estimate triggering condition becomes fundamental. For example, Staley et al. (2017) developed a framework for regions where no historical data exist. The model combines the assessment of the statistical likelihood of debris flow occurrence with the definition of spatial explicit intensity-duration thresholds, defined as the rainfall intensity equal to the 50% likelihood of debris flow. Another possible approach to solve the problem is the development and the use of an hydrological model.

1.4 Hydrological modelling

Hydrological models are numerous and different (Rodríguez-Iturbe and Valdés, 1979; Rinaldo et al., 1991; Orlandini and Rosso, 1996; Orlandini and Lamberti, 2000; Saco and Kumar, 2002b; Botter and Rinaldo, 2003; Grimaldi et al., 2012). Main distinctions are made on spatial input (lumped or distributed models), temporal variability (continuous or single-event models), physical realism of

simulated problems (physically based, conceptual or empirical models), kind of involved variables (deterministic or stochastic models) and linearity of model. With improvements of computing power and availability of hydrological data recorded at fine temporal and spatial scales, models are becoming more complete, but more complex (Montanari and Brath, 2004). Complexity increases the number of parameters used to simulate real processes, so the parameter calibration is becoming the next contest (Liu and Gupta, 2007). In fact, Wagener et al. (2001) proposed a framework for investigating the equilibrium balance between model complexity and available data (Figure 1.8). The calibration process is required because reliable reproduction of catchment behaviour is often unobtainable just taking into account the basin characteristics (Wagener and Montanari, 2011). During a calibration, the model relies on rainfall-runoff observations to understand how a particular watershed works. Different combinations of parameters represent different real conditions, so modelling needs to be supported by field surveys. Additionally, integration of hydrological model with spatial descriptions given by digital terrain model (DTMs) and digital surface models (DSMs) allows to describe distributed phenomena (erosion/deposition) at the pixel scale, and then to integrate them to the entire watershed (Orlandini and Rosso, 1996).

However, the hydrology of a catchment is complex to understand and the uncertainty in the streamflow estimates remains (Montanari and Brath, 2004; Ebel et al., 2007a,b; McDonnell and Beven, 2014). The lack of observations in the most catchments of the world and the uncertainty in model predictions at these sites are seen as main limitations for hydrology (Sivapalan, 1993). Uncertainties have to be understood, quantified and, mainly, reduced (Masih et al., 2011). Without an adequate comprehension of all different source of errors, it is difficult to quantify and reduce them. Diverse sources could introduce significantly different errors that require distinct resolution techniques. Furthermore, neglecting some causes of errors could lead to wrong predictions in the hydrological output (Liu and Gupta, 2007). For a good estimation of uncertainties, the
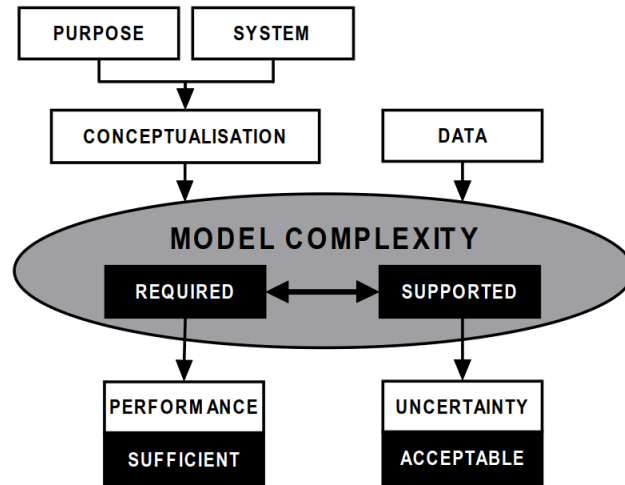
Figure 1.8: Framework proposed by Wagener et al. (2001) for development and application of hydrological models, considering required level of detail and complexity supported by available data. From Wagener et al. (2001).

knowledge about their probability distribution and their error characteristics is necessary. For this reason, the typical solution for quantifying the uncertainty in hydrological outputs is to represent outcomes in terms of probability distribution, performing probabilistic models instead of deterministic ones (Montanari and Brath, 2004). However reducing uncertainties is possible: realistic solutions could be the acquisition of more quality hydrological data, the improvement of model constitutive equations, and the enhancement of model ability to extract information from input (Liu and Gupta, 2007; Wagener and Montanari, 2011).

Neglecting the great uncertainty on flood hydrograph due to the storm spatial movement (Koren et al., 1999; Zoccatelli et al., 2011), the fundamental processes of hydrological catchment response are the calculation of excess rainfall distribution and the routing of generated runoff to the basin outlet. Infiltration is a critical element in the rainfall-runoff models and it is influenced by rainfall intensity and top soil hydraulic properties. Infiltrated water can percolate to deep groundwater, evaporates, or flows downhill as subsurface flows (Figure 1.9). At the beginning of precipitation, most of rainfall infiltrates into the soil, rising the water table. Increasing of soil moisture, the infiltration capacity de-
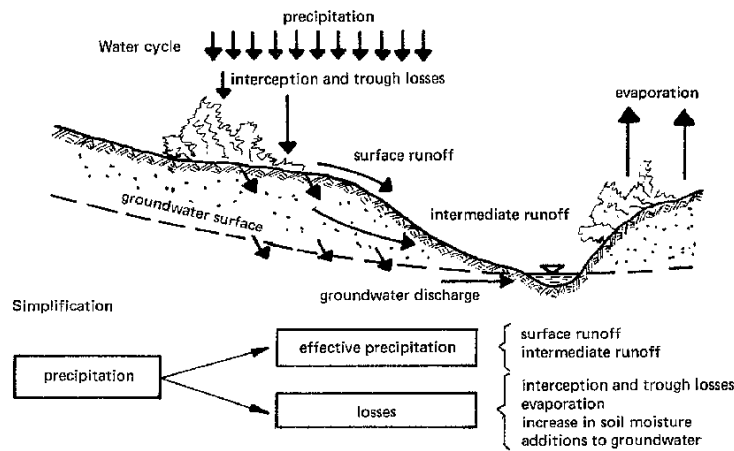
Figure 1.9: Separation process of fallen rainfall, from Lauterjung and Schmidt (1989).

creases, rainfall begins to pond on surface and it generates runoff. Runoff is routed to basin outlet through the slope-imposed pathways (Tarboton, 1997). The catchment runoff time is given by three factors: the holding time for rainfall excess, and the hillslope and the channel network travel time. The contribution of hillslope and network geomorphology to the hydrological response has been investigated by several authors (Rodríguez-Iturbe and Valdés, 1979; Rinaldo et al., 1991; Robinson et al., 1995; Di Lazzaro, 2008; Li et al., 2011). With concepts of geomorphological dispersion (Rinaldo et al., 1991), kinematic dispersion (Saco and Kumar, 2002b,a), and dispersive hillslope mechanism (Saco and Kumar, 2004), the relative role of hillslope and channel paths on the basin response was better understood, as well as the relevance of overland flow with respect to channel processes at different scales (Botter and Rinaldo, 2003; D'Odorico and Rigon, 2003). However scales issues and regionalisation of model parameters are still unresolved problems (Croke and Norton, 2004; Montanari and Toth, 2007; Seibert and Beven, 2009).

To calculate infiltration and runoff, hydrological models adopted for modelling runoff generating debris flow use simplified or empirical equations (Berti and Simoni, 2005; Coe et al., 2008). Lower parameter number encourages the model calibration and simulation time decreases. As stressed above, physically-

based models need field surveys and laboratory tests to evaluate parameters and this is not always simple in high mountainous environments. In fact, despite the noteworthy importance, water discharge measures at the outlet of headwater catchments are rarely performed, mainly for the difficulty related to the measurement in steep torrents (Onda et al., 2006; Kean et al., 2012). As a consequence, runoff is commonly gauged downstream the rocky outcrops (Onda et al., 2006; Moody et al., 2008; Bouvier et al., 2015; Wei et al., 2017) or on hillslopes (Sheridan et al., 2007), but a real systematic assessment of surface runoff triggering debris flows is still lacking.

1.5 Aim of the study

The goal of this work is to perform an hydrological analysis in the Dolomites (North Eastern Italian Alps) near Cortina d'Ampezzo, recording precipitations and corresponding headwater basin discharges to better understanding the runoff generation and modelling the triggering of runoff-generated debris flows. To reach this objective, an experimental facility has been installed at the outlet of a small rocky headwater catchment in the Dolomites. The facility is located just upstream the fan apex where debris flows could initiate and propagate. In parallel, the hydrological model of Gregoretti and Dalla Fontana (2008) has been upgraded both on rainfall separation and channel network routing. The measured water discharges are thus used to improve the understanding of basin response and to test the different levels of the model upgrade.

The work is structured as follows:

- Chapter 2 describes the study area, the hydrological model and the collected data;

- Chapter 3 reports the main reached outcomes, both on rainfall analysis and in hydrological modelling;

- Chapter 4 summarizes the conclusion of the research.

Chapter 2

Materials and methods

2.1 The field site

The Fiames monitoring site is located in the river Boite valley, three kilometres north of Cortina d'Ampezzo (BL), along the national road 51 (Figure 2.1). In this area, carbonatic Platform formations dominate. Limestones of the "Calcari Grigi" formation overly the thick dolomitic succession of the "Dolomia Principale" formation. The scree on the left side of the Boite valley is incised by numerous debris flow channels. They originate at the base of the steep rock cliffs (Marchi et al., 2008) and threaten the national road and the activities around it. Debris flows frequently occur along these channels. These events are triggered by the water discharge delivered by rocky channels descending from the upstream cliffs (see lower insert of Figure 2.1). The loose sediment material, essential for the triggering of solid-liquid wave, is provided by both the weathering of upstream cliffs and the shallow failures affecting the channel banks.

The Dimai watershed (delimited by a line in Figure 2.1) is very impervious. The basin has an area of 0.032 km^2, a mean elevation of 2043 m a.s.l., and an average slope of 319%, corresponding to 72.3º. It is drained by a rocky channel incised on the Dimai Peak. The channel is usually dry and the bed is

Table 2.1: Dimai headwater basin, morphological characteristics extracted from a 1-m resolution DEM obtained from a Lidar survey accomplished on 2011.

Area (km^2)	0.032
Min elevation (m a.s.l.)	1716
Mean elevation (m a.s.l.)	2043
Max elevation (m a.s.l.)	2306
Mean slope (°)	72.3
Max slope (°)	88.3
Channel mean slope (°)	67.2
Land use	95% bare rock
	5% moors and heathland

characterized by very high vertical steeps (about 5-10 m), with the presence of several boulders. Its mean slope is 238% (i.e., 67.2°). Geomorphological features are summarized in Table 2.1 and have been computed by using a DEM (1 m grid size) derived from a Lidar survey carried out on October 2011 with a sampling density of 3 points/m^2. The use of LiDAR topographic dataset is fundamental for improving the definition of a basin, compared to its description furnished by the conventional contour-based maps. The contour-based DEMs are not enough accurate to represent the very steep slopes typical of the headwater catchments, that, conversely, can be better described by the high-density LiDAR points. The improved description of valley and channel profiles, as well as the parametrization of stream channel geometry, reflects on the simulation of the hydrological responses. Degetto et al. (2015), focusing on the Dimai and the Rovina di Cancia (Section 2.4) basins, highlighted how the contour-based DEMs erroneously determined the watershed divides and smoothed the real surfaces, creating artificial and uncorrected flow paths, with a simplification of the channel networks, less branched and shorter. This poor accuracy in the topographical description largely influenced the hydrological simulations, leading to less peaked and delayed runoff responses.
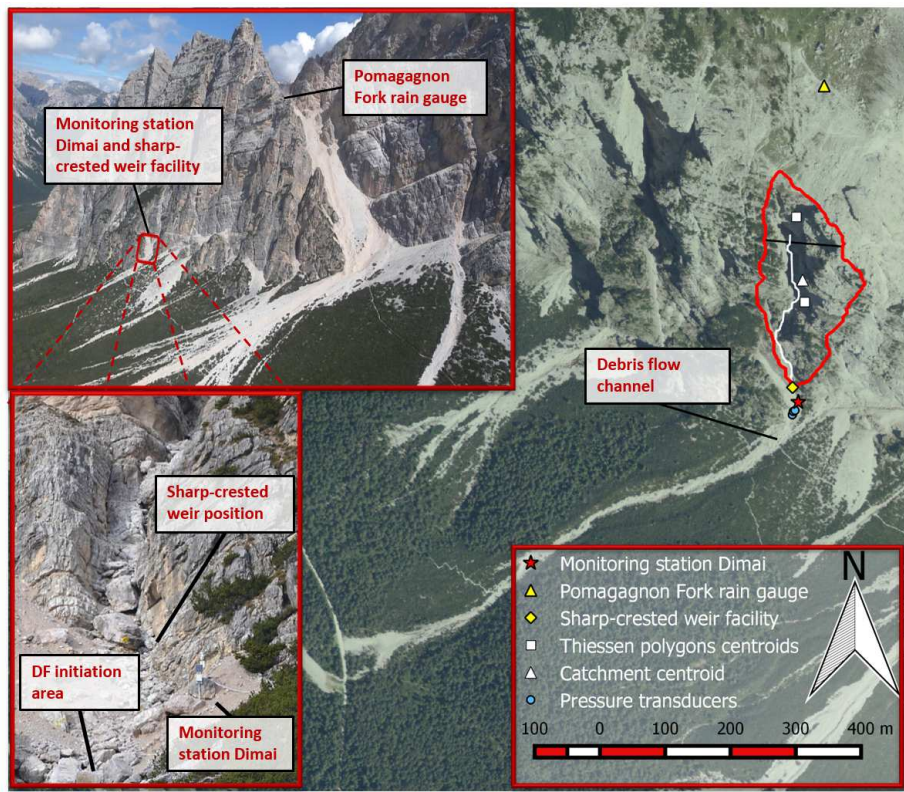
Figure 2.1: Aerial view of the area of Fiames, near to Cortina d'Ampezzo (BL), with the considered catchment (red line) and the locations of measuring facilities. The inserts show the frontal view of the monitoring site (upper insert) and a view of the outlet of the watershed (lower insert). Adapted from Gregoretti et al. (2016b).

2.1.1 The monitoring station

With the purpose to increase knowledge about both the runoff discharges at the feet of the rock cliffs and the triggering of debris flows, a monitoring station was installed at the base of the Dimai Peak, on July 2010. It has a rain gauge, a thermometer, four pressure transducers, three of which buried into the scree, 2 cameras that record the upstream rocky channel and the downstream scree, a control and synchronization unit powered by a couple of 12 V batteries recharged by a solar panel. The monitoring station normally records the data supplied by rain gauges and pressure transducers every 5 minutes. The sampling interval decreases to 5 seconds when the rainfall intensity exceeds the threshold

value of 0.6 mm/2.5 min, triggering the alarm mode. At the outlet of the main rocky channel incised on Dimai Peak, just upstream the monitoring station, a sharp-crested weir was installed on August 2011. The weir is monitored by a time-lapse camera, that records images every 20 seconds (60 seconds in 2013), and a pressure transducer provides the water level upstream it (see Section 2.1.2).

2.1.2   The sharp-crested weir stilling basin

The sharp-crested facility (Figure 2.2) consists of a small trapezoidal-shape basin (2.0 m long and, on average, 1.78 m wide), with a flat and concrete-covered bottom. It is limited by a rock wall and a giant boulder on the left and right sides respectively. On the downstream side, the basin is confined by a steel plate, 0.67 m high and 1.55 m wide, that operates as sharp-crested weir. On the upstream side, two levels of gabions work as filters to prevent the filling of the facility because of sediments transported during high intensity runoff events. Gabions are filled with coarse material (gravel 0.2 m size on average) and drained with pipes inside (0.08 m diameter). The volume of water that the stilling basin can contain before the spilling over the weir is about 2.5 m^3. A pressure transducer is placed 0.90 m upstream the weir, to provide the water level measurement. It is posed inside a PVC pipe perforated and covered by a filter to prevent collisions and burying, and is connected to the monitoring station by a cable fixed on the rocky wall. In Appendix A, the reader can find some pictures about the construction of the sharp-crested weir facility. The pressure transducer is carefully positioned inside the protection PVC pipe with the tap at the same level of the bottom of the steel plate. It is of piezoresistive type (Keller, series 26W, output signal 400-2000 mV) with a range 0-0.5 bar (0-5.1 m of water depth) and a measurement error of about $\epsilon_h = \pm 1$ mm (0.3 mV). The zero of the instrument was identified by exposing it to different known water levels and verifying its output signal. The zero resulted close to the theoretical value of 400 mV.
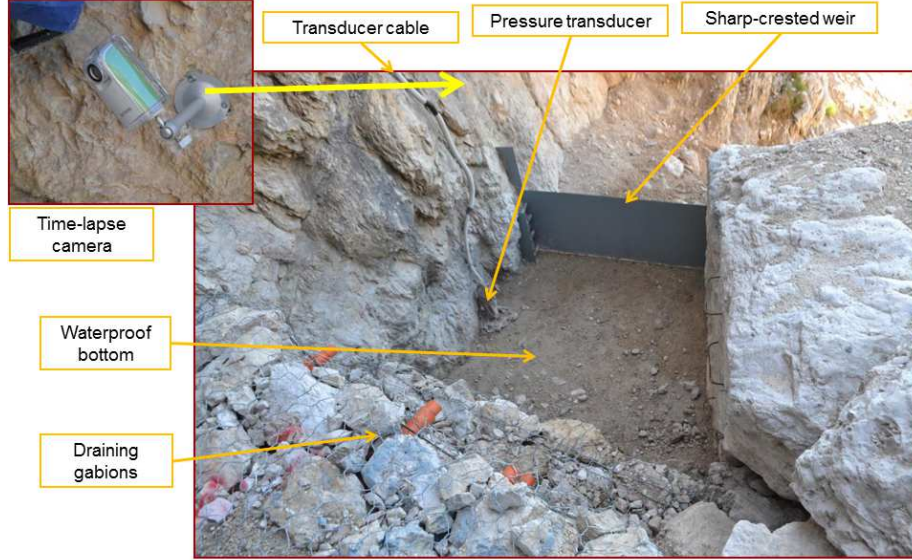
Figure 2.2: Upper view of the sharp-crested facility.

Using water level recorded it is possible to compute flow discharge through the continuity equation applied to the stilling basin:

$$Q(t) = \frac{dV}{dt} + Q_L + Q_O, \qquad (2.1)$$

where $Q(t)$ is the inflow discharge descending from Dimai Peak, Q_O is the outflow discharge, Q_L is water loss caused by the non-perfect waterproofing of bottom (evaluated $Q_L \approx 0.6 \times 10^{-4} m^3/s$), V is the water volume in the facility and t is time. Q_O is 0 when the water level h is lower than the weir level p, otherwise it is given by the weir discharge equation:

$$Q_O(t) = C_D b \sqrt{2g} \left[h(t) - p\right]^{3/2} \qquad (2.2)$$

where C_D is the discharge coefficient and $b = 1.55 - 0.1(h - p)$ the effective width of the weir (considering the lateral contraction on the right side). $Q(t)$ was computed by means of backward differences for the discretization of $\frac{dV}{dt}$ and

Figure 2.3: Frontal view of sharp-crested weir taken by the time-lapse camera on July 25th, 2015. The left panel shows the stilling basin partially filled, the right displays the flow discharge over the weir. In both the cases, the water level in the stilling basin is almost steady.

setting $Q_O(t)$ equal to its mean during a computational step. The errors in the estimation of discharge $Q(t)$ was evaluated in $\epsilon_{dV/dt} = \pm 0.7$ l/s and $\epsilon_{Q_O} = \pm 0.1$ l/s. These uncertainties are related to the error ϵ_h, i.e. the error caused by a measure of h on the evaluation of $\frac{dV}{dt}$ and $Q_O(t)$. The global error, assessed as sum in quadrature of $\epsilon_{dV/dt}$ and ϵ_{Q_O} (Taylor, 1997), is less than 1 l/s. In Figure 2.4, we show an example of the evolution of water level and the related assessed discharge. The runoff fluctuations are due to the intermittent behaviour of the inflowing discharge. During the decreasing limb, the water level oscillates on the order of few millimeters, corresponding to runoff fluctuations of a few l/s.

The sharp-weir facility was built on summer 2011. About ten days after its inauguration, the stilling basin was completely obstructed by a rockfall initiated after a severe storm, 16.2 mm/10 mins. After the removal of the huge boulder above it (Figure 2.5), the measuring facility was ruined by snow avalanches on 2014 spring. As a consequence, the stilling basin was fully working only five days in 2011 and a few months in the period 2013-2014. After 2014, the stilling basin has been filled or obstructed several other times again (e.g. Figure 2.6 shows the basin after the refilling occurred the 14th of August 2016). When it happens, the steel plate needs to be removed and the basin emptied with shovels, picks and perseverance. Table 2.2 reports the significant events occurred during the monitored period 2011-2017. In Appendix A, we also illustrate the various
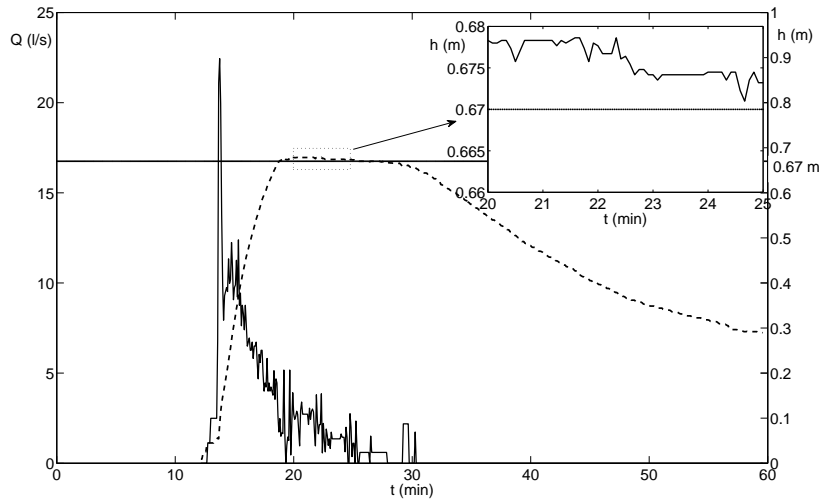
Figure 2.4: Example of the measured water level $h(t)$ (dotted line) and of the corresponding discharge entering into the stilling basin $Q(t)$ (thick continuous line), assessed through equation (2.1). The insert highlights the fluctuations of the water level in the stilling basin. Modified after Gregoretti et al. (2016b).

fillings and restorations of the sharp-crested weir facility.

2.1.3   Rainfall measurement

For a better evaluation of the precipitation fallen during convective events, another rain gauge is placed upstream the catchment, on the Pomagagnon Fork (2180 m a.s.l). The rain gauges, namely that of the Dimai monitoring station and that placed on the Pomagagnon Fork, are 188 m and 300 m respectively far from the centroid of the investigated watershed and are 500 m from each other. Their areas of influences have been obtained using the Thiessen polygons (Figure 2.1). The rain gauge on Pomagagnon Fork covers about 25% of the total catchment area, while the area of influence of the lower rain gauge is the remaining 75%. For the analysis, we assumed that hyetographs measured by rain gauges correspond to the centre of respective Thiessen polygons (squares of Figure 2.1), shifted in time according to the convective cell travelling velocity.

Table 2.2: Sharp-crested weir, significant events since 2011.

Date	Description
Summer 2011	
May, 13	Starting of the monitoring period (without sharp-crested weir)
July, 4	Debris flow event
August, 14	Installation of the sharp-crested weir
August, 18	Debris flow event and filling of the stilling basin
September, 20	End of the monitoring season
Summer 2012 - No monitoring activity	
Summer 2013	
May, 28	Starting of the monitoring period (without sharp-crested weir)
July	Restoring of the stilling basin
July, 26	Installation of the sharp-crested weir
August, 4	Stilling basin partially filled by sediments
August, 8	Emptying and restoring of sharp-crested weir facility
October, 25	End of the monitoring season
Summer 2014	
June, 12	Starting of the monitoring period (without sharp-crested weir)
June, 20	Missing in power supply - monitoring station turned off
July	Restoring of the stilling basin
July, 10	Change of batteries and monitoring station restoring
July, 15	Failure of solar panel and missing battery recharge
July, 18	Installation of the sharp-crested weir
August, 2	Change of solar panel and monitoring station restoring
October, 27	End of the monitoring season
Summer 2015	
June, 4	Starting of the monitoring period
June, 7	Stilling basin completely filled by sediments
June, 30	Crash of the central unit and data loss
July, 11	Emptying and restoring of the sharp-crested weir facility
July, 25	Stilling basin partially filled by sediments
July, 29	Stilling basin completely filled by sediments
August, 2	Emptying and restoring of the sharp-crested weir facility
September, 13	Stilling basin partially filled by sediments
October, 2	Emptying and restoring of the sharp-crested weir facility
November, 19	End of the monitoring season
Summer 2016	
May, 25	Starting of the monitoring period
June, 18	Emptying of the stilling basin (Figure 2.6)
June, 23	Restoring of the sharp-crested weir facility
July, 8	Change of the sharp-crested steel plate
August, 14	Stilling basin completely filled by sediments
August, 29	Partially emptying of the stilling basin
September, 12	Partially emptying of the stilling basin
September, 21	Emptying and restoring of the sharp-crested weir facility
October, 21	End of the monitoring season
Summer 2017	
May, 30	Starting of the monitoring period
July, 14	Stilling basin completely filled by sediments

Figure 2.5: On the left, the situation found after the rockfall occurred on August 2011; on the right, the cracked boulder, before removal.

For example, on August 19th, 2013 (Figure 2.7) the convective cell moved from North to South, affecting the Pomagagnon Fork 5 minutes earlier than the Dimai monitoring station. Considering the distance between the two rain gauges, the travelling rate of the rainfall cell was about 500 m in 5 minutes. In this case, the precipitation at the upstream polygon centroid corresponds to that measured by the Pomagagnon Fork rain gauge, postponed by 2 minutes, while rainfall fallen in the downstream polygon matches to that measured by the monitoring station, brought forward of 1.5 min.

Figure 2.6: On the left, the situation found on the 27th of August 2016 at the sharp-crested facility during an habitual reconnaissance; on the right, emptying of the basin like Egyptians.
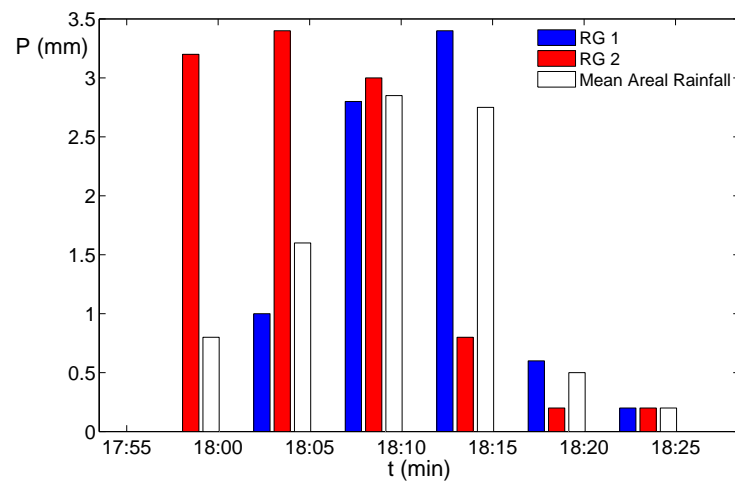
Figure 2.7: The rainfall depths of the 19 August 2013, recorded each five minutes by the rain gauges installed at the monitoring station Dimai (RG1) and in Pomagagnon Fork (RG2), are compared to mean areal rainfall values obtained through Thiessen polygons. Modified after Gregoretti et al. (2016b).

2.2 Collected data

Automatic stations are useful to collect a huge amount of continuous data, without the requirement of a physical presence. Data are usually recorded in text files and videos. For the monitoring station placed in the Dimai watershed, text files represent 2 tables:

1. The first chart contains data recorded in the normal mode, namely every 5 minutes as reported in Table 2.3. Columns in the chart represent: *TIME STAMP* the end time of the 5 minutes monitored interval, *RN* the count of recorded intervals, *BATT* the current battery voltage, *PA01/02/03* the output voltage of pressure transducers buried in the scree, *BARO* the voltage corresponding to atmospheric pressure, *STRM* the output voltage related to the water level in the stilling basin, *EN* the count of occurred alarms, and *Rain* the rainfall depth fallen in the previous 5-minutes interval.

2. 5-second data are contained in the chart of alarm mode (Table 2.4). Symbols have the same meaning of the normal mode table.

Table 2.3: Dimai monitoring station, header of normal mode table.

TIME STAMP	RN	BATT Volts	PA01	PA02	PA03 mVolts	BARO	STRM	EN	Rain mm
07/26 12:35	0	13.23	1069.44	1069.69	1094.73	543.87	404.95	0	0
07/26 12:40	1	13.23	1069.65	1069.86	1094.74	543.95	405.85	0	0.2

Table 2.4: Dimai monitoring station, header of alarm table.

TIMESTAMP	RN	PA01	PA02	PA03	BARO	STRM
26/07/2016 18:34:40	0	1071	1071	1095	548.2	405
26/07/2016 18:34:45	0	1071	1072	1094	548.4	405.2

Videos are acquired by the monitoring station cameras when the alarm mode is triggered (Section 2.1.1). The only continuous operative video camera is that

placed in front of the sharp-crested weir facility. This time-lapse camera was set to acquire 1 frame every 60 seconds in 2013; the acquisition time was reduced to 20 seconds from 2014. The video camera is only operational during daylight hours.

The sharp-crested facility was completed in 2011. Up to June 2017, about twenty significant runoff events were observed, and in twelve cases (15 August 2011; 9 August 2013; 19 August 2013; 24 August 2013; 12 August 2014; 31 August 2014; 4 August 2015; 3 September 2015; 13 July 2016; 5 August 2016; 9 August 2016; 21 June 2017) discharge was successfully measured. In the other events, the measurement failed because of rockfall, uncorrected positioning of the pressure transducer, or missing power to the central unit (see Table 2.2). Figures 2.8 and 2.9 show the measured hyetographs recorded by the Dimai and Pomagagnon Fork rain gauges and the generated runoff hydrographs (the hydrographs in 2.8 have been already displayed by Gregoretti et al. (2016b)). In all but two cases, the runoff rises to a peak in a short time and then decreases quite rapidly to reach a nearly horizontal plateau. Only the discharges observed on 24 August 2013 and on 9 August 2016, exhibited a secondary, less steep maximum. Finally, discharges fall abruptly to zero. In general, the measured runoff can be sketched as a hydrograph composed of two rectangles: a high and narrow initial rectangle, followed by a wider and shorter second rectangle. The characteristics of the discharges and of the inducing rainfalls are reported in Table 2.5. The observed runoff events did not trigger any debris flow. Since the setup of the monitoring station (July 2010, one year before the installation of the sharp-crested weir), only two debris flows occurred in the scree downstream (July and August 2011). The triggering rainfall recorded by the rain gauge of the Dimai station were 22.6 and 16.2 mm in thirty and ten minutes respectively, i.e. characterized by intensities much higher than those reported in Table 2.5. In Table 2.6, the events that filled the sharp-crested weir facility are reported. Due to the absence of continuously recorded video, we cannot neither distinguish the

Event	Time (GMT+0)	AMC	P_5 (mm)	P (mm)	T (min)	I (mm/h)	I_{MAX} (mm/h)	Q_P (l/s)	t_L (min)	t_{LC} (min)	C_{PQ}	t_P (s)	V_R (m³)
08/15/2011	04:45	1	6.4	14.4	515	1.7	7.2	0.25	28				0.54
08/09/2013	22:30	2	12.8	5.4	85	3.8	14.4	10.2	9	15	0.34	20	7.3
			10.0	5.2	90	3.5	9.6		19	20	0.29		
			12.8	5.2	90	3.5	11.9		12	18	0.31		
08/19/2013	18:00	1	0.4	8.0	25	19.2	45.5	22.4	3.5	4	0.32	60	3.5
			0.4	11.2	35	19.2	40.8		10	7	0.38		
			0.4	8.8	35	15.2	39.6		6	7	0.35		
08/24/2013	23:05	1	11.0	26.4	170	9.3	21.6	15.8	1	32	0.47	20	44.7
			12.8	25.6	175	8.8	19.2		10	40	0.38		
			11.5	26.2	178	8.8	21.0		4	35	0.43		
08/12/2014	14:35	1	7.4	11.2	120	5.6	36.0	15.7	6	8	0.55	40	4.2
			12.4	11.6	120	5.8	45.6		5	8	0.62		
			8.7	11.3	120	5.6	38.5		6	8	0.57		
08/31/2014	17:25	1	10.6	11.6	95	7.3	24.0	12.9	5	5	0.32	70	10.2
08/04/2015	17:45	3	41.6	15.8	70	13.5	50.4	28.6	9	13	0.58	75	33.4
			44.0	13.4	70	11.5	40.8		8	14	0.59		
			42.2	15.2	70	13.0	46.2		9	13	0.62		
09/03/2015	22:10	1	5	13.8	70	11.8	31.2	34.4	11	12	0.56	90	48.9
			5	14.2	70	12.2	28.8		15	17	0.59		
			5	13.9	70	11.9	28.2		12	15	0.58		
07/13/2016	12:40	3	41.2	10.2	55	11.1	55.2	28.5	5	11	0.32	30	26.6
			44.0	9.2	60	9.2	50.4		7	11	0.31		
			42.2	10	60	10.0	50.4		5	11	0.33		
08/05/2016	07:25	2	27.2	22.6	145	9.4	36.0	20.6	10	17	0.71	90	55.3
			26	14.8	155	5.7	28.8		12	17	0.61		
			26.9	20.7	155	8.0	31.8		10	17	0.71		
08/09/2016	16:45	3	38.2	43.0	285	9.1	43.2	38.8	73	170	0.22	90	238.3
			30.4	39.8	285	8.4	43.2		75	170	0.22		
			36.3	42.4	285	8.9	43.2		74	170	0.22		
06/21/2017	18:55	2	13.0	8.2	30	16.4	50.4	13.3	5	8	0.35	50	5.8

Table 2.5: Relevant features of observed rainfall events that produced runoff up to June 2017. AMC: antecedent moisture conditions; P_5: previous five days rainfall height; P: rainfall heights; T: rainfall duration; I: mean rainfall intensity; I_{MAX}: maximum rainfall intensity computed over a five minutes duration; Q_P: peak runoff discharge; t_L: lag time computed as the distance between the rainfall centroid and the peak discharge; t_{LC}: lag time computed through cross-correlation between temporal distributions of rainfall and flow discharge; C_{PQ}: cross-correlation coefficient; t_P: time initially taken by the runoff discharge to grow from zero up to the peak value; V_R: runoff volume. The three values reported for P_5, P, t, I, I_{MAX}, t_L, t_{LC}, C_{PQ} correspond to rainfalls provided by the rain gauges of Dimai, Pomagagnon Fork and their areal mean, respectively. During the events of August 15th, 2011 and August 31th, 2014 the rainfall was measured only by the Dimai rain gauge.
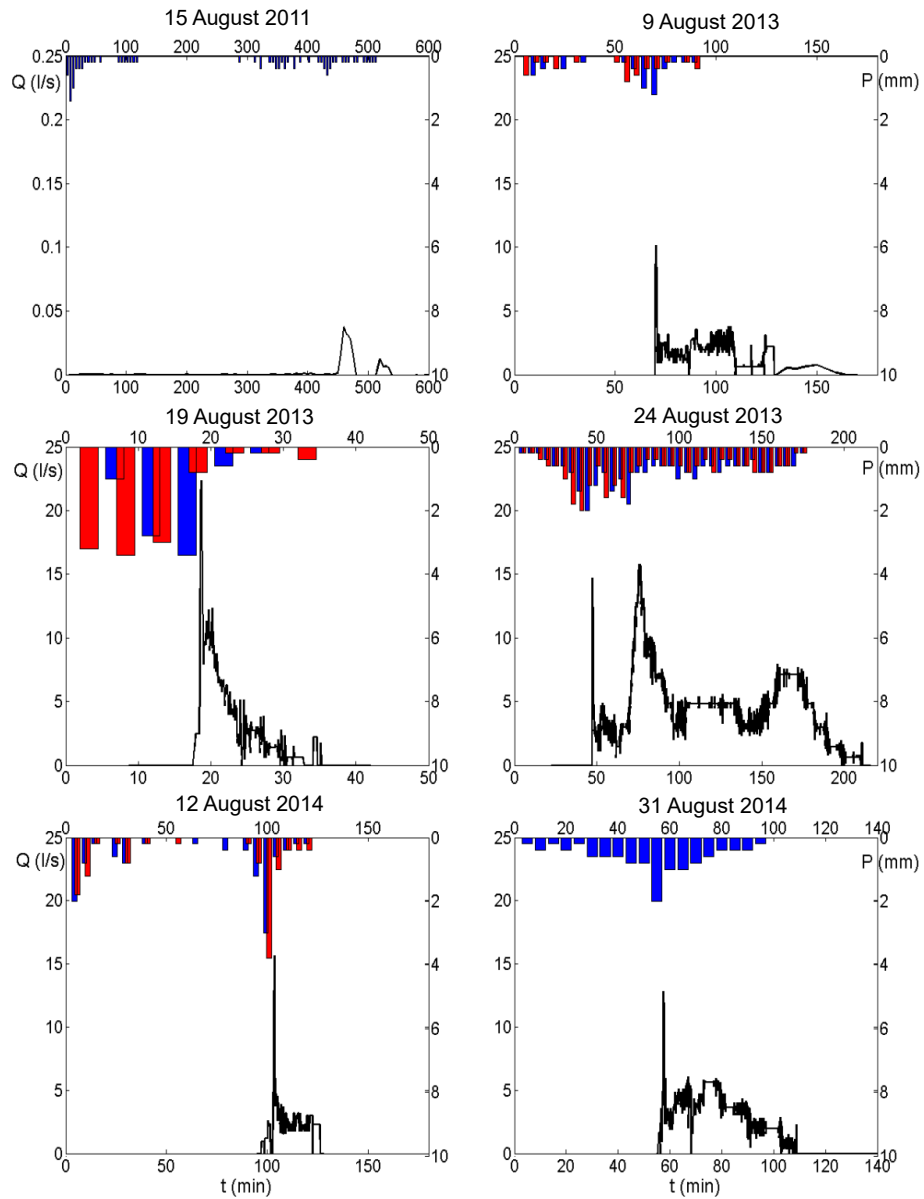
Figure 2.8: Runoff discharge hydrographs measured for six rainfall events during the period 2011-2014. These discharges have already been presented by Gregoretti et al. (2016b). Top panels refer to the events observed on 15 August 2011 (left) and 9 August 2013 (right). Middle panels refer to the events observed on August 19 (left) and 24 (right), 2013. Bottom panels refer to the events observed on 12 August (left) and 31 (right) 2014. Red bars correspond to the rainfall recorded by Pomagagnon Fork rain gauge while blue bars correspond to the rainfall recorded by Dimai monitoring station. Recorded 5-minute rainfalls are represented shifted in time, being referred to the centre of the relevant Thiessen polygon. For each event, time origin is reported in Table 2.5.
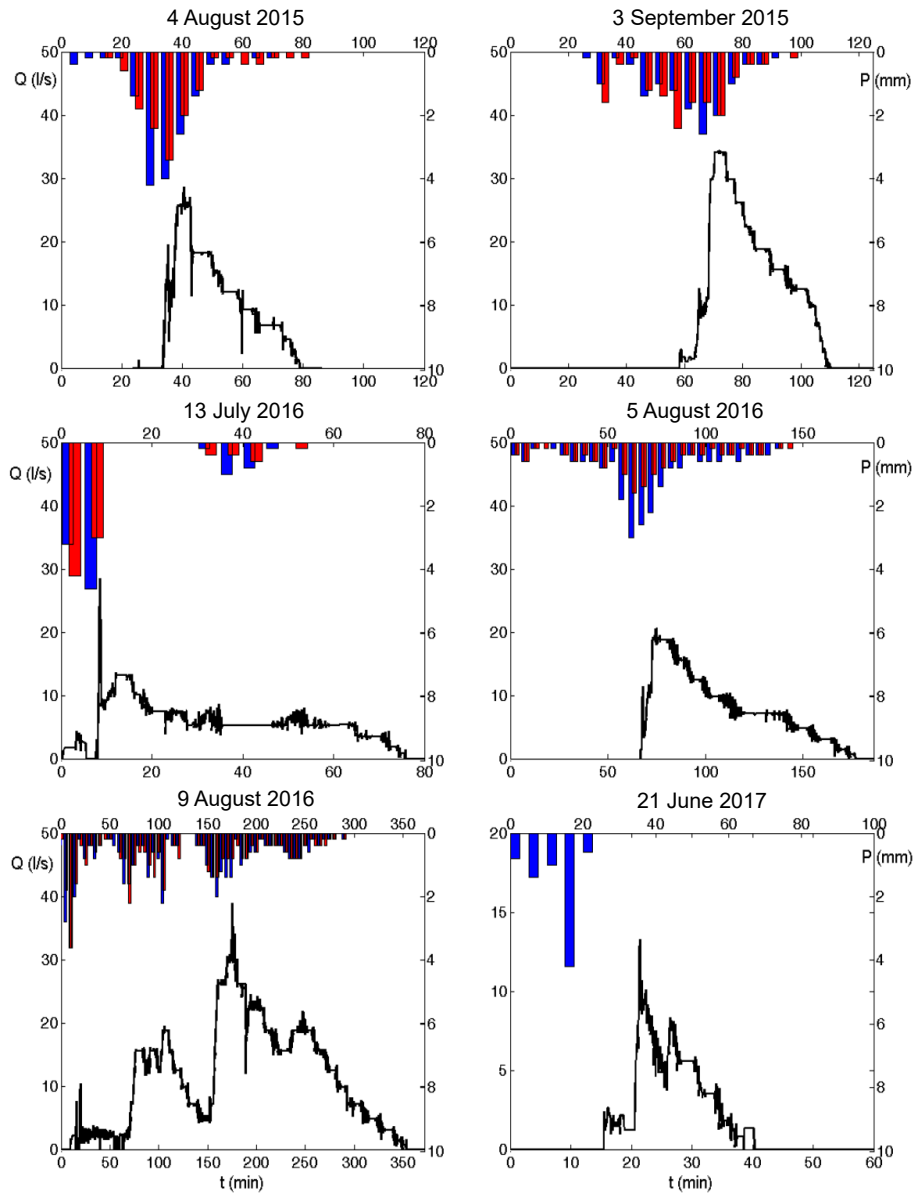
Figure 2.9: Runoff discharge hydrographs measured for five rainfall events during the period 2015-2017. Top panels refer to the events observed on 4 August (left) and 3 September (right) 2015. Middle panels refer to the events observed on 13 July (left) and 5 (right) August 2016. The bottom panelS refers to the event occurred on 9 August 2016 (left) and 21 June 2017 (right). Red bars correspond to the rainfall recorded by Pomagagnon Fork rain gauge while blue bars correspond to the rainfall recorded by Dimai monitoring station. Recorded 5-minute rainfalls are represented shifted in time, being referred to the centre of the relevant Thiessen polygon. For each event, time origin is reported in Table 2.5.

Table 2.6: Relevant features of observed rainfall events that produced mass transport up to 2016. AMC: antecedent moisture conditions; P_5: previous five days rainfall height; P: rainfall heights; T: rainfall duration; I: mean rainfall intensity; I_{MAX}: maximum rainfall intensity computed over a five minutes duration.

Event	AMC	P_5 (mm)	P (mm)	T (min)	I (mm/h)	I_{MAX} (mm/h)
04-07-11	1	7.4	22.6	40	33.9	64.8
18-08-11	2	17.8	16.2	10	97.2	98.4
04-08-13	1	3.6	21.4	75	17.1	57.6
07-06-15	1	9.8	13.8	20	41.4	69.6
25-07-15	1	12.2	18.2	30	36.4	69.6
29-07-15	3	30.2	16	30	32.0	52.8
14-08-16	3	58.2	18	35	30.9	86.4
13-07-17	2	17.2	28.2	180	9.2	2.6

type of movement, nor estimate a discharge value.

2.3   Hydrological modelling

An accurate simulation of runoff is required to predict debris-flow initiation downstream. Starting from the model proposed by Gregoretti and Dalla Fontana (2008), we introduced substantial and physically based modifications useful to improve the performance of the model.

Estimation of excess rainfall

In the model of Gregoretti and Dalla Fontana (2008), the excess rainfall P_e contributing to runoff discharge is determined by the SCS-CN method (Soil Conservation Service, 1972):

$$P_e(t) = \begin{cases} 0 & t \leq t_{I_a} \\ \frac{(P(t)-I_a)^2}{P(t)-I_a+S} & t > t_{Ia} \end{cases} \tag{2.3}$$

where $P(t)$ is the rainfall height at time t, I_a considers the initial losses, t_{I_a} is the time within I_a occurs, and S is the potential maximum retention. The

latter two quantities (expressed in millimetres) are linked to the runoff curve parameter CN through the relations:

$$S = 25.4\left(\frac{1000}{CN} - 10\right), \qquad I_a = 0.1\,S \tag{2.4}$$

The original equation $I_a = 0.2S$ was changed to $I_a = 0.1S$ by Gregoretti and Dalla Fontana (2008), because $I_a = 0.2S$ is considered excessively high for mountain environment (Hawkins et al., 2008; D'Asaro and Grillone, 2012). The SCS-CN method is used to compute the excess rainfall at each time step for every cell by which the basin is subdivided. The parameter CN is empirical and depends on soil type, land use, and moisture conditions antecedent to rainfall (AMC), commonly classified as dry ($AMCI$), normal ($AMCII$) and wet ($AMCIII$) (see Section 1.2). Considering the curve numbers for normal AMC (CN(II)), equivalent curve numbers can be assessed by:

$$CN(AMC) = \frac{aCN(II)}{10 - bCN(II)} \tag{2.5}$$

where $a = 2.08454e^{0.80709AMC} - 0.47225$, $b = \dfrac{a - 4.2}{100} - 0.058$, and AMC corresponds to dry (I) or wet (III) conditions (Chow et al., 1988). Originally, the SCS-CN method was developed for flat/hilly watershed; to adapt it to steep headwater catchments, some adjustments are needed. In the presence of high slopes and nearly impervious soils, rainfall tends to flow superficially rather than to infiltrate, and the infiltration occurs in the large fissures rather than through the soil pores; at the same time, rainfall interception by vegetation is scarce or even absent. As shown by Eli and Lamont (2010), the SCS-CN relationship is not an infiltration equation, and its use is not appropriate for evaluating the incremental rainfall excess during a storm event. Consequently, a modification to the computation of the effective rainfall is necessary to better estimate the discharge. Following the approach of Grimaldi et al. (2013), we developed a procedure in which we coupled the SCS-CN method with a more proper infiltration

equation. Grimaldi et al. (2013) simulated about one hundred runoff events in four US basins after joining the excess rainfall computed through the SCS-CN method with the Green-Ampt infiltration equation. Anyway, the Green-Ampt equation is not suitable for catchment as that monitored in this work. As remarked before, high slopes facilitate overland runoff rather than saturation, whereas the high fracturing degree of rocky outcrops promotes the infiltration (Marchi et al., 2008). To validate these observations, field experiments of runoff generation in steep carbonatic rocky outcrops (dolomite/limestone) show that the the dominant mechanism of runoff generation is infiltration excess or Hortonian flow process (Lange et al., 2003; Li et al., 2011) as in the semi-arid areas (Beven, 2002). The original Horton equation consider the use of three parameters to estimate the excess rainfall. This approach could be problematic because data on both the initial value of the infiltration rate and the decay constant for rocky terrains are almost unknown, as well as their dependence on the initial moisture conditions. For this reason a basic behaviour of infiltration is considered, coupling a simplified version of the Horton equation (constant infiltration rate f_c) with the SCS-CN method (hereafter called SCS-CNH):

$$P_e(t) = \begin{cases} 0 & t \leq t_{I_a} \\ \frac{(P(t)-I_a)^2}{P(t)-I_a+S} & t > t_{I_a}, I < f_c \\ P_e(t-\Delta t) + P(t) - P(t-\Delta t) - f_c\Delta t & t > t_{I_a}, I > f_c, P_e < P_{e_{SCS}} \end{cases}$$
$$(2.6)$$

Here, I refers to the mean rainfall intensity during a time step Δt and $P_{e_{SCS}}$ is the excess rainfall of the precipitation computed through the SCS-CN method. As explained before, the lack of knowledge about initial infiltration rates and decay constants for rocky surfaces pushed us to simply use a constant infiltration rate, replacing the rapid decreasing limb of the Horton equation with the initial abstraction of the SCS-CN method. The parameter f_c considers the effects on infiltration of both slope and terrain composition (Wilson, 1990). The higher the slope, the more rainfall tends to flow over the surface than percolate into the

rock fissures. Hence, excess rainfall could be generate also for rainfalls which intensities do not exceed the infiltration rate f_c. In this way, when rainfall is lower than f_c, this procedure provides the excess rainfall using the SCS-CN method, while the Horton approach works when the rainfall intensity exceeds the infiltration rate.

Routing model

The former model, of Gregoretti and Dalla Fontana (2008) computes the flow paths from each cell to the outlet along the steepest direction and the corresponding travel times as the ratio between flow path length and assigned time invariant runoff velocity. Travel times t_T allow the computation of flow discharge $Q(t)$, given by the sum of all the excess rainfall pulses $P_e(\vec{x}, \tau)$ precipitated on basin cells dA at location $\vec{x}$ and time $\tau = t - t_T(\vec{x})$, that reach the outlet at the same time step:

$$Q(t) = \int_A P_e(\vec{x}, \tau) \, dA \qquad (2.7)$$

The overall travel time t_T is assessed by:

$$t_T(\vec{x}) = \frac{L_C(\vec{x})}{U_C} + \sum_{i=1}^{N} \frac{L_{Si}(\vec{x})}{U_{Si}} \qquad (2.8)$$

where L_C is the channel path length, U_C is the runoff channel velocity, L_{Si} is the path length along the i-th sloping surface, and U_{Si} is the corresponding runoff velocity, depending on the N types of terrain. Each flow path is extracted along the steepest topographic direction by means of the D8 method (Tarboton, 1997), after removing pits or flat regions. Moreover, it is divided into hillslope and channel paths for accounting the different velocities, typical of distinct regions of the watershed (Botter and Rinaldo, 2003; Grimaldi et al., 2012). Hillslopes are divided according to the land use (rock, scree and wooded) because runoff slope velocity is assigned considering surface characteristics (Saco and Kumar, 2004). On the other side, channel paths are extracted considering the DTM

maps (Montgomery and Foufoula-Georgiou, 1993). Channel velocity is assumed constant during the entire duration of the event and equal to that characterizing the discharge peak (Q_p). It is obtained solving iteratively the Gauckler-Strickler uniform flow equation $U_C = k_s R_h^{2/3} i_f^{1/2}$ at the closure section of the basin, until $U_C \, \Omega = Q_{max}$. Here, k_s is the Gauckler-Strickler friction coefficient, R_h and Ω are respectively the hydraulic radius and the cross-sectional area of the channel at the outlet, and $i_f = sin\alpha$, with α the bed slope angle.

The developed improvement for the model accounts for along channel variations of U_C by means of a matched diffusivity kinematic-wave model (Orlandini and Rosso, 1996) to route the runoff along the channel. According to Woolhiser and Liggett (1967), the kinematic wave approximation is accurate for simulating flow routing in the examined rocky channel whose average slope is 238%. Rengers et al. (2016) stated that, for these high-slope catchments, the differences between results obtained with kinematic wave assumptions and full shallow water equations are negligible. The finite differences numerical solution of the standard kinematic model is affected by numerical diffusion that counteracts the tendency of wave to steepen with results depending on the grid size (Ponce, 1991). This numerical diffusion is because of truncation errors and, in general, there is no way to determine if this dispersion matches with the hydraulic diffusivity of the wave. Furthermore, the accurate modelling of a small hydraulic diffusivity linked to an impulsive hydrograph cannot be obtained by using a standard numerical solution of the kinematic wave model (Orlandini and Rosso, 1996). This inconvenience is overcome by integrating the diffusion wave model by using the Muskingum-Cunge method where numerical diffusion matches the hydraulic diffusivity; with this approach, the solution becomes grid-size independent, unconditionally stable, and physically realistic. Thereby, the Muskingum-Cunge method can be used for modelling waves with a small hydraulic diffusion, as those represented by the kinematic wave approximation

(Ponce, 1991). The governing flow equation is:

$$\frac{\partial Q}{\partial t} + c_k \frac{\partial Q}{\partial s} = D_h \frac{\partial^2 Q}{\partial s^2} + c_k q_L \qquad (2.9)$$

where c_k is the celerity of the kinematic flood wave, D_h is the hydraulic diffusivity, and q_L is the lateral inflow per unit length, computed according:

$$q_L(t) = \frac{1}{\Delta x} \int_{A_S} P_e(\vec{x}, \tau) \, dA_S \qquad (2.10)$$

where A_S is the area of the watershed drained by the cell adjacent to the channel that supplies it runoff, Δx is the cell size, $P_e(\vec{x}, \tau)$ is the excess rainfall at location $\vec{x}$ and time $\tau = t - t_{TS}(\vec{x})$. The slope travel time t_{TS} is defined as the ratio of path length along slope to hillslope velocity:

$$t_{TS}(\vec{x}) = \sum_{i=1}^{N} \frac{L_{Si}(\vec{x})}{U_{Si}} \qquad (2.11)$$

The partial differential equation (2.9), is solved through the Muskingam-Cunge method, and leads to the following linear algebraic equation (Orlandini and Rosso, 1996):

$$Q_{i+1}^{j+1} = C_1 \, Q_i^{j+1} + C_2 \, Q_i^{j} + C_3 \, Q_{i+1}^{j} + C_4 \, q_{L,i+1}^{j+1} \qquad (2.12)$$

where Q_{i+1}^{j+1} is the runoff at the cell $(i+1)\Delta s$ and time $(j+1)\Delta t$, while $q_{L,i+1}^{j+1}$ is the lateral inflow rate at the $(i+1)-$th space interval and $(j+1)-$th time interval that is provided by the equation 2.10. The routing coefficients C_i $(i = 1, 4)$ are:

$$C_1 = \frac{c_k(\Delta t/\Delta s) - 2X}{2(1 - X) + c_k(\Delta t/\Delta s)} \tag{2.13}$$

$$C_2 = \frac{c_k(\Delta t/\Delta s) + 2X}{2(1 - X) + c_k(\Delta t/\Delta s)} \tag{2.14}$$

$$C_3 = \frac{2(1 - X) - c_k(\Delta t/\Delta s)}{2(1 - X) + c_k(\Delta t/\Delta s)} \tag{2.15}$$

$$C_4 = \frac{2c_k\Delta t}{2(1 - X) + c_k(\Delta t/\Delta s)} \tag{2.16}$$

$$\tag{2.17}$$

where X is a weighting factor matching the numerical and hydraulic diffusivity defined as:

$$X = \frac{1}{2}\left(1 - \frac{2D_h}{c_k\Delta s}\right) \tag{2.18}$$

By relating channel width and flow discharge through a power law (Leopold and Maddock, 1953), and expressing the flow resistance through the Gauckler-Strickler relation, it results that (Orlandini and Rosso, 1996):

$$D_h = \frac{3\,Q^{1-b_1}}{2\,(3 + 2b_1)\,\mathcal{B}\,\tan\beta} \tag{2.19}$$

where $\mathcal{B}\ (= \mathcal{B}_0(A/A_0)^{b_2})$ is a width parameter associated with the upstream drainage area A, the outlet width $\mathcal{B}_0$, and the catchment area A_0, and Q is provided by the following expression:

$$Q = \mathcal{B}^{-2/(3+2b_1)}\,k_s^{3/(3+2b_1)}\,S_f^{3/[2(3+2b_1)]}\,\Omega^{5/(3+2b_1)} \tag{2.20}$$

with S_f the energy slope, Ω the flow area, and b_1 a suitable morphological exponent (Leopold and Maddock, 1953). The final expression for the kinematic wave celerity, $c_k = dQ/d\Omega = [5/(3 + 2b_1)]Q/\Omega$, reads:

$$c_k = \frac{5}{3 + 2b_1}\,\mathcal{B}^{-2/5}\,k_s^{3/5}S_0^{3/10}\,Q^{2/5(1-b_1)} \tag{2.21}$$

The values of X and c_k are computed by means of equations (2.18) and (2.21) for each pixel, after extracting local bed slope values from the DEM model and taking $Q = (Q_i^j + Q_{i+1}^j + Q_i^{j+1})/3$. The lateral inflow $q_{L,i+1}^{j+1}$ is provided by the hydrographs of the cells adjacent to the channel. Setting $\mathcal{B}_0$ from field observations and assuming $b_1 = 0.26$ (Leopold and Maddock, 1953; Orlandini and Rosso, 1996), the only calibration parameter of the model is the roughness coefficient k_s.

The hydrological model, above presented, has already been discussed and published in Gregoretti et al. (2016b).

2.4 Testing sites

Jointly with the data collected from the Fiames site, data of two other monitoring stations were used. The monitored sites, called Acquabona Punta Nera and Rovina di Cancia, are located in the same area, 8 and 15 km far from the Dimai watershed respectively (see Figure 2.10). The rocky formations, characterizing the two basins, are the same of Dimai.

Acquabona Punta Nera basin

The basin of Acquabona Punta Nera is located in the municipality of Cortina d'Ampezzo, on the left side of the Boite valley, delimited by the western slope of the Sorapis Group. It origins at the feet of Punta Nera (2738 m a.s.l.), develops downstream encountering the national road 51 at 1115 m a.s.l., and is confined by the Boite river (Figure 2.11). Acquabona has a history of debris flows, which have been monitored in the past (Berti et al., 1999, 2000; Tecca et al., 2003; Tecca and Genevois, 2009). However, this basin is not the subject of the cited works, but is adjacent. Two collapses of Punta Nera vertical cliffs occurred on spring 2015 and 2016, generating a huge amount of loose available sediments. The debris materials mainly deposited on the rocky channel incising the Punta Nera cliffs. Subsequent rainfalls mobilized these sediments, triggering debris
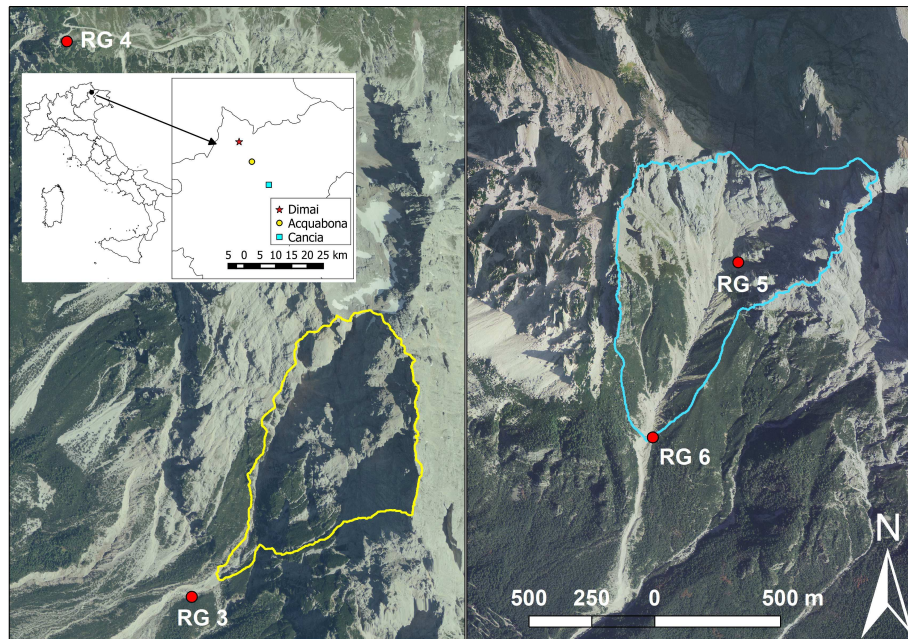
Figure 2.10: Aerial view of Acquabona Punta Nera (left), and Rovina di Cancia (right), with the positions of the reference rain gauges: Acquabona Punta Nera (RG3), Faloria (RG4), and Rovina di Cancia (RG5, RG6).

flows that incised a new channel in the scree slopes. The triggering area (1545 m a.s.l.) lies just downstream of a rock drop, where superficial discharges form a waterfall that hits the underlying debris deposit. In Table 2.7, we summarize the main features of the watershed extracted from a 1-m DEM obtained by using a Lidar survey carried out on October 2015. The sampling density of the Lidar survey has been 4 points/m^2.

A monitoring station was set up on July 2016, 100 m downstream the drop. It is equipped with a rain gauge, a thermometer, an anemometer, two pressure transducers buried in the middle of the channel about 0.3 m below the surface, and two time-lapse cameras; all instruments are managed by a remotable control unit (Campbell CR1000). The pressure transducers are of piezoresistive type (Keller, series 26W), operating in the range 0-0.5 bar (output signal 400-2000 mV). The time-lapse cameras are Brinno TLC 200 and record the images on a SD card, capturing a frame each two seconds. Data are ordinarily sampled at 5
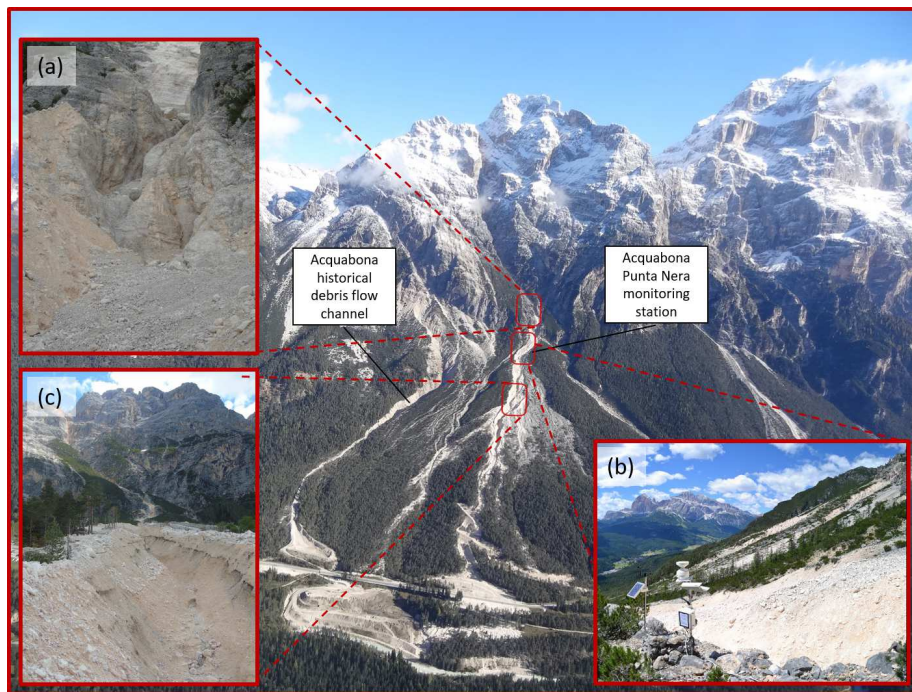
Figure 2.11: Front view of the Acquabona Punta Nera watershed incised by the debris flow channel. The inserts show some typical locations along the debris flow channel: (a) rock chute at the end of the rocky channel, (b) monitoring station placed by the University of Padova at the initiation area, (c) typical v-shape of the channel in the transportation zone. The central panel shows the location of the monitoring station, corresponding to RG3 (Figure 2.10), and the location of the Acquabona historical debris flow channel (Berti et al., 1999).

minutes intervals. When rainfall depth exceeds the value of 0.6 mm in 150 seconds, the station switches in alarm mode, cameras turn on and acquisition time decreases to five seconds. The five seconds sampling period and the shooting time last two hours. After this time, the alarm mode is prolonged of other two hours if the rainfall intensity exceeds again the threshold value.

Rovina di Cancia basin

The basin of Rovina di Cancia is located in the municipality of Borca di Cadore, on the left side of the Boite river valley, delimited by the western slope of the Mount Antelao. It origins at Salvella Fork (2451 m a.s.l.) and develops

Table 2.7: Acquabona Punta Nera headwater basin, morphological characteristics extracted from a 1-m resolution DEM obtained from a Lidar survey accomplished on 2015.

Area (km^2)	0.490
Min elevation (m a.s.l.)	1546
Mean elevation (m a.s.l.)	2285
Max elevation (m a.s.l.)	2847
Mean slope (º)	62.5
Max slope (º)	89.1
Channel mean slope (º)	47.5
Land use	70% bare rock
	20% Scree and active erosion
	10% moors and heathland

downstream encountering the confluence with the Bus del Diau affluent on the left side at 1340 m a.s.l., and the village of Borca di Cadore (880 m a.s.l). The Boite river delimits the downstream side of the basin (Figure 2.12). Considering the downstream limit of the Boite river, the drainage area is 2.4 km^2 while 1.8 km^2 at the confluence with Bus del Diau. The basin presents a slope varying from 70-80% in the upper part to 20-25% in the lower part (fan area). This basin has a history of debris flows, as reported in literature (Bacchini and Zannoni, 2003; Gregoretti and Dalla Fontana, 2008). For this reason, geological settings have been widely discussed also by Mantovani et al. (2002) and Deganutti and Tecca (2013). The basin could be divided in three characteristic areas: in the upper part massive rock cliffs prevail. The medium part of basin is characterized by screes of poorly sorted and highly permeable rock debris, with boulders of diameters up to 4 meters. The downstream part is covered by old debris flow deposits including postglacial sediment material. The triggering area of the debris flows is located at 1666 m a.s.l., where a giant rock retains a large quantity of sediments. At the initiation area, the channel descending from Mount Antelao drains a basin of area 0.65 km^2. In Table 2.8, we summarize the main features of the watershed extracted from the 1-m DEM obtained by using a Lidar survey carried out on October 2011.

On July 2014, a low-cost automated monitoring station was installed just
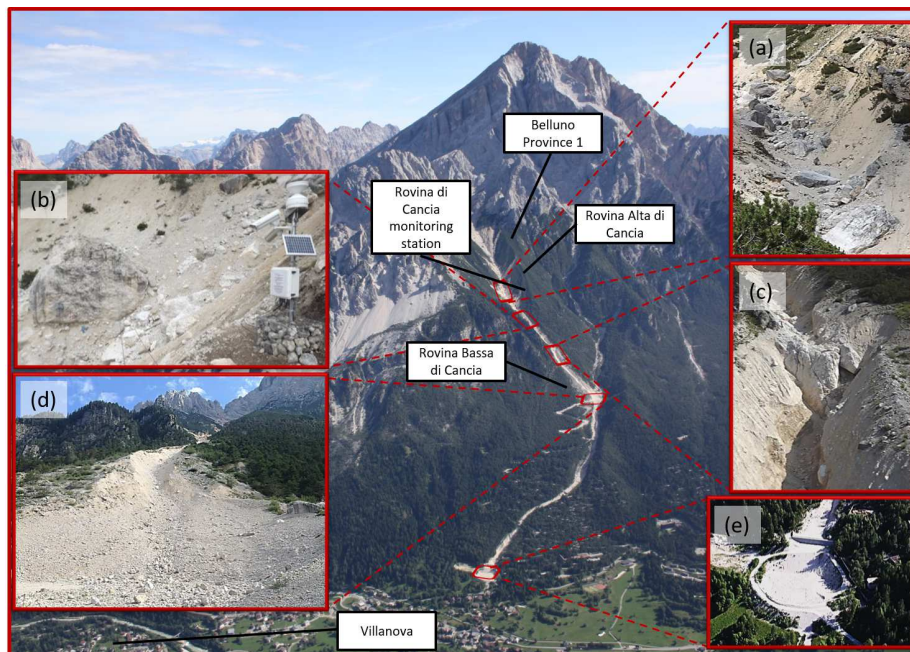
Figure 2.12: Front view of the Rovina di Cancia watershed incised by the debris flow channel. The inserts show some typical locations along the debris flow channel: (a) portion of the upper reach, (b) monitoring station placed at the initiation area, (c) rock drop at elevation 1500 m a.s.l., (d) the flat area dissecting the downstream reach of the channel, and (e) the gabion wall and retaining basin at the end of the channel. The central panel also shows the rain gauges present in the area: Belluno Province 1 and Rovina di Cancia monitoring station correspond to RG5 and RG6 (Figure 2.10).

in front of the giant rock. It is equipped with a rain gauge, a thermometer, two pressure transducers buried into scree, and two time-lapse cameras; all instruments are managed by a remotable control unit (Campbell CR800). The pressure transducers are placed in the middle of the channel, about 0.3 m below the surface. The instrumentation, namely pressure transducers and time-lapse cameras, the acquisition mode, and the sampling rates are the same described in the Acquabona Nera catchment section. In this basin a debris flow monitoring and warning system was installed by CAE S.p.A. on 2013. This monitoring system is managed by the Department Land Defence and Civil Protection of the Province of Belluno.

Table 2.8: Rovina di Cancia headwater basin, morphological characteristics extracted from a 1-m resolution DEM obtained from a Lidar survey accomplished on 2011.

Area (km^2)	0.654
Min elevation (m a.s.l.)	1662
Mean elevation (m a.s.l.)	2213
Max elevation (m a.s.l.)	3067
Mean slope (º)	54.2
Max slope (º)	87.8
Channel mean slope (º)	36.5
Land use	50% bare rock
	28% Scree and active erosion
	22% moors and heathland

Chapter 3

Results and discussion

3.1 Rainfall analysis

Before the hydrological modelling, a meticulous analysis of recorded rainfall events is necessary. Since the establishing of the Dimai monitoring station, about 220 rainfall events triggered the alarm mode. Observed rainfalls generally show two different patterns, a behaviour already observed by Gregoretti and Dalla Fontana (2007) in the same area: precipitations with low value intensities and no significant variations during the event, or highly variable rainfalls with the presence of short high-intensity episode, or burst. The definition of burst is not unique in literature: Berti and Simoni (2005) consider it as a period of intense rainstorm that exceeds an average value of 0.5 mm/5 min; Gregoretti and Dalla Fontana (2007) proposed a burst as a rainfall that begins when intensity exceeds 0.8 mm/5 min and ends when intensity drops below this value; Coe et al. (2008) defined it considering gaps between rain gauge bucket tips, setting in 10 min the minimum separation time of two consecutive storms. For extracting the rainfalls, we choose the approach followed by Coe et al. (2008). The recorded precipitations (taking into account only those that triggered the alarm mode) have been classified considering their capability to generate surface runoff, in order to understand how the catchment works in term of response

to the rain forcing. As explained in Section 1.3, the common variables for assessing watershed response are rainfall duration and mean intensity (equation 1.2). In Figure 3.1 the recorded events are plotted. Two different behaviours emerge: the former is the unclear separation between the events generating and non-generating surface runoff, the latter is the quite defined distinction between runoff events with and without mass transportation. The thresholds sketched in Figure 3.1 (a) are defined by the envelope of limit mean intensity values corresponding to different response in the Dimai watershed. In this way, ID thresholds delimit the maximum rainfall intensity values that did not generate surface runoff (dashed red line, equation 3.1), and the minimum mean rainfall intensity values that generated surface runoff (dashed black line, equation 3.2) or surface runoff with mass transportation (dashed blue line, equation 3.3).

$$I = 8.84D^{-0.83} \tag{3.1}$$

$$I = 3.60D^{-0.83} \tag{3.2}$$

$$I = 17.69D^{-0.50} \tag{3.3}$$

Due to the unclear division between runoff and no runoff events, we focus attention on precipitations lying between the thresholds given by equations 3.1 and 3.2. For each recorded precipitation, we extract its general features (duration, cumulative rainfall, mean and maximum intensities). Furthermore, we evaluate the moisture conditions of the soils in the watershed by calculating the pre-event cumulative rainfall for different time periods, i.e. from 1 to 5 days before each precipitation. For understanding which parameters are more useful to characterize the events, we perform two different kinds of regression on the binary variable *Yes/No runoff*: a linear model and a logistic one. We start from the more complex models, in which we consider every variable inherent to
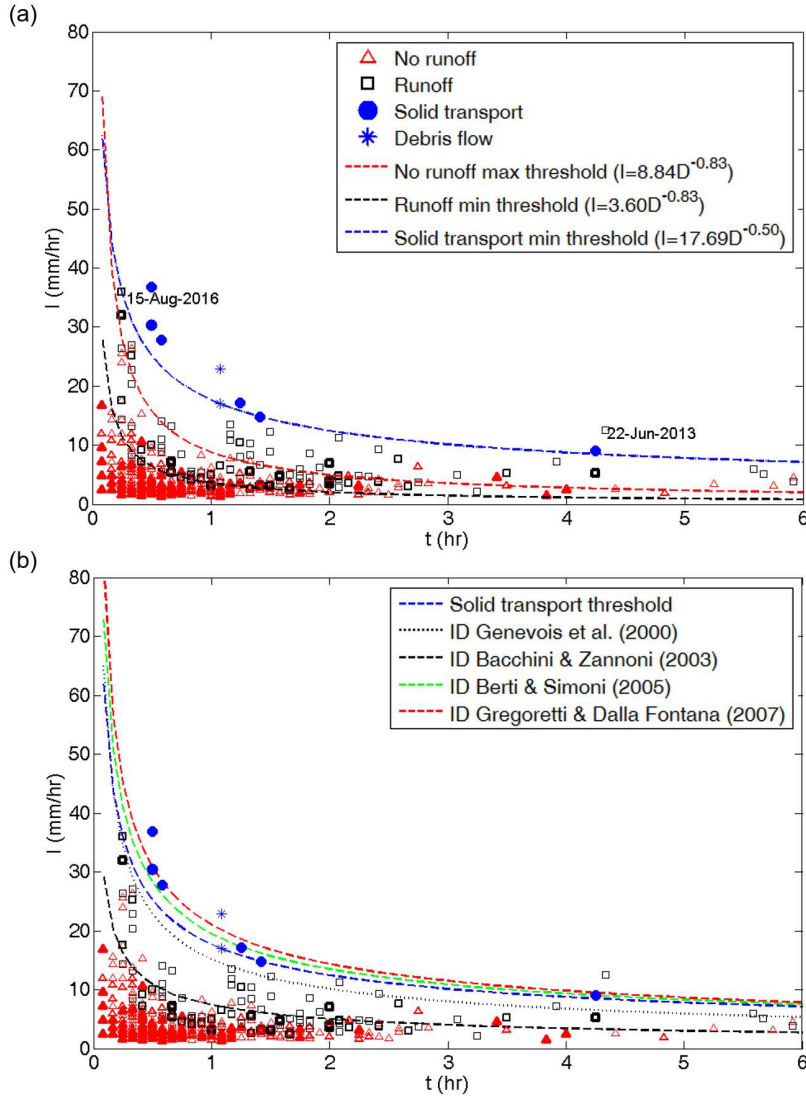
Figure 3.1: In the panel (a), analysis of rainfall mean intensity I (mm/hr) versus duration t (hr) of events recorded by the Dimai monitoring station. Highlighted thresholds indicates the envelope of maximum intensities without generated runoff (dashed red line), minimum intensities generating runoff (dashed black line), and mass transport (dashed blue line). In the panel (b), comparison with different ID thresholds developed for evaluating the debris flow triggering in the dolomitic environment. In both the panels, the thickness of indicators state the AMC of the event, from thinner (AMC I) to thicker (AMC III). AMC is computed considering for each event the cumulative rainfall of the previous two days (see Section 3.3).

precipitation features and every different-duration pre-event cumulative rainfall. We simplify the models applying a trial and error method, until remaining variables are significant for the regressions (*p-value* of Wald test lower than 0.05). The choice to follow a stepwise statistical approach for the selection of significant variables is in agreement with Cannon et al. (2010). The features that mainly influence the response of both the models are the event rainfall accumulation P (expressed in mm), and the antecedent moisture conditions. In more detail, the linear regression depends on the pre-event cumulative precipitations fallen during 1 day (*CR1*) and 2 days (*CR2*) before each event (expressed in mm), and on their interaction, whereas the logistic regression depends only on *CR2*. The equations describing the models are respectively:

$$Y = resc(-0.29 + 0.05CR1 + 0.02CR2 + 0.07P - 0.01CR1 \times CR2) \quad (3.4)$$

$$Y = \frac{1}{1 + e^{-5.17 + 0.29CR2 + 0.48P}} \quad (3.5)$$

where Y is a number varying from 0 to 1 that represents the statistical likelihood of runoff occurrence. The operator *resc* rescales the range of the linear regression to the range $[0, 1]$. Following Staley et al. (2017), we set a likelihood threshold of 0.5. We evaluate the ability of the models in discriminating the events with/without runoff. The occurrence could be positive or negative (success or failing in model prediction). Each event is assigned to a class. A true positive (*TP*) is an event with modelled and recorded runoff, while, vice versa, a true negative (*TN*) represents a neither modelled nor recorded runoff. False positives (*FP*) occur when an over-threshold rainfall event do not generate runoff, while false negatives (*FN*) indicate under-threshold rainfalls that generate discharge. The prediction rate improves but some errors remain. The linear regression mispredicts events in 27 cases on 100 (4 FP and 23 FN), and the logistic model gives 22 wrong predictions (8 FP and 16 FN). The linear regression predicts the TN events better than the logistic model but, on the other

hand, results the worst in predicting TP rainfalls. Two important statements can be however extracted from this analysis:

1. The separation between rainfall generating runoff and those generating no response remains unclear. Adding further features to the ID relationship drastically reduces but does not completely eliminate all the uncertain points;

2. The variables considered in the models seem to highlight how AMC might be assessed differently with respect to the SCS-CN standard practice, reported in Table 1.4.

The other investigated behaviour represents the almost clear separation between runoff events without and with mass transportation. Only two rainstorms that did not transport sediments overcome the threshold given by equation 3.3. The former is the event on June 22nd, 2013 that had a duration of 3 hours with a mean intensity of 17.5 mm/hr. The latter is the rainfall occurred on August 15th, 2016. This 15-minute event had a high maximum intensity (96 mm/hr) and a mean rate of 36 mm/hr. During the first rainstorm, the lack of solid transport can be explained by the presence of snow and ice that consolidated available sediments, whereas the second event occurred the day after a mass transportation event that washed out the channel and, probably, there was no sediments to entrain. We also compare the assessed sediment transport critical threshold with other four ID thresholds for debris flow triggering in dolomitic environment (Figure 3.1, lower panel). The considered threshold are those assessed by Genevois et al. (2000), Bacchini and Zannoni (2003), Berti and Simoni (2005), and Gregoretti and Dalla Fontana (2007). The lower panel of Figure 3.1 shows how the threshold estimated in this work is far apart from that of Bacchini and Zannoni (2003), while it is close to those of Genevois et al. (2000), Berti and Simoni (2005), and Gregoretti and Dalla Fontana (2007). In particular, it lies between those evaluated by Genevois et al. (2000) and by Berti and Simoni (2005). This occurs despite the different features considered for the

assessment of the thresholds. Genevois et al. (2000) focused their work on the Acquabona catchment and compared mean intensities of rainfalls corresponding to the triggering of debris flows with mean intensities of rainfalls that did not initiate any phenomena. The threshold was defined as the envelope of higher mean intensities with no occurrence of debris flow. Berti and Simoni (2005) carried out their analysis in the same catchment of Genevois et al. (2000), considering bursts exceeding an average of 0.5 mm in 5 minutes. Gregoretti and Dalla Fontana (2007) neglected the initial and ending samples of precipitation lower than 1 mm in 5 minutes because hydrological response did not change significantly. Their study concerned 6 different sites. Depending on the case, the reference rain gauge was located between 50 and 4000 m from the debris flow triggering area. On the other side, the threshold evaluated by Bacchini and Zannoni (2003) is the most dissimilar. This is mainly due to the adopted methods for selecting rainfall data used in their study. Bacchini and Zannoni (2003) analysed 21 rainstorms leading to channel-bed failures on 5 different basins. The rainfall dataset was recorded by rain gauges as far as 5000 m from sources areas. The durations of the events ranged between 30 minutes to 40 hours. In some cases precipitations were evaluated up to debris flow initiation, sometimes were the cumulative rainfall in the day of event occurrence. Furthermore, rain intensities were normalized by using the mean annual precipitation before obtaining the threshold.

A further analysis on rainfall is performed for investigating how the choice in the definition of burst affects the assessment of the threshold. Gregoretti and Dalla Fontana (2007) observed that the removal of the initial and ending segments from the hyetographs equal or smaller than 0.8 mm/5 min, i.e. with an intensity lower than 12 mm/hr, does not influence the results of the hydrological simulations of critical rainfalls. In this investigation, we analyse all the events recorded during the period 2011-2017 by the monitoring station, and those that did not trigger the alarm mode. Varying the minimum significant intensity for considering the inception of hyetographs, the mean intensity and the duration

of most the rainfalls obviously change. The higher the cutting threshold, the shorter the rainfall durations and larger the mean intensities. At the same time, the considered events decrease from about 1950 to 200. The decrease is mainly due to neglecting those did not cause runoff. In Figure 3.2, we illustrate the influence of trimming the initial and ending parts of the hyetographs on the evaluation of the events and the critical thresholds (we only consider the solid transport threshold for simplicity). As expected, ID thresholds tend to increase as we gradually raise the minimum intensity for cutting the rainfalls (blue dotted lines in Figure 3.2). A strange behaviour occurs when we increase the limit to 12 mm/hr (1 mm/5 min). The ID limit becomes lower than that evaluated excluding smaller intensities. The explanation lies on the event that occurred on July 13$^{\text{th}}$, 2017. It switches its duration from 4 hours to 2, while its mean intensity varies from 9.0 mm/hr to 12.5 mm/hr. The differences between the two mean intensities is lower than that evaluated by using the equation $I = 20.91D^{-0.59}$ (reported in Figure 3.2 (c)) for the two durations. For this reason, the small variation in mean intensity for the event of July 13$^{\text{th}}$, 2017, added to the drastic reduction in time, produces the decreasing of the critical threshold despite the raising of the hyetograph lower intensity. Indeed, neglecting that point, ID limit raises also for the limit of 12 mm/hr (red dotted line in Figure 3.2 (d)).

The same analysis is carried out on the testing sites of Acquabona Punta Nera and Rovina di Cancia. Figures 3.3 and 3.4 illustrate the recorded events on Summer 2016 in Acquabona Punta Nera, and on the Summers 2014-2016 in Rovina di Cancia. Mean intensities of rainfalls that triggered debris flows in the basin of Acquabona Punta Nera result sensibly lower than the Dimai ID thresholds in almost every case for each selected trimming intensity. This behaviour is due to a combination of several factors. The main factor is the huge availability of loose sediments in the catchment. During the spring of 2015 and 2016, two large rock collapses occurred on Punta Nera Peak cliffs, mainly due to frost weathering. These debris materials, mostly stopped on
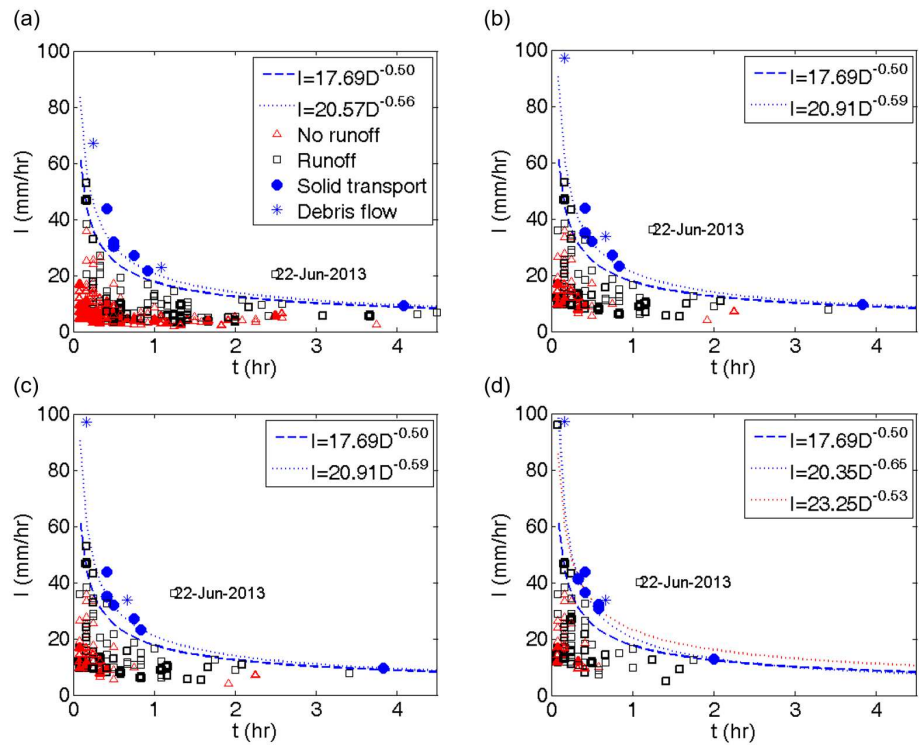
Figure 3.2: Analysis of the influence of initial and ending parts of the hyetographs on the evaluation of the critical thresholds. The minimum initial and conclusive intensities are: (a) 0.4 mm/5 min, (b) 0.6 mm/5 min, (c) 0.8 mm/5 min, (d) 1.0 mm/5 min. The thickness of indicators state the AMC of the event, from thinner (AMC I) to thicker (AMC III). AMC is computed considering for each event the cumulative rainfall of the previous two days (see also Section 3.3).

the channel incised on the rocky walls characterized by very high slopes, are easily entrainable by the surface runoff delivered by the cliffs. Lower discharges, i.e. lower rainfalls, need to move sediments lying on the channel. Moreover, the triggering mechanism could be debris mass deposit failure rather than for grain-by-grain bulking. It could require rainfalls of longer duration and lower intensity. Another aspect to not omit is the location of the reference rain gauge. Similarly to the Dimai watershed, it is close to the rocky channel outlet, but it is about 850 m far from the basin centroid. The high variability of convective events could make not completely truthful the rainfalls recorded by the monitoring station. The Rovina di Cancia example strengthens this last point of view. The monitoring station rain gauge RG6 is distant about 700 m from the watershed centre and does not overcome the threshold for one debris flow occurrence, while the rainfalls recorded by RG5, 100 m far from the centroid, exceed the ID limit in all the instances.

3.2   Observations about recorded discharges

The characteristics of the recorded discharges shown in Table 2.5 and the hydrographs of Figures 2.8 and 2.9 provide an overall response of the watershed to intense convective rainfalls. The delay in the response (evaluate as lag time t_L) is obtained using two methods. The first evaluates t_L as difference between the centroid of rainfall and the peak discharge (Sherman, 1932). The second calculates it as the time t_{LC} that returns the maximum value for the cross correlation coefficient of runoff and rainfall intensity time series (Kean et al., 2011, 2012). Values of lag time fall in the range 4-17 min, for the short high intensity precipitations; differently, for the events occurred on August 15th, 2011, on August 9th-24th, 2013, and on August 9th, 2016, characterized by the presence of very low intensity and/or extended rainfalls, lag times vary in the range 20-70 min. In general, lag times seem decreasing as rainfalls become more intense (e.g., August 19th 2013), attaining values close to those calculated by
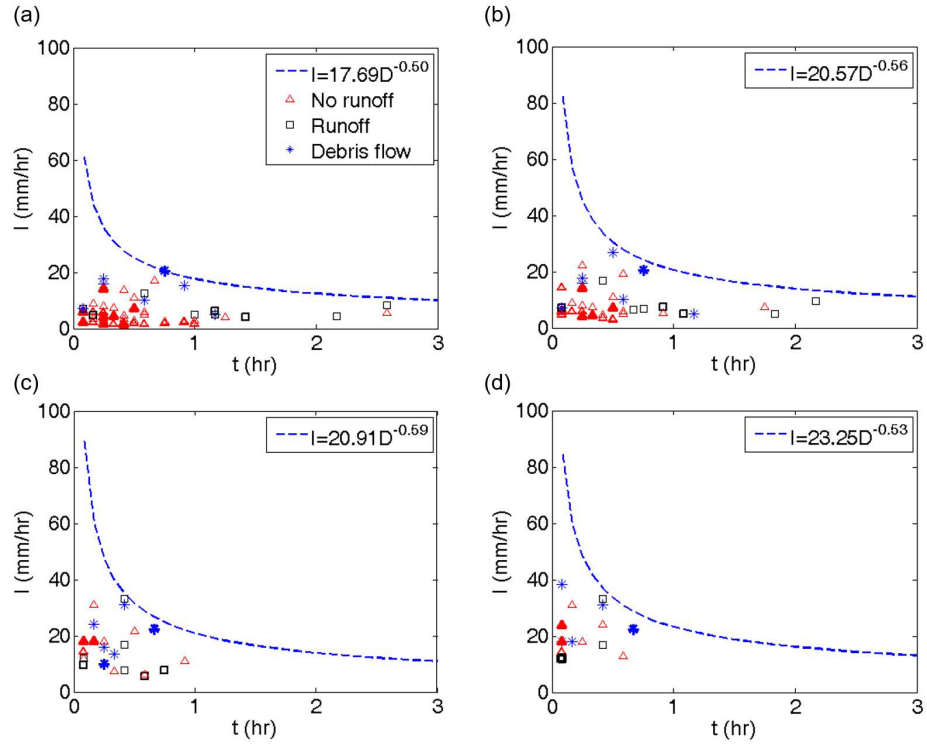
Figure 3.3: Analysis of the influence of initial and ending parts of the hyetographs on the evaluation of the burst features in Acquabona Punta Nera. The minimum initial and ending intensities are: (a) 0.2 mm/5 min, (b) 0.4 mm/5 min, (c) 0.8 mm/5 min, (d) 1.0 mm/5 min (we omit the graph concerning the threshold 0.6 mm/5 min because its results are very close to that obtained with the threshold 0.8 mm/5 min). The sketched thresholds correspond to those assessed for the Dimai watershed with the same hyetograph cutting intensity. The thickness of indicators state the AMC of the event, from thinner (AMC I) to thicker (AMC III). AMC is computed considering for each event the cumulative rainfall of the previous two days (see also Section 3.3).
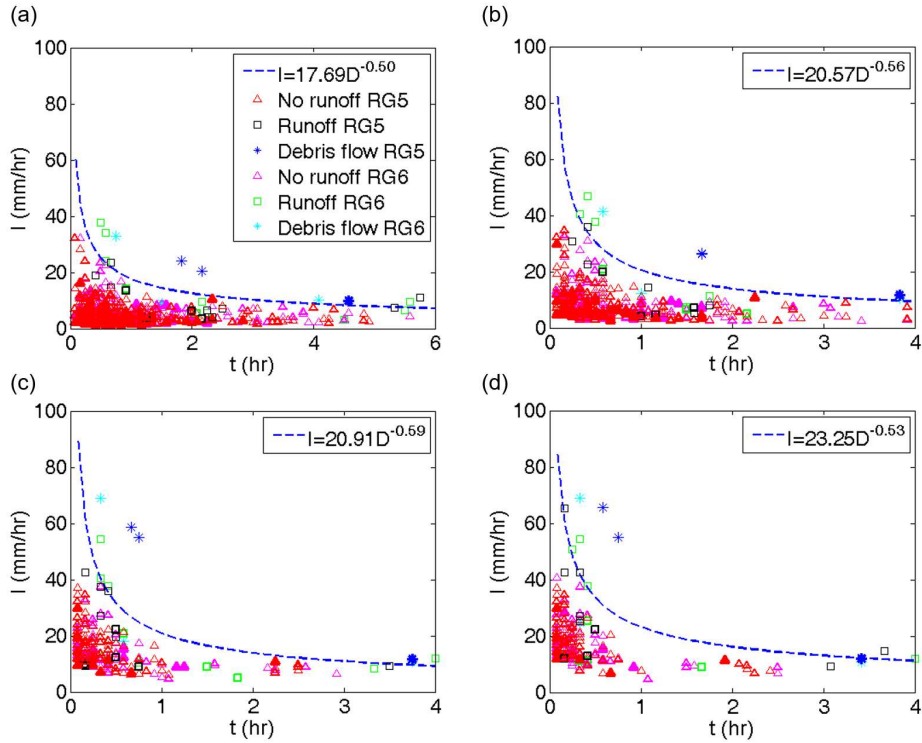
Figure 3.4: Analysis of the influence of initial and ending parts of the hyetographs on the evaluation of the burst features in Rovina di Cancia. The minimum initial and ending intensities are: (a) 0.2 mm/5 min, (b) 0.4 mm/5 min, (c) 0.8 mm/5 min, (d) 1.0 mm/5 min (we omit the graph concerning the threshold 0.6 mm/5 min because its results are very close to that obtained with the threshold 0.8 mm/5 min). The sketched thresholds correspond to those assessed for the Dimai watershed with the same hyetograph cutting intensity. The thickness of indicators state the AMC of the event, from thinner (AMC I) to thicker (AMC III). AMC is computed considering for each event the cumulative rainfall of the previous two days (see also Section 3.3).

Kean et al. (2012) for similar size basins. The time t_P in which runoff passes from zero to its peak value normally varies in the range 20-90 s. The higher the rainfall intensity peak, the fastest the basin response. For the events on August 24, 2013 and August 9, 2016 two peaks appear: the former is similar to those observed in the other events ($t_P \simeq 20$ s), the latter is less sharp and reaches an almost similar value. Summarizing, for convective rainfalls of short duration (about one hour or less), and estimated 5-minutes intensity larger than 15 mm/h, the time of response of the catchment is a few minutes. The flow discharge has an impulsive behaviour, with a rising limb (from zero to the peak value) lasting on average around one minute, and a subsequent decreasing to a smaller value. The lasting time of the smaller discharge value seems depending on the amount of rainfall that precipitates after the occurrence of the discharge peak.

The impulsive shape of discharges looks like the shape of debris flow hydrographs (Berti et al., 2000; Hürlimann et al., 2003; Kean et al., 2012), with a rising limb much faster than those observed in flow stage curves during flash flood in semiarid regions (Shannon et al., 2002) and in small mountain catchments (Kean et al., 2012). This kind of response emerges because of the interaction among high intensity bursts, steep slopes and in-channel routing. After considerable initial losses, due to the high degree of fissuring of rocky surfaces, high intensity rainfalls produce an excess rainfall through an Hortonian mechanism. The generated surface runoff reaches the rocky channel, causing a flood wave that progressively grows as it propagates downstream. Due to its high celerity, this wave incorporates smaller slower waves previously provided to the rocky channel by downstream slopes, leading to the highlighted rapid rising hydrograph shapes. The brief routing times is favoured by the steep slopes of the catchment, whereas the rapid decreasing of the hydrographs after the peak is caused by the limited duration of bursts that trigger the discharges.

Time-lapse videos show that slight discharges generally last for many hours after the conclusion of rainfall events. It means that the surface-subsurface flow

interaction plays a significant role in the investigated catchment. On the other hand, we are interested in modelling the sudden discharges that rapidly develop in response to high intensity bursts, i.e. surface runoff that could trigger debris flows. For this reason, the low conductivity of the rocky soils suggests that the saturation-excess runoff generation mechanism may not affect the hydrographs recorded by the monitoring station (Figures 2.8 and 2.9), and the assumption of neglecting the subsurface runoff should be reasonable.

3.3 Calibration of SCS-CN parameters

Before discussing the comparison between recorded and modelled hydrographs, it is essential to understand which values should be used in the Curve Number method for the involved parameters, i.e. CN, Ia, and AMC. The original value for the initial losses, $Ia = 0.2S$, was found too large by numerous authors (Hawkins et al., 2010; D'Asaro and Grillone, 2012). At the same time, as found out in the Section 3.1, a different way for evaluating AMC (respect to that reported in Table 1.4) could be taken into account. Due to the interaction between Ia and AMC through CN (see Section 2.3), we perform a sensitivity analysis on the recorded rainfall events for choosing the better combination to assign to the two parameters. We fix a constant value for the Curve Number $CN=90$, generally representative of rocky formations. We vary Ia between $0.05S$ and $0.2S$, with a step of $0.025S$, while cumulative rainfall, needed for the assessing of AMC, is computed considering 1 to 5 days before the events. Once evaluated both the parameters for any event, we consider the runoff prediction: could the fallen rainfall overcome the initial abstraction threshold and generate discharge?

Following Staley et al. (2013), we assess the performance for each Ia-AMC combination, considering the threat score (TS) (Schaefer, 1990) as:

$$TS = \frac{TP}{TP + FP + FN} \qquad (3.6)$$
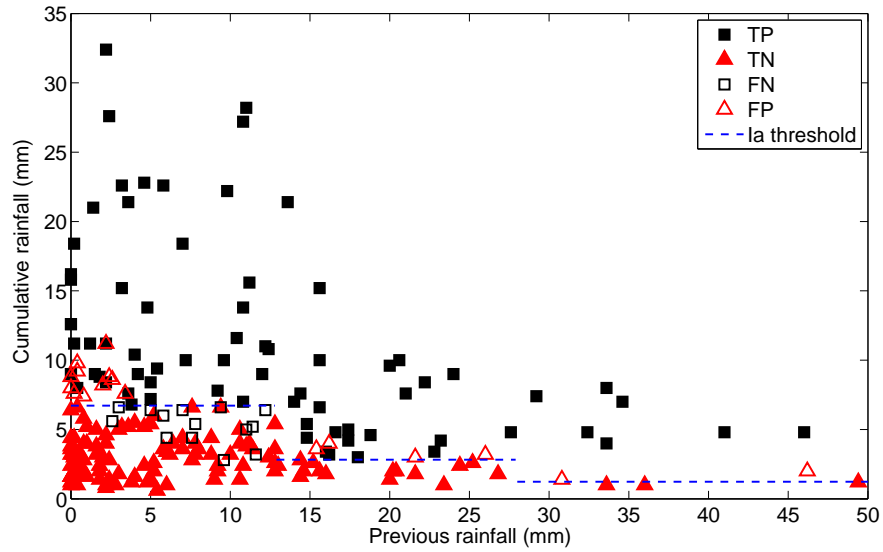
Figure 3.5: Runoff prediction analysis, varying the combination of Ia and AMC parameters. TP indicates the true positive events, TN the true negative ones, FN represents the false negative rainfalls, and FP the false positives. Ia threshold varies following AMC values (see equations 2.4 and 2.5). The limit values among the different AMC are reported in the first column of Table 1.4. The reported case refers to the combination $Ia = 0.1S$ and AMC assessed by using the cumulative rainfall of the previous two days.

TP, FP, and FN have been defined in Section 3.1. As reported in Staley et al. (2017), we choose TS as an indicator "*because it equally weights the reduction in score for both FN and FP events, while not biasing the results based on the large number of TN records in the database*". As deductible from Table 3.1, the combination with the best score ($TS = 72\%$) occurs with the values $Ia = 0.1S$ and AMC computed by using the cumulative rainfall fallen during the 2 days before each event (Figure 3.5). It confirms both the goodness of the assumption about $Ia = 0.1S$ made by Gregoretti and Dalla Fontana (2008) and the findings of Section 3.1, in considering 2 days of previous rainfall for selecting the AMC parameter. An interesting observation regards the number of rainfall events in the various moisture conditions. Changing the way to compute AMC (i.e. considering only the previous two days), the number of rainfalls in dry conditions increases of about 70% (from 96 to 165), while the variations of events in normal

or wet conditions are negative and in the amount of 35% (from 63 to 41) and 79% (from 60 to 13) respectively.

Table 3.1: Threat score, TS, computed by using equation 3.6 for each combination of the parameter Ia and AMC.

Considered days for AMC assessment	Ia						
	$0.050S$	$0.075S$	$0.100S$	$0.125S$	$0.150S$	$0.175S$	$0.200S$
1 day	59%	66%	65%	60%	48%	39%	35%
2 days	55%	67%	72%	67%	59%	48%	43%
3 days	54%	62%	66%	65%	61%	51%	49%
4 days	53%	58%	61%	63%	62%	56%	54%
5 days	51%	54%	57%	58%	60%	55%	55%

Starting from the estimated parameters, the calibration of the values of CN (Table 3.2) is obtained by matching measured and simulated runoff volumes for the significant events reported in Table 2.5. The resulting range of CN is wide (74.0-95.6) and appears to be dependent on the antecedent moisture conditions: higher the degree of saturation of soil, lower the value of CN. Absolute values of the curve number, CN_A, i.e. referred to the AMC conditions of each event, are obtained by means of equation 2.5. The interval of CN_A ranges between 67.7 and 90.1 and is representative of highly fissured rocky terrains, dominant presence in this basin (95% of the basin area). Excluding the values 67.7 and 71.5, corresponding to two very-prolonged rainfalls (longer than 3 hours and half) occurred on August 2013 and on 2016, the maximum relative difference is about 10 %, with a mean of 81.5. Considering also these lowest values, the mean of CN_A slightly decreases to 79.2, with a maximum relative difference less than 15%. Nevertheless, these values are comparable to those found by Hawkins et al. (2010) and D'Asaro and Grillone (2012), corresponding to a "violent behaviour" of the catchment. This response pattern is characterized by a sudden growth of CN when rainfall overcomes a determined threshold, up to reach an higher quite-stable value CN_∞.

Event	AMC	CN	AMC_{NEW}	CN_{NEW}	CN_A	Q_P	Q_{P1}	Q_{P2}	Q_{P3}	Q_{CNH}	Q_{CNH-MC}	f_C	C	II_s	Cu
						(l/s)	(l/s)	(l/s)	(l/s)	(l/s)	(l/s)	(cm/h)			
8/15/2011	I	81.3	I	81.3	64.6	0.2	0.1	0.1	0.1	0.1	0.1	0.54	0.0001	8.7/4.3	1.44
08-09-13	II	90.6	I	95.6	90.6	10.2	6.6	8.2	9.9	9.7	9.6	1.28	0.0435	8.3/3.7	1.97
8/19/2013	I	90.4	I	90.4	79.8	22.4	5.7	8.0	8.2	22.3	22.8	2.59	0.0123	13.7/3.7	1.97
8/24/2013	I	83.3	I	83.3	67.7	15.8	13.1	13.5	13.8	16.2	15.9	1.76	0.0535	13.7/13.2	1.70
08-12-14	I	88.4	I	88.4	76.2	15.7	4.3	5.2	8.4	15.9	15.7	3.46	0.0116	4.6/4.6	1.72
8/31/2014	I	90.1	I	90.1	79.3	12.9	5.8	6.0	6.3	13.1	13.4	1.15	0.0274	10.9/5.1	0.96
08-04-15	III	62.5	I	90.4	79.8	28.6	31.3	32.9	36.1	32.1	31.9	4.46	0.0660	11.7/9.8	2.00
09-03-15	I	92.8	I	92.8	84.4	34.4	41.8	42.6	46.5	42.0	41.1	2.63	0.1034	8.3/6.6	1.51
7/13/2016	III	74.0	III	74.0	86.7	28.5	30.0	41.9	53.6	33.0	28.1	5.00	0.0819	7.3/5.4	1.36
08-05-16	II	76.0	I	88.5	76.0	20.6	21.9	23.0	24.7	22.7	22.5	3.38	0.0853	7.1/6.7	1.93
08-09-16	III	50.3	I	85.7	71.6	38.8	46.3 (39.5)	49.7 (39.9)	51.5 (40.6)	49.0 (39.8)	48.5 (39.7)	2.34	0.1762	9.6/8.6	1.56
6/21/2017	II	83.9	II	83.9	83.9	13.3	13.6	19.7	26.9	21.1	14.1	4.68	0.0245	11.7/4.7	1.13

Table 3.2: Relevant features of simulated runoff discharges. AMC: antecedent moisture conditions, according to Soil Conservation Service (1972); CN: values of curve number for the rocky portion of the basin, related to AMC; AMC_{NEW}: antecedent moisture conditions, according to the new assessment method; CN_{NEW}: absolute values of curve number for the rocky portion of the basin, related to AMC_{NEW}; CN_A: CN_{NEW} normalized by using equation 2.5; Q_P: measured peak discharge; Q_{Pi}: peak discharge computed by setting the slope velocity U_S and the channel velocity U_C equal to 1) 0.3, 2 m/s; 2) 1, 1 m/s; 3) 3, 2 m/s); Q_{CNH}: peak discharge computed according to the SCS-CNH procedure; Q_{CNH-MC}: peak discharge computed according to the SCS-CNH procedure and kinematic wave routing with matched diffusivity; f_C: infiltration rate; C: runoff coefficient; II_s: performance parameter according to the new procedure SCS-CNH with constant U_C, the second one to the new procedure SCS-CNH with kinematic-wave routing); Cu: maximum value of the Courant number reached during the CNH-MC simulation.

3.4 Results of hydrological simulations

The model performance analysis begins with the simpler model (Gregoretti and Dalla Fontana, 2008), that computes the excess rainfall by the SCS-CN method and routes it to the basin outlet according to constant flow velocities (different values along slopes U_S and channel U_C). We use as example the event recorded on 19 August 2013 (Figure 3.6). We consider it a well-suited rainfall for the test of event-based hydrological models. It was produced by a convective rainstorm (8.7 mm in 30 minutes) with completely dry conditions of the basin (0.4 mm of cumulative rainfall in the previous two and five days, AMC I). For matching the measured and simulated volumes, we set CN=90.4 for the rocky surfaces of the catchment (Table 3.2), corresponding to an absolute value CN_A=79.8, and CN=61.0-75.0 (CN_A=39.6-55.8) for the remaining portions. Furthermore we assume $U_S = 0.7$ m/s for rocky cliffs, 0.1 m/s for scree slopes and $U_C = 1$ m/s, supposed constant along the entire rocky channel. This last statement was assumed congruent with the topographic features of the channel network, constituted by abrupt steps linked by highly sloped reaches, that prevented any fine calibration of the channel velocity at the outlet. The original version of the hydrological model is unable to reproduce the discharge, both on peak (about one third of measured) and timing t_P (delayed of about 4 minutes). Varying the couples of values adopted for U_C and U_S between 2 and 10 m/s, only the peak time prediction can be improved (Figure 3.6 shows the results achieved with $U_C = U_S = 3$ m/s, dashed line), while no significant progresses are obtained on the peak discharge. The only way to reproduce the maximum runoff is the modification of the total runoff volume, up to three times larger than that observed (dash-dotted line in Figure 3.6), after assuming $Ia = 0.1S$.

In general, the shapes of the simulated discharges are particularly different with respect to those recorded in the field. Even by coupling the SCS-CN method with the matched diffusivity kinematic model, the description of the
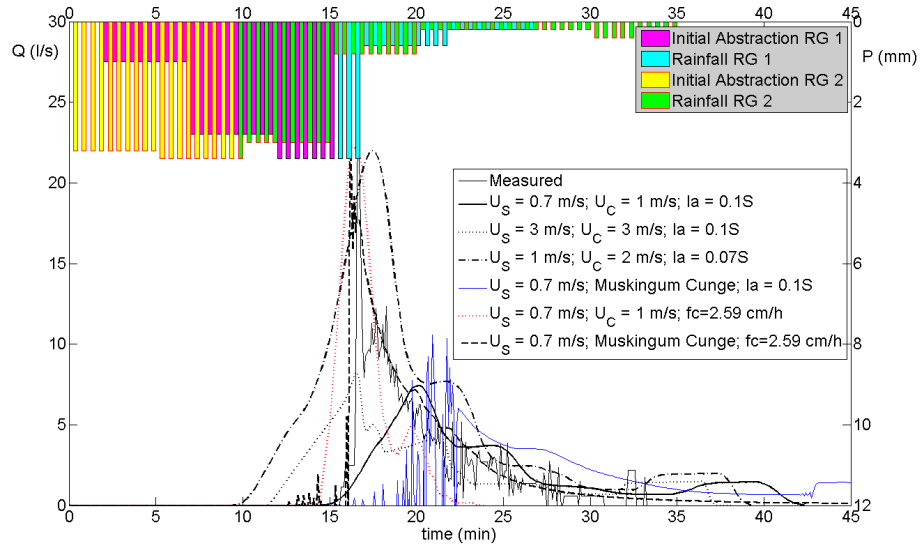
Figure 3.6: Simulations of the runoff hydrograph measured on 19 August 2013, carried out estimating the excess rainfall through the SCS-CN model and SCS-CNH procedure with both constant routing velocity approach and Muskingum-Cunge routing method (MC). Parameters are setted $k_s = 9$ m$^{1/3}$/s, $b_1 = 0.26$ and $\mathcal{B}_0 = 2$ m. Rainfall RG1 refer to the Dimai monitoring station, RG2 to the Pomagagnon Fork rain gauge. Rainfalls have been shifted in time to account for the areas of influence of the two rain gauges used to sample the rainfall. From Gregoretti et al. (2016b).

runoff hydrograph is not improved (Figure 3.6, dotted line). Discrepancies are due to an overestimation of initial infiltration of the rainfall. As a consequence, the model predicts a smaller peak discharge and a delayed peak time. Using either the initial model or the improved channel routing method, t_P is always too large and, consequently, the value of the peak flow is too small. Figure 3.7 helps to explain this behaviour. It shows the along-channel distribution of the extent of the hillslope areas that provide inflow to the channel network, highlighting in the inserts the discharges entering in the rocky channel about 250 m far from the basin closure section. The hydrographs evaluated by using the SCS-CN method and constant routing velocities U_S display a too slow rising limb of the curve, a low peak value and a duration greater than that observed. The use of a more accurate approach for the channel routing does not improve
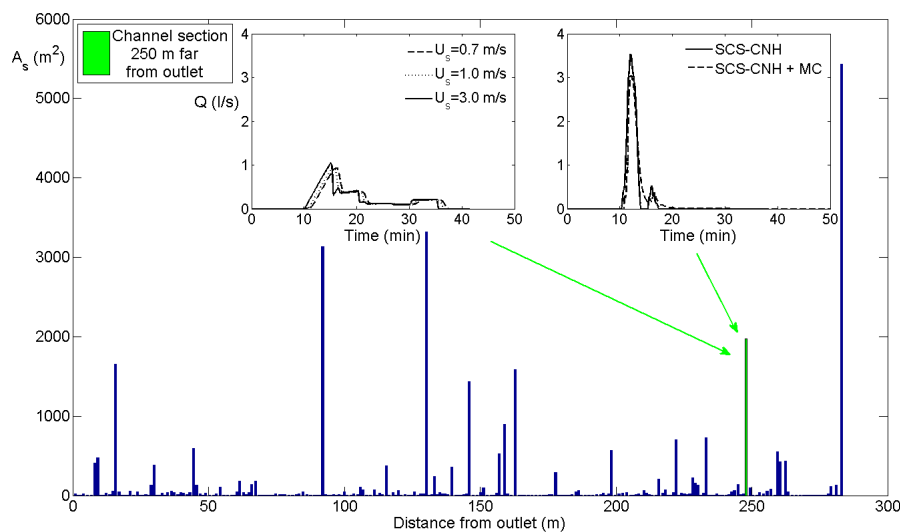
Figure 3.7: Along channel distribution the contributing areas A_S that supply runoff to the rocky channel. The inserts show two representative hydrographs corresponding to a channel section located 250 m far from the closure section, and achieved by means of: i) the SCS-CN method and various constant routing velocities U_S (left insert), ii) the SCS-CNH procedure and an hillslope routing velocity U_S=0.7 m/s (right insert), and iii) the SCS-CNH procedure coupled with the Muskingum-Cunge method ($k_S = 9m^{1/3}/s$) for simulating runoff propagation along hillslope surfaces (right insert). From Gregoretti et al. (2016b).

the shape of the modelled hydrograph, even resulting in a worse outcome.

A first step to improve the reproduction of the discharges is obtained through estimating the excess rainfall by means of the Horton simplified equation. Figure 3.8 exhibits the results of simulations carried out for the runoff events observed on 9, 19 and 24 August 2013, and 12-31 August 2014 and already presented by Gregoretti et al. (2016b). Peak runoff discharges are satisfactory approximated (the maximum difference is about $\sim 5\%$ for the event on 9 August 2013). Peaking times are almost well reproduced for all one but the events: differences varies in the range 0.5-2.5 minutes, excluding the 24 August 2013 event, for which only the second runoff peak is simulated, besides 4 minutes in advance. Figure 3.9 highlights the modelling for the events occurred between 2015 and 2017. Also in these circumstances, both peak discharges and peaking times are satisfactory reproduced. Differences in peak runoff vary between 2% and 18%.
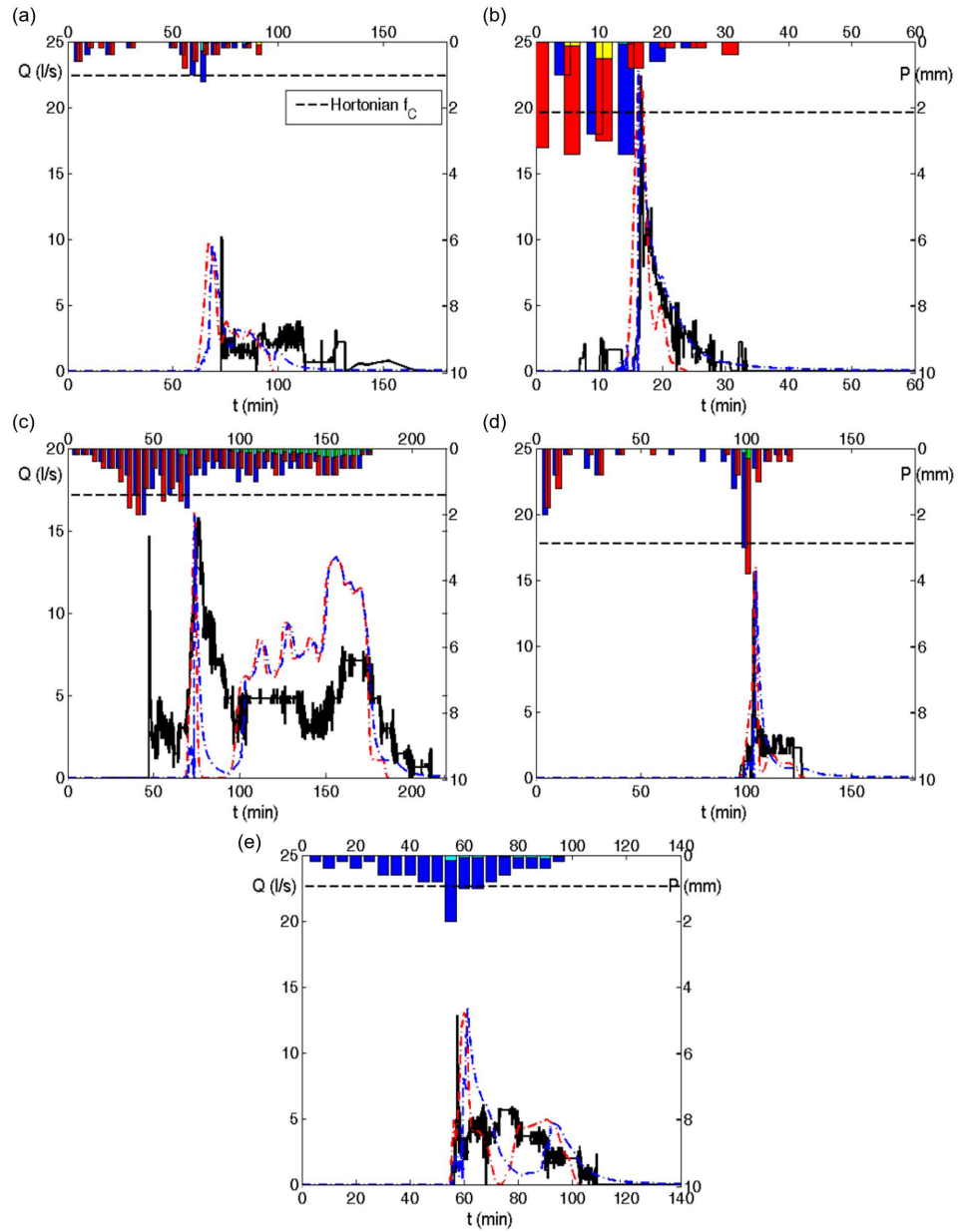
Figure 3.8: Comparison between observed runoff discharges (continuous line) and those simulated by using the SCS-CNH procedure with i) constant routing velocities (red lines) and ii) Muskingum-Cunge runoff routing along the channel (blue lines). Parameters $U_S = 0.7$ m/s, $b_1 = 0.26$, $\mathcal{B}_r = 2$ m, and $k_S = 9$ m$^{1/3}$/s are set. The observed events occurred on: 9 August 2013 (a), 19 August 2013 (b), 24 August 2013 (c), 12 August 2014 (d) and 31 August 2014 (e). Red and yellow corresponds to rainfall and excess rainfall concerning the Pomagagnon Fork rain gauge, while blue and cyan refers to the Dimai monitoring station. Rainfalls are shifted in time to the centre of the relevant influence areas (see Section 2.1.3) These results have already been presented by Gregoretti et al. (2016b).

The maximum error takes place on the second runoff peak of the event occurred on August 9th, 2016. Peaking times range in the interval 0.5-3 minutes, as occurred in the first 2 years of observations.

In all the computations, the only variable parameter is the infiltration rate f_C, while U_C (= 1.0 m/s) and U_S (= 0.7 m/s) are kept fixed. The infiltration rate, f_C, is varied considering the terrain moisture, i.e. on the basis of previous rainfalls (Beven, 2002). A sensitivity analysis on these three parameters is carried out to explain how the variation of each of them influences the output discharge and is shown in Figure 3.10. When U_S is increased, the peak discharge Q_P proportionally grows, while the peak time t_P reduces (left panel). Just the opposite is observable when f_C is increased (right panel). U_C only influences the timing of the hydrograph. A small variation of U_C, in the interval 1-1.2 m/s, entails a slight reduction of Q_P (5%) and an anticipation of about 1 minute in t_P. A further increase of U_C (up to 2 m/s) causes a time shift of some minutes in advance to the discharge. In summary, for the considered rainfall events, the SCS-CNH approach in combination with constant routing velocities appears to produce a robust estimate of the runoff discharge for $2 \leq f_C \leq 3$ cm/h, $0.5 \leq U_S \leq 0.9$ m/s and $1.0 \leq U_C \leq 1.2$ m/s. These runoff velocities are comparable with those estimated from the videos recorded by the monitoring station on 10 July 2010, 18 August 2011, and 19 August 2013. Also the variation range for f_C seems admissible, compatible with those measured by Li et al. (2011) in dolomite rocky outcrops. These values could be explained by the high fracturing degree of the Dolomite rock masses (Marchi et al., 2008). At the same time, the influence of the modelling approach cannot be excluded neither. However, an additional support to the goodness Hortonian approach is obtained plotting f_C values against the cumulative rainfall of the previous 2 days (Figure 3.11, left panel). All but two points tend to be arranged along a straight line. The events that do not follow the alignment are those occurred on August 13th 2016 and June 21st 2017. Differently to the other events, they occurred in AMC II and III (both for the old and the new approach, 2- or 5-days previous
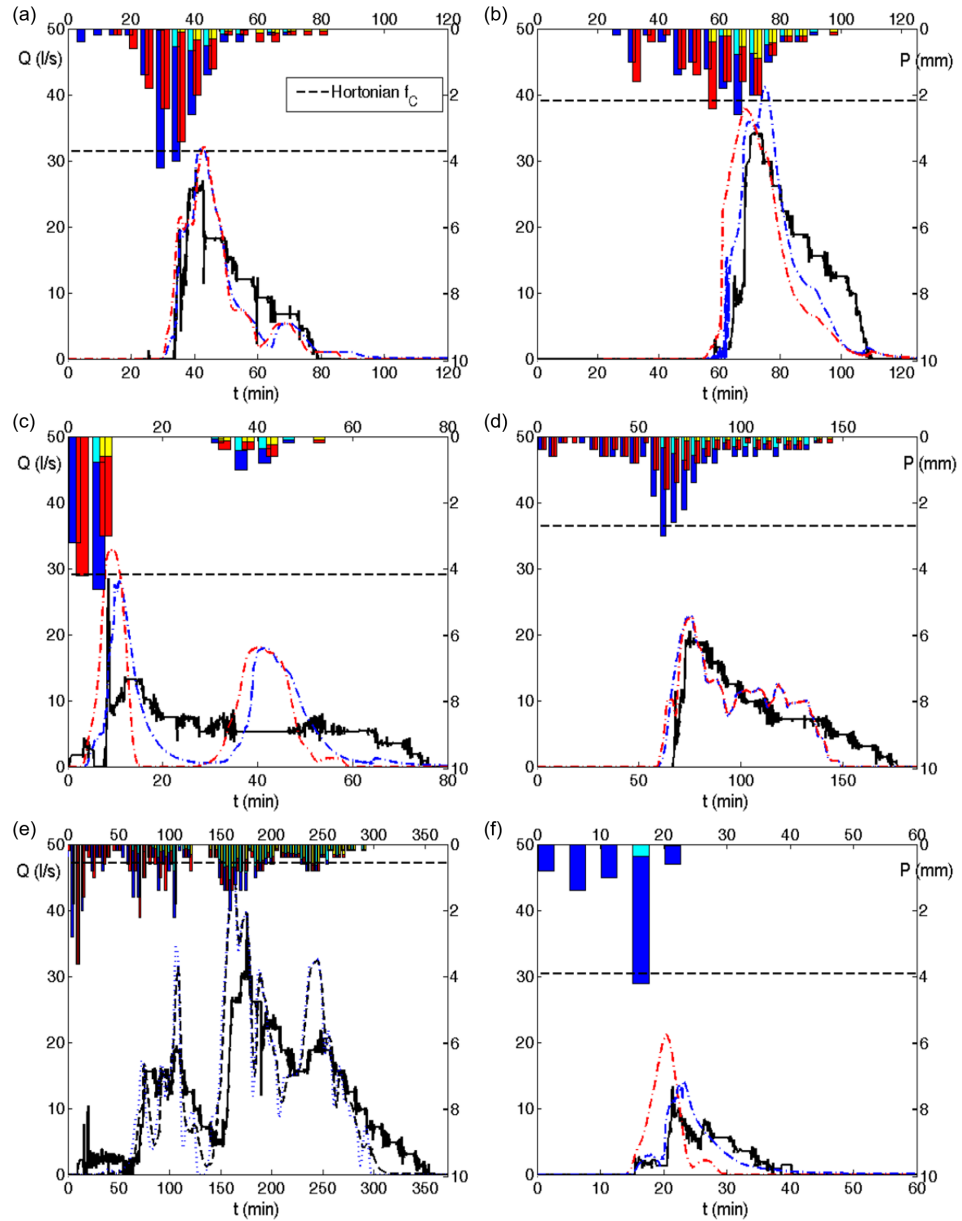
Figure 3.9: Comparison between observed runoff discharges (continuous line) and those simulated by using the SCS-CNH procedure with i) constant routing velocities (red lines) and ii) Muskingum-Cunge runoff routing along the channel (blue lines). Parameters $U_S = 0.7$ m/s, $b_1 = 0.26$, $\mathcal{B}_I = 2$ m, and $k_S = 9$ m$^{1/3}$/s are set. The observed events occurred on: 04 August 2015 (a), 03 September 2015 (b), 13 July 2016 (c), 05 August 2016 (d), 09 August 2016 (e), and 21 June 2017 (f). Red and yellow corresponds to rainfall and excess rainfall concerning the Pomagagnon Fork rain gauge, while blue and cyan refers to the Dimai monitoring station. Rainfalls are shifted in time to the centre of the relevant influence areas (see Section 2.1.3).

rainfall). A singular behaviour appears by observing that the linear trend for AMC I events is also complied by the maximum intensity of some events that did not generate any runoff (Figure 3.11, right panel). These events have been selected considering that their maximum rainfall intensity resulted higher than the infiltration rate f_C, evaluated by means of the linear interpolation equation traced in the left panel of the Figure 3.11.

The outcomes given by the SCS-CNH method with constant routing velocities show a certain degree of approximation. The time t_P is generally twice the real value, and the tails of simulations are shorter than those observed. A marked improvement is obtained when the runoff routing through the rocky channel is simulated by means of the matched diffusivity kinematic-wave model. Figure 3.6, referring to the event of 19 August 2013, shows the results of simulations carried out by setting $k_s = 9 \text{ m}^{1/3}/\text{s}$ (Gregoretti and Dalla Fontana, 2008), $b_1 = 0.26$ (Leopold and Maddock, 1953; Orlandini and Rosso, 1996), and $\mathcal{B}_0 = 2 \text{ m}$ (field measurements). The peak discharge, the vertical rising limb up to the peak, the subsequent rapid decrease, and the tail of the runoff hydrograph are all well reproduced. These findings apply in the same way to the various simulations of the events observed during the 5 years of monitoring (Figures 3.8 and 3.9).

In addition to the graphical comparison, the performance of the different methodologies are evaluated by means of the performance parameter Π_s (Schulz et al., 1999):

$$\Pi_S = 200 \frac{\sum_{i=1}^n |q_{c,i} - q_{o,i}| q_{o,i}}{n \, q_{oMax}^2} \tag{3.7}$$

where n is the number of observed discharges, $q_{c,i}$ and $q_{o,i}$ the corresponding values of computed and observed discharges, and q_{oMax} the maximum value of observed discharge. This parameter is widely used for evaluating the goodness of hydrological models, and a good performance is ensured by values of Π_S in the range 3-10 (Foglia et al., 2009). For the SCS-CNH method, Π_S takes values between 4.6 and 13.7, with a mean of 9.3 and the performances of 4
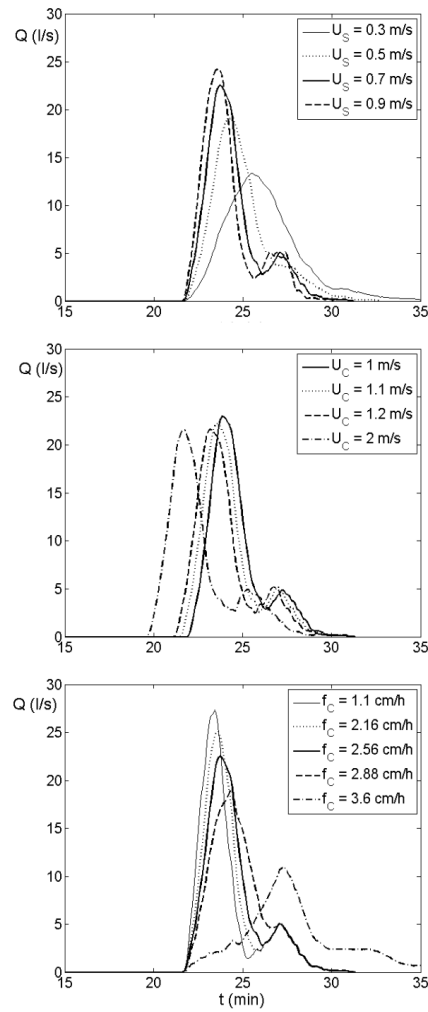
Figure 3.10: Sensitivity analysis about the parameters of the SCS-CNH model coupled with hillslope constant velocities: U_S (upper panel), U_C (central panel), and f_C (lower panel). The best simulation of the event occurred on August 19th, 2013 is denoted by a thick continuous line (carried out with $U_S = 0.7$ m/s, $U_C = 1$ m/s, $f_c = 2.59$ cm/hr). It correctly reproduces the peak value and the peak time of the observed runoff. Adapted from Gregoretti et al. (2016b).
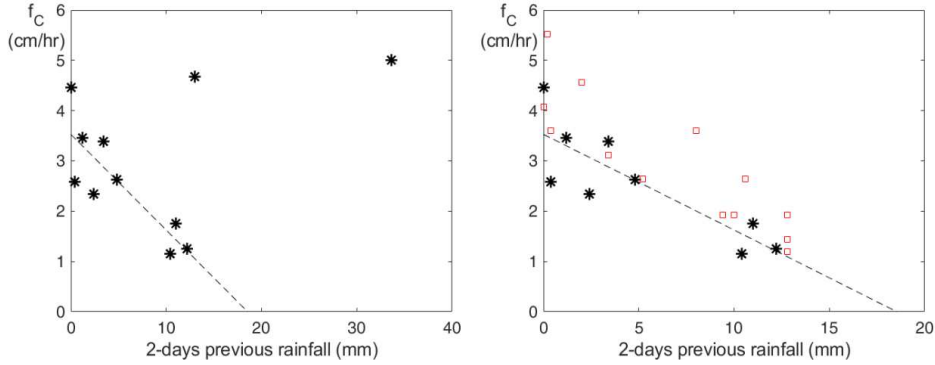
Figure 3.11: Hortonian infiltration rate f_C plotted against the previous 2 days cumulative rainfall. In the left panel, all the events are plotted. The intercept and angular coefficient, evaluated only considering the AMC I events, are 3.53 cm/hr and -0.19 cm/(mm hr). In the right panel, we plot the infiltration rates f_C of the AMC I events. The red squares represent the maximum rainfall intensity of some events with no runoff and maximum rainfall intensity higher than the infiltration rate f_C assessed with the previous equation.

events classified as sufficient, i.e. Π_S larger than 10 (Table 3.2). The better performance obtained by using the matched diffusivity kinematic-wave model are confirmed by the parameter Π_s; calculated values are smaller than those resulting from the SCS-CNH method with the constant velocity approach, with a mean of 6.6, and, all but one, lower than 10. Furthermore, it is noteworthy that the values attained by the weighting factor X (equation 2.18) are close to 0.5 except at the initial time steps. This implies that the diffusive term in the governing flow equation 2.9 is almost negligible.

In order to accomplish the sensitivity analysis in its entirety, we evaluate how would change computing excess rainfall by using the runoff coefficients, reported in Table 3.2, and the Hortonian components alone. For this second instance, we consider two sub-cases: the values f_C, already used for the simulations and reported in Table 3.2, and the values f_{CV}, that ensures the matching between measured and simulated runoff volumes. The comparison are displayed in Figures 3.12 and 3.13. In the runoff coefficient case, the modelled hydrographs generally replicate the evolution of the precipitation. When rainfalls are charac-
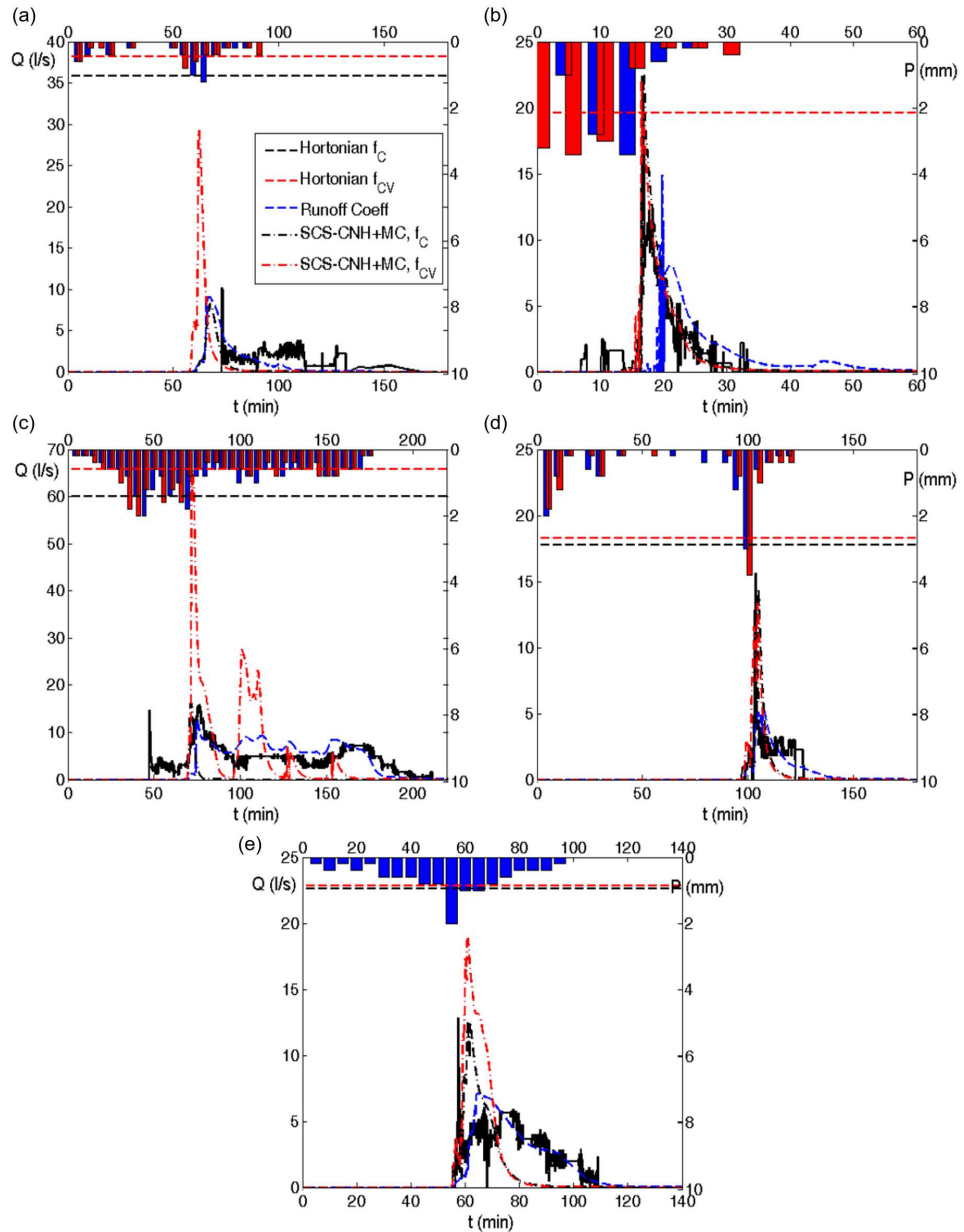
Figure 3.12: Comparison between observed discharges (continuous line) and those simulated by computing the excess rainfall with i) runoff coefficient (dashed blue lines), ii) the Hortonian component f_C alone (dash-dotted black lines), and iii) the Hortonian component f_{CV} that guarantees the matching between observed and simulated runoff (dash-dotted red lines). Parameters $U_S = 0.7$ m/s, $b_1 = 0.26$, $\mathcal{B}_l = 2$ m, and $k_S = 9$ m$^{1/3}$/s are set. The observed events occurred on: 9 August 2013 (a), 19 August 2013 (b), 24 August 2013 (c), 12 August 2014 (d) and 31 August 2014 (e). Red bars correspond to the rainfall recorded by Pomagagnon Fork rain gauge while blue bars correspond to the rainfall recorded by Dimai monitoring station.

terized by large pulses, the resulting hydrographs overestimate those recorded; otherwise the model output results in smaller peaks and longer durations than those measured by the monitoring station. In the second case, using the values f_C, a good replication of the observed hydrographs is obtained when rainfalls are characterized by large pulses including most of cumulative precipitation, for example 19th August 2013, 12th August 2014, 13th July 2016, or 21st June 2017. For the other events, both peak discharges and runoff volumes are underestimated. For reaching the equality between discharge volumes, we need to reduce the values f_C to the lower values f_{CV}. The consequence are the highly overestimated peaks that simulated discharges exhibit.

The latter tested approach considers the routing of runoff along the hillslope paths by means of the matched diffusivity kinematic-wave equation. Results are similar to those obtained with the constant velocity method (right insert of Figure 3.7), but the computational time required for the model execution is larger of about one order of magnitude. The outcomes of either a constant velocity or the matched diffusivity kinematic-wave equation model are essentially dominated by the extent of contributing areas. The along-channel summing of the various lateral inflows largely increments the in-channel discharge and, consequently, the wave celerity (see equation 2.21). As explained before, the flood wave of this runoff contribution can thus reach and include previous smaller waves, already routing along the channel. On the other side, surface runoff routing along hillslopes cannot increase as fast as in the channel. The discharge values are lower, whereas the gradients of the hillslope paths are higher than those along the channel (Figure 3.14). Therefore, the wave celerity (equation 2.21) varies in a small range and so the possibility of subsequent waves to merge together is limited. For this reason, runoff routing in sloping areas can be approximated through a constant velocity approach. This behaviour is in a partial contradiction with the viewpoint of Wooding (1965) and Robinson et al. (1995). They suggested that, for small size mountain watersheds, the hydrological dominating behaviour is the hillslope response rather than the channel one,
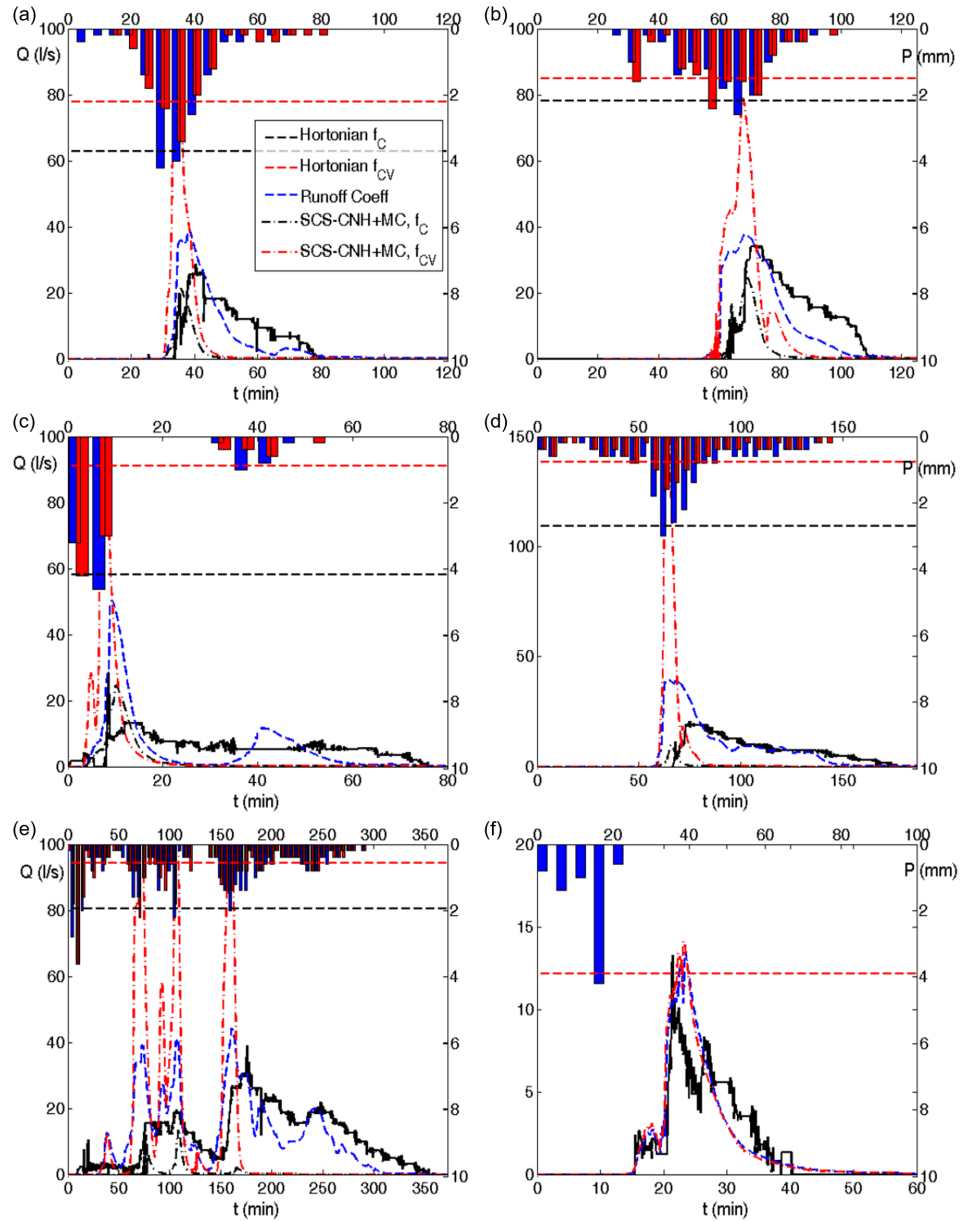
Figure 3.13: Comparison between observed discharges (continuous line) and those simulated by computing the excess rainfall with i) runoff coefficient (dashed blue lines), ii) the Hortonian component f_C alone (dash-dotted black lines), and iii) the Hortonian component f_{CV} that guarantees the matching between observed and simulated runoff (dash-dotted red lines). Parameters $U_S = 0.7$ m/s, $b_1 = 0.26$, $\mathcal{B}_l = 2$ m, and $k_S = 9$ m$^{1/3}$/s are set. The observed events occurred on: 04 August 2015 (a), 03 September 2015 (b), 13 July 2016 (c), 05 August 2016 (d), 09 August 2016 (e), and 21 June 2017 (f). Red bars correspond to the rainfall recorded by Pomagagnon Fork rain gauge while blue bars correspond to the rainfall recorded by Dimai monitoring station.
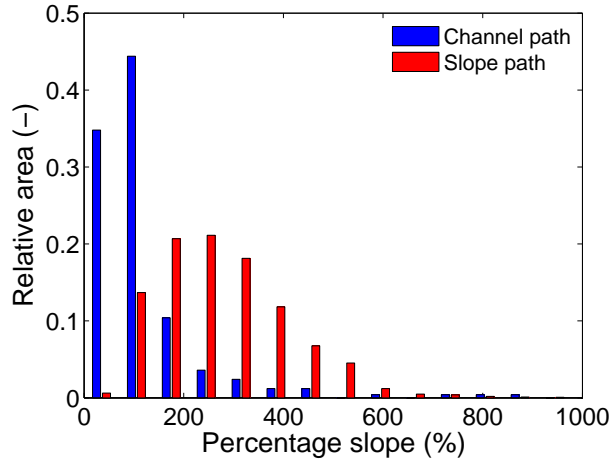
Figure 3.14: Comparison between percentage slopes in channel network and in slope paths. The larger values of mean slope in sloping areas permits to approximate the routing along hillslope paths through a constant velocity approach.

suggesting to place focus on the hydrodynamic routing of discharges through hillslopes, differently to our findings. As a consequence, the non-linear storage model developed by Horton (1938) cannot reproduce the distribution of measured discharges, neither by means of the modified form proposed by Agnese et al. (2001).

The work of D'Asaro and Grillone (2012) suggested us to test also the possibility that the sudden rising of observed runoff events could be due to a basin partial contributing to the delivering of discharges. To support or reject this assumption, we carried out some additional modelling, excluding the upper part of the basin from the contributing area. This portion of catchment (25% of the basin area) is characterized by restricted slopes and corresponds to the influence area of the Pomagagnon rain gauge. The simulated hydrographs does not describe discharges better than what already achieved (shown in Figures 3.6, 3.8 and 3.9), but are obtained with values of parameters ($U_S = 2$ m/s and $\mathcal{B}_0$ $= 0.25$ m) that seem physically less significant. As a consequence, it is possible to affirm that all the basin is likely contributing to runoff.

The outcomes illustrated in this Section suggest some general statements:

- Routing the excess rainfall, assessed by using the SCS-CN method, with a constant velocity approach does not lead to reliable results in rocky headwater catchments. For each hillslope contributing area yielding surface runoff to the channel, this procedure produces too-slow growing discharge hydrographs, less peaked and too much elongated in time (left insert of Figure 3.7). For this reason, their total contribution is unable to replicate the observed impulsive shape of the recorded hydrographs. Neither the improving of channel routing by means of the matched diffusivity kinematic-wave equation leads to better results, as illustrated in Figure 3.6.

- When the direct runoff is estimated through the SCS-CNH method, and the along channel routing is carried out taking a constant velocity, the hydrograph peak can be detected but without its typical impulsive shape.

- To reproduce both the peak and shape of the observed hydrographs, a kinematic model with matched diffusivity is needed.

- The constant velocity approach and the matched diffusivity kinematic-wave model applied to the routing along slope paths seem giving comparable results, because slope paths are characterized by very high gradients (see right insert of Figure 3.7).

3.5 Considerations on the adopted modelling parameters

In the previous Sections, we report no details about the structural parameters used in the surface runoff propagation modelling. The propagation has been performed by using the finest available LiDAR DEM, with a spatial resolution Δx of 1 meter. As reported in the Section 2.1, the use of an accurate topographic dataset is fundamental for a reliable hydrological modelling (Quinn et al., 1991; Garbrecht et al., 2001; Degetto et al., 2015). For this reason, we

chose to set the simulation time step Δt in order that the computational con-
strains due to the numerical method would have been met. As reported in
Orlandini and Rosso (1996), no general conditions for accuracy are a priori es-
tablished for the Muskingum-Cunge method. In general, it is recommended to
satisfy the empirical criterion $C_1 \geq 0$. Cunge (1969) found that, in the linear
analysis, the numerical dispersion could result minimised if the Courant number
Cu is maintained close to 1. In the nonlinear case, instead, Cu can vary cell-by-
cell, and it is not possible verify if accuracy is kept. Orlandini and Rosso (1996)
suggested a threshold value $Cu^* = 3$ to avoid fluctuations in the modelling.
The definition of the Courant number is $Cu = c_k \frac{\Delta t}{\Delta x}$, with c_k resulting from
equation 2.21.

As a first test, we maintained the time step Δt set by KRERM (Gregoretti
and Dalla Fontana, 2008):

$$\Delta t = \frac{\Delta x}{max(U_S)} \tag{3.8}$$

with the maximum slope velocity $max(U_S) = 0.7$ m/s, and $\Delta t = 1.43$ s. In
Table 3.2, we report the maximum values of Cu reached along the entire channel
during the modelling of the events. The maximum value results $Cu = 2.00$,
reached during the simulation of the event occurred on August 4th, 2015. On
account of this result, we kept the assumed Δt. In Section 3.6, we will present
further simulations performed on the two catchments described in Section 2.4
that are wider than the Dimai watershed. For these basins, we found that the
resulting Cu were too big (maximum $Cu = 5.8$) if we maintained $\Delta t = 1.43$ s.
Considering to be truthful the threshold $Cu^* = 3.0$, we set $\Delta t_{new} = 0.5dt$. In
this way, the maximum Cu resulted 2.8.

3.6 Robustness of the model

In order to verify the predictability of the improved hydrological model,
coupling the SCS-CNH method with a constant velocity routing along slopes

Basin	Date	Recorded phenomenon	Rain gauge	Rainfall depth (mm)	Rainfall duration (min)	AMC	Time (GMT)	t_P (GMT)
Acquabona Punta Nera	7/21/2016	solid-liquid front transit	RG3	13.6	30	AMCI	18:33	18:36
Acquabona Punta Nera	8/14/2016	solid-liquid front transit	RG4	18.6	40	AMCI	20:01	20:06
Rovina di Cancia	7/23/2015	solid-liquid front transit	RG5, RG6	36.4	40	AMCI	15:06	15:07
Rovina di Cancia	8/4/2015	runoff arrival	RG5, RG6	34.8	40	AMCI	19:37	19:38

Table 3.3: Type of recorded event, the rain gauge used for simulation, rainfall depth and duration, AMC condition, occurrence time of the event, and simulated runoff peak time t_P. For the location of the rain gauges, see Figure 2.10.

and a matched diffusivity kinematic-wave routing along the channel network, we apply it to two other dolomitic sites prone to runoff-generated debris flows, Acquabona Punta Nera and Rovina di Cancia. For the features of the two basins, the reader can refer to Section 2.4. According to Rengers et al. (2016), the comparison is carried out evaluating the difference in time between the peak of simulated discharges and runoff arrival/debris flow transit in the triggering area.

Table 3.3 reports the characteristics of the precipitation (rainfall depths, durations, and corresponding AMC) recorded by four rain gauges (Acquabona Punta Nera monitoring station, RG3; Faloria, RG4; Rovina di Cancia, RG5 and RG6, see Figure 2.10), as well as the timing of runoff arrival and/or debris flow occurrence. The considered rainfall events triggered debris flows on July 21st, and August 14th, 2016 in the basin of Acquabona Punta Nera, and on July 23rd, and August 4th, 2015 at Rovina di Cancia.

Following the findings reported in Section 3.3, the CN_A coefficient has been set equal to 81.5 for rocky surfaces, whereas the CN values for mountain pine slopes (CN=61), and for scree slopes (CN=65-70, depending on thickness and texture of deposits) have been taken from the literature. The slope velocity, U_S is assumed equal to 0.7 m/s for rocky path and 0.1 m/s for the remaining terrains. The coefficient f_c for rocky surfaces is obtained through the linear relationship shown in the left panel of Figure 3.11, whereas direct field observations
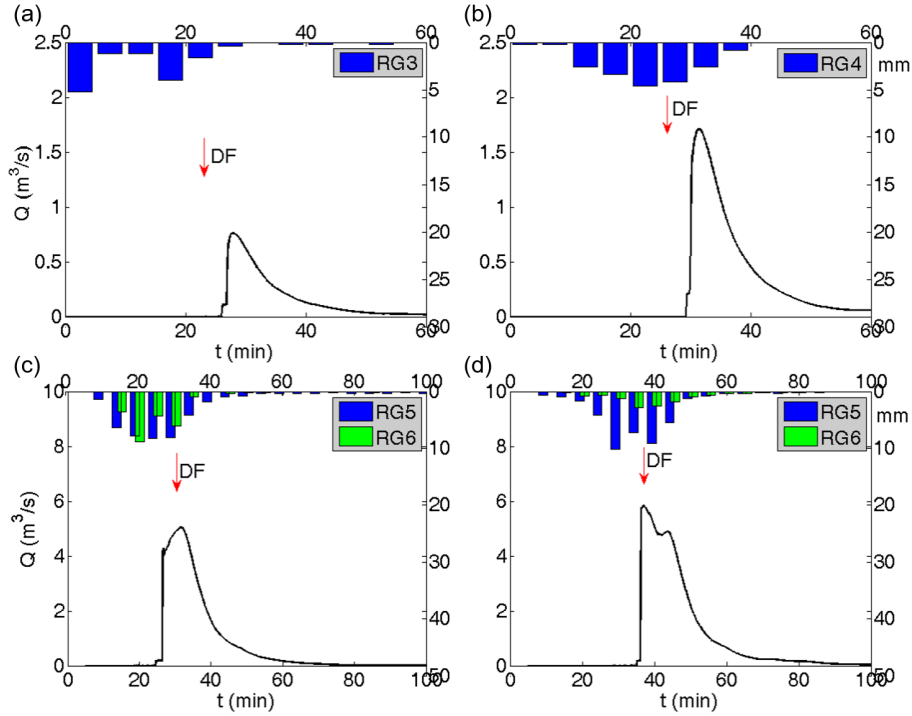
Figure 3.15:   Simulated   runoff   hydrographs,   with   the   timing   of   debris/hyperconcentrated flow pointed by an arrow, for the rainfall events recorded at: a) Acquabona Punta Nera, 21 July 2016; b) Acquabona Punta Nera, 14 August 2016; c) Rovina di Cancia, 23 July 2015; d) Rovina di Cancia, 4 August 2015. The values of the parameters adopted in the hydrological model are: $U_S = 0.7$ m/s and $k_S = 9$ m$^{1/3}$/s, $\mathcal{B}_I = = 6$ m for Acquabona Punta Nera and 6.7 m for Cancia. Rainfalls are shifted in time to the centre of the relevant influence areas.

have been carried out to estimate f_c on the scree. In particular, we performed some measures of infiltration rate by means of a double ring infiltrometer the day before the event of July 23$^{\text{rd}}$, 2015, that resulted in $f_c = 10.8$ cm/hr. This high value corresponds to AMC I conditions and is set for every event in both the watersheds. Furthermore, for the terrain with mountain pine we assumed $f_c = 5.5$ cm/hr, following Li et al. (2011). Finally, the outlet widths for Acquabona Punta Nera and Cancia basins are about $\mathcal{B}_0 = 6.0$ and 6.7 m, respectively.

Figure 3.15 shows the simulated discharges and the timing of debris flow initiation. Rainfalls recorded by the rain gauges were shifted to the centres of the basins, as already done for the Dimai catchment. In Acquabona Punta Nera,

we observe that debris flows initiate just before the peak of simulated runoffs, while in Rovina di Cancia, debris flow (23 July 2015) and hyperconcentrated flow (4 August 2015) initiations are almost coincident with the simulated runoff peak (Table 3.3). The calculated hydrographs for the events that occurred in Rovina di Cancia are different from those already discussed and published by Gregoretti et al. (2016b). For the event of July 23rd the differences are slight, but for the hydrograph of August 4th differences are more evident. The discrepancies between these results and Gregoretti et al. (2016b) are due to three factors:

1. The previous days of cumulative rainfall to consider for evaluating AMC has been switched from five to two;

2. We have modified the linear relationship for assessing the infiltration rate f_C;

3. The CN$_A$ has been set equal to 81.5, instead of 79.8.

With these changes, the simulated hydrographs seem to agree with the recorded time-lapse videos of the two events better than those of Gregoretti et al. (2016b). Recorded videos show that flow levels were very similar for the two events, with the second event lasting only few minutes longer than the first.

A possible explanation for the delay between debris flow timings and simulated runoff peak times in Acquabona Punta Nera could be due to the difference in the triggering mechanism in the two basins. In Rovina di Cancia, as a result of field exploration of the channel upstream the triggering area, we can assume that the discharge is continuous, because there is no evidence for a dam break phenomenon caused by blockage of the channel. Instead, in Acquabona Punta Nera, due to the huge availability of loose sediments in the catchment, we cannot exclude debris flow initiation from mass failure of in-channel sediment deposits, similar to that pointed out by McGuire et al. (2017). Consequently, debris flow initiation could be plausibly earlier than the peak of the runoff discharge. Furthermore, the largest time lag between debris flow occurrence and runoff peak (5 minutes) corresponds to a rainfall recorded by RG4, about 1.8 km far from the centre of Acquabona Punta Nera basin. For this reason, the precipitation

could not correctly represent the effective rainfall fallen over the basin.

The obtained outcomes are consistent with the inception mechanisms of debris flows. Indeed, in both the cases, debris flow triggering is strictly related to the destabilizing action exerted by runoff on in-channel sediment layers. Hence, a small time lag between the hydrograph peak simulation and the triggering instant of debris flow implies a rather robust performance of the rainfall-runoff model. These findings are completely in agreement with those of Rengers et al. (2016), who compared the peak times of modelled discharges with those of corresponding stage hydrographs of occurred debris flows, concluding that hydrological models can emulate the initiation time of runoff-generated debris flows. This similar behaviour took place although the difference in the implemented excess rainfall generating process, due to the distinct features of the analysed catchments. Rengers et al. (2016) evaluated excess rainfall by means of the Green-Ampt approach, i.e. a saturation-excess runoff production mechanism, whereas we used an infiltration-excess method, as the Horton equation.

The capability of the developed model to catch the runoff peak time with good accuracy suggests a potential use in early warning systems for evaluating the debris flow occurrence time. A further application could also be to estimate the building-up of the solid-liquid hydrograph required to execute debris flow propagation models. For example, the water discharge runoff contributing to the debris flow formation and the corresponding solid-liquid hydrograph could be determined and propagated by using the procedure developed by Gregoretti et al. (2012) and resumed by Gregoretti et al. (2016a) and De Paola et al. (2017). A reliable estimate of entrainable sediment volume and, consequently, of the potentially inundated areas is fundamental to hazard assessment and risk evaluation, the design of appropriate structural countermeasures, and the development of efficient emergency management regulation.

3.7   Weaknesses of the model

As highlighted in Section 3.4, the proposed hydrological model reproduces with good accuracy all the features of the recorded hydrographs, such as the peak value and timing of discharges and the overall volume. Furthermore, in Section 3.6, we showed the accuracy in predicting the occurrence times of runoff-generated debris flows. Nevertheless, some general remarks on the weak spots of the model need to be pointed out:

1. Despite the truth of setting $Ia = 0.1S$, a better characterization of the initial losses would be useful. In some cases, such as events occurred on August 24th, 2013 or August 9th, 2016, the model is unable to catch the first peak of the runoff discharge;

2. The implemented Hortonian approach is congruent with the infiltration-excess mechanism typical of the high-slopes dolomitic catchments in response to high intensity rainstorm. On the other hand, when rainfall intensity drops under the prescribed infiltration rate, the computation of excess rainfall by means of the SCS-CN method is rough and, probably, not representative of the different runoff generation process. Furthermore, the mechanisms of storing and restitution of infiltrated rainfall is still poorly understood. For example, longer duration events, such as those occurred on August 24th, 2013 or August 9th, 2016, exhibit a worse behaviour when simulated;

3. In Figure 3.11 we displayed a robust linear relationship between infiltration rates and 2-days of cumulative previous rainfalls for AMC I events. This relation is still missing for the events that occurred in normal (AMC II) or wet (AMC III) moisture conditions, which, on the other hand, are very few.

3.8 Future developments

In Section 1.3, we mentioned the rainfall forcing to the catchments among the major sources of uncertainty. We highlighted that the use of both the rain gauge and the weather radar measurements has strengths and weaknesses. In our analysis, we focused our attention on the measures recorded by rain gauges. Their placement close to the rocky walls of the Dimai and Rovina di Cancia headwater basins permitted to estimate with good accuracy the precipitations hitting the catchments. At the same time, in Section 3.1, we showed that the debris flow triggering rainfalls gauged in the initiation zone of Acquabona Punta Nera debris flow channel resulted lower of the triggering critical thresholds estimated by using the Dimai monitoring station records. Among the various causes of this behaviour, the distance between the rain gauge position and the basin centroid is the most influential when we consider the tremendous variability of convective storms in Alpine areas. Orlandini and Morlini (2000) also recognized and investigated this problem in the same geographical area, proposing the use of the weather radar to improve the description of convective precipitations. The use of weather radars could be very useful to take into account the spatio-temporal variability of debris flow triggering rainfalls, increasing their benefit as the basin size increases and the rain gauge placement is not optimal. Some introductory analysis on radar rainfall fields have been already performed. Investigated rainfall fields were surveyed by means of the weather radar placed on the Mount Macaion (Bolzano province), about 70 km far from the study areas, and were obtained by using the Marshall-Palmer (MP) equation for transforming the recorded reflectivity into rainfall intensity. Preliminary results lead to a general underestimation of the precipitations in the area, due to the issues that appear by using weather radars in mountainous regions (Germann et al., 2006). Moreover, these findings confirm the results of Orlandini and Morlini (2000), that needed to employ some artificial neural networks for improving the rainfall fields obtained by using the MP relationship. In the next future, we will test
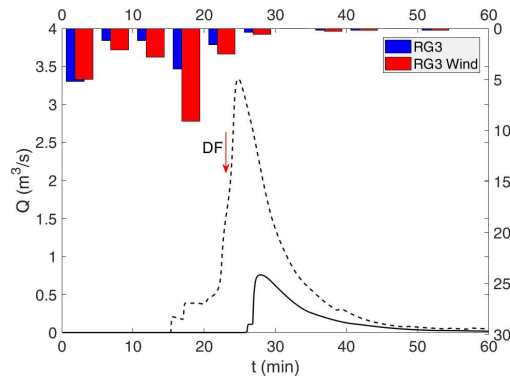
Figure 3.16: Simulated runoff hydrographs for the rainfall events recorded at Ac-quabona Punta Nera, 21 July 2016, with the timing of debris flow pointed by an arrow. The blue rainfall and the continuous-line hydrograph have been already displayed in Figure 3.15 (a). The dotted-line discharge represents the surface runoff modelled by using the rainfall corrected through the model described by Orlandini and Lamberti (2000) (red bars) for considering the influence of wind. Wind data were recorded by the monitoring station located in the Acquabona Punta Nera basin.

some correction methods to make available radar data suitable for our purposes.

Another aspect that could be examined in more depth is the influence of wind on the precipitation fallen on the steep slopes characterizing the Alpine environment. This problem was initially addressed by Orlandini and Lamberti (2000). They developed a simple model to describe the 3D rainfall field due to the effects of wind speed and direction on the precipitation. The model was later applied to the Fiames and Acquabona study cases, two catchments close to those analysed in this work. According to the observations recorded in the field by the monitoring stations, the presence of wind during convective events is significant and, consequently, its effects should not be neglected. Unfortu-nately, the monitoring station placed in the Dimai catchment is not equipped with an anemometer and, for this reason, the influence of wind on the precipi-tation interesting the basin is not easily probed. Furthermore, the monitoring stations placed in the contiguous watershed Fiames and on Pomagagnon Fork frequently recorded contrasting wind directions during the same event, produc-ing discrepancy when we apply the correction to the Dimai events. Conversely, the introductory analysis about wind effects on the Acquabona Punta Nera

watershed seems corroborate the 3D model of Orlandini and Lamberti (2000). Considering about ten events, we find an increasing in precipitation intercepted by steep slopes of about 50% on average, ranging from 20% to 150%. As a consequence, the increment in precipitations leads to the increase in the discharge peak values and to the reduction in the delay between debris flow timings and simulated runoff peak times (e.g. Figure 3.16 shows the event occurred on July 21st, 2016, already displayed on Figure 3.15 (a)). Moreover, these findings could be added to the why of the debris flow triggering rainfalls do not overtake critical thresholds.

Chapter 4

Conclusions

The abrupt morphology and the impervious nature of the headwater catchments in the Dolomites make monitoring activities challenging. A thorough knowledge of discharge behaviour is fundamental to improve knowledge about debris flow initiation and to model the dynamics during their triggering on scree slopes extending at the base of rocky cliffs. The measurement facility installed at the outlet of the Dimai headwater basin provided valuable data about the hydrological response of this type of mountain watersheds.

We documented the hydrological response of the catchment to twelve convective rainfall events. Observed hydrographs exhibit an impulsive character, with a well-defined initial peak, similar to that observed in the stage hydrographs of debris flows (Berti et al., 2000; Kean et al., 2012). The surface runoff then decreases quite rapidly, generally down to a nearly constant plateau. In this way, the runoff hydrograph can be schematized by two rectangles: the former high and narrow, the latter shorter and longer.

The analysis of rainfalls recorded during Summers 2011-2016 highlighted that the ID critical thresholds evaluated by Berti and Simoni (2005) and Gregoretti and Dalla Fontana (2007) are good indicators of debris flow initiation conditions. Furthermore it showed that the losses in the basin before generating runoff can be replicated by using the SCS-CN method, modified by adopting I_a

$= 0.1\,S$, as already assumed by Gregoretti and Dalla Fontana (2008), Hawkins et al. (2010) and D'Asaro and Grillone (2012), providing that AMC is assessed by using the cumulative rainfall of the previous two days. In this way, the SCS-CN method has been found to carefully compute the discharge volume, but not the magnitude of the peak discharge and the overall shape of the hydrograph. This inadequacy is mainly due to an incorrect estimation of the excess rainfall generation pattern: it is clear the overestimation of the initial infiltration and, hence, an underestimation of the excess rainfall contributing to the flow discharge.

For surpassing this drawback, the SCS-CN method has been coupled with a simplified Horton equation that simulates the runoff generation process for infiltration-excess, i.e. when the rainfall intensity is larger than a prescribed infiltration rate, and the cumulative excess rainfall lower than that computed accordingly to the SCS-CN procedure. The suggested methodology, denoted as SCS-CNH, produces encouraging results. The coefficients CN, calibrated to ensure the matching between observed and simulated runoff volumes, vary inside a small interval of values, around an absolute value of 81.5. The value and the timing of the peak discharge, and the total runoff volume are replicated with a satisfactory precision.

A further improvement in replicating the overall shape of the recorded runoff hydrographs can be obtained by means of a matched diffusivity kinematic model, suggested for the runoff routing along the channel. The almost vertical raise of the runoff discharge, and the decreasing limb are modelled with good accuracy, while the maximum discharge remains essentially unchanged.

The robustness of the model is tested by comparing the simulated runoff peak times and the timing of debris/hyperconcentrated flow occurred in two neighbouring monitored catchments. Differences in timing result in few minutes, ensuring a reasonably good predictability of the model.

There is still some rooms of improvement in the model. The assessment of direct runoff, not subject to the Hortonian law, by using the SCS-CN method

is not completely representative of the real processes. Furthermore, the rate of change of the infiltration rate with antecedent moisture condition is adequately understood only for AMC I events, remaining not completely clear for AMC II and III events, that, on the other hand, were very few.

In any case, the present dataset is a unique opportunity to test any other hydrological model for providing a plausible input to debris flow models. Moreover, results achieved by the present work can be extended to similar mountain watersheds that, due to their morphology, are ungauged.

References

Agnese, C., Baiamonte, G., and Corrao, C. (2001). A simple model of hillslope response for overland flow generation. *Hydrological Processes*, 15(17):3225–3238.

Aleotti, P. (2004). A warning system for rainfall-induced shallow failures. *Engineering Geology*, 73(3-4):247–265.

Anderson, M. G. and Burt, T. P. (1978). The role of topography in controlling throughflow generation. *Earth Surface Processes*, 3(4):331–344.

Armanini, A., Fraccarollo, L., and Rosatti, G. (2009). Two-dimensional simulation of debris flows in erodible channels. *Computers and Geosciences*, 35(5):993–1006.

Armento, M. C., Genevois, R., and Tecca, P. R. (2008). Comparison of numerical models of two debris flows in the Cortina d' Ampezzo area, Dolomites, Italy. *Landslides*, 5(1):143–150.

Bacchini, M. and Zannoni, A. (2003). Relations between rainfall and triggering of debris-flow: case study of Cancia (Dolomites, Northeastern Italy). *Natural Hazards and Earth System Science*, 3(1/2):71–79.

Bardou, E., Ancey, C., Bonnard, C., and Vulliet, L. (2003). Classification of debris-flow deposits for hazard assessment in alpine areas. *3th International Conference on Debris-Flow hazards mitigation : mechanics, prediction, and assessment*.

Berger, C., McArdell, B. W., Fritschi, B., and Schlunegger, F. (2010). A novel method for measuring the timing of bed erosion during debris flows and floods. *Water Resources Research*, 46(2):n/a–n/a.

Berger, C., McArdell, B. W., and Schlunegger, F. (2011). Sediment transfer patterns at the Illgraben catchment, Switzerland: Implications for the time scales of debris flow activities. *Geomorphology*, 125(3):421–432.

Berti, M., Genevois, R., LaHusen, R. G., Simoni, A., and Tecca, P. R. (2000). Debris flow monitoring in the Acquabona watershed on the Dolomites (Italian alps). *Physics and Chemistry of the Earth, Part B: Hydrology, Oceans and Atmosphere*, 25(9):707–715.

Berti, M., Genevois, R., Simoni, A., and Tecca, P. R. (1999). Field observations of a debris flow event in the Dolomites. *Geomorphology*, 29:265–274.

Berti, M. and Simoni, A. (2005). Experimental evidences and numerical modelling of debris flow initiated by channel runoff. *Landslides*, 2(3):171–182.

Beven, K. J. (2002). Runoff generation in semi-arid areas. In Bull, L. and Kirkby, M. J., editors, *Dryland Rivers: Hydrology and Geomorphology of Semi-arid Channels*, chapter 3, pages 57 – 105. Wiley.

Borga, M., Anagnostou, E. N., Blöschl, G., and Creutin, J.-D. (2010). Flash floods: Observations and analysis of hydro-meteorological controls. *Journal of Hydrology*, 394(1-2):1–3.

Botter, G. and Rinaldo, A. (2003). Scale effect on geomorphologic and kinematic dispersion. *Water Resources Research*, 39(10).

Bouvier, C., Brunet, P., LeBourgeois, O., Nguyen, S., Borrell, V., Ayral, P.-A., Didon-Lescot, J.-F., Domergue, J.-M., and Grard, N. (2015). Hydrological processes generating flash floods at hillslope scale in a small mountainous Mediterranean catchment. *EGU General Assembly 2015*.

Bovis, M. J. and Jakob, M. (1999). The role of debris supply conditions in predicting debris flow activity. *Earth Surface Processes and Landforms*, 24(11):1039–1054.

Brayshaw, D. and Hassan, M. A. (2009). Debris flow initiation and sediment recharge in gullies. *Geomorphology*, 109(3-4):122–131.

Brunetti, M. T., Peruccacci, S., Rossi, M., Luciani, S., Valigi, D., and Guzzetti, F. (2010). Rainfall thresholds for the possible occurrence of landslides in Italy. *Natural Hazards and Earth System Science*, 10(3):447–458.

Caine, N. (1980). The Rainfall Intensity: Duration Control of Shallow Landslides and Debris Flows. *Geografiska Annaler. Series A, Physical Geography*, 62(1/2):23.

Cannon, S. H., Gartner, J. E., Rupert, M. G., Michael, J. A., Rea, A. H., and Parrett, C. (2010). Predicting the probability and volume of postwildfire debris flows in the intermountain western United States. *Geological Society of America Bulletin*, 122(1-2):127–144.

Cannon, S. H., Gartner, J. E., Wilson, R. C., Bowers, J. C., and Laber, J. L. (2008). Storm rainfall conditions for floods and debris flows from recently burned areas in southwestern Colorado and southern California. *Geomorphology*, 96(3-4):250–269.

Chow, V. T., Maidment, D. R., and Mays, L. W. (1988). *Applied Hydrology*. McGraw-Hill, New York.

Coe, J. A. and Godt, J. W. (2003). Estimating debris-flow probability using fan stratigraphy, historic records, and drainage-basin morphology, Interstate 70 highway corridor, central Colorado, U.S.A. *Debris-Flow Hazards Mitigation: Mechanics, Prediction, and Assessment*, pages 1085–1096.

Coe, J. A., Kinner, D. A., and Godt, J. W. (2008). Initiation conditions for debris flows generated by runoff at Chalk Cliffs, central Colorado. *Geomorphology*, 96(3-4):270–297.

Costa, J. E. (1984). Physical Geomorphology of Debris Flows. In *Developments and Applications of Geomorphology*, pages 268–317. Springer Berlin Heidelberg, Berlin, Heidelberg.

Creutin, J.-D. and Borga, M. (2003). Radar hydrology modifies the monitoring of flash-flood hazard. *Hydrological Processes*, 17(7):1453–1456.

Croke, B. and Norton, J. (2004). Regionalisation of Rainfall-Runoff Models. In Pahl-Wostl, C., Schmidt, S., Rizzoli, A., and Jakeman, T., editors, *2nd Biennial Meeting of the International Environmental Modelling and Software Society*, number 3, pages 1201–1207, Manno, Switzerland.

Crosta, G. B. and Frattini, P. (2000). Rainfall thresholds for soil slip and debris flow triggering. In Mugnai, A., Guzzetti, F., and Roth, G., editors, *Proceedings of the EGS 2nd Plinius Conference on Mediterranean Storms*, number 1, pages 463–488, Siena, Italy.

Crosta, G. B. and Frattini, P. (2003). Distributed modelling of shallow landslides triggered by intense rainfall. *Natural Hazards and Earth System Science*, 3(1/2):81–93.

Cruden, D. M. and Varnes, D. J. (1996). Landslide types and processes. In *Landslides: Investigation and Mitigation - Special Report*, number 247, chapter 3, pages 36–75. Transportation Research Board.

Cunge, J. (1969). On The Subject Of A Flood Propagation Computation Method (Musklngum Method). *Journal of Hydraulic Research*, 7(2):205–230.

D'Asaro, F. and Grillone, G. (2012). Empirical Investigation of Curve Number Method Parameters in the Mediterranean Area. *Journal of Hydrologic Engineering*, 17(10):1141–1152.

Davies, T. R. H. (1988). *Debris flow surges: a laboratory investigation*. Number 96. Zurich.

De Paola, F., De Risi, R., Di Crescenzo, G., Giugni, M., Santo, A., and Speranza, G. (2017). Probabilistic Assessment of Debris Flow Peak Discharge by Monte Carlo Simulation. *ASCE-ASME Journal of Risk and Uncertainty in Engineering Systems, Part A: Civil Engineering*, 3(1):A4015002.

Deganutti, A. M. and Tecca, P. R. (2013). The Case Study of Cancia (Dolomites, Italy), a Mountain Village Threatened by a Debris Flow. In *Landslide Science and Practice*, pages 329–333. Springer Berlin Heidelberg, Berlin, Heidelberg.

Degetto, M., Gregoretti, C., and Bernard, M. (2015). Comparative analysis of the differences between using LiDAR and contour-based DEMs for hydrological modeling of runoff generating debris flows in the Dolomites. *Frontiers in Earth Science*, 3(June):1–15.

Di Lazzaro, M. (2008). Correlation between channel and hillslope lengths and its effects on the hydrologic response. *Journal of Hydrology*, 362(3-4):260–273.

D'Odorico, P. and Rigon, R. (2003). Hillslope and channel contributions to the hydrologic response. *Water Resources Research*, 39(5).

Easterling, D. R., Evans, J. L., Groisman, P. Y., Karl, T. R., Kunkel, K. E., and Ambenje, P. (2000). Observed variability and trends in extreme climatic events: a brief review. *Bulletin of The American Meteorological Society*, 81:417–425.

Ebel, B. A., Loague, K., Dietrich, W. E., Montgomery, D. R., Torres, R., Anderson, S. P., and Giambelluca, T. W. (2007a). Near-surface hydrologic response for steep, unchanneled catchment near Coos Bay, Oregon: 1. Sprinkling experiments. *American Journal of Science*, 307(4):678–708.

Ebel, B. A., Loague, K., Vanderkwaak, J. E., Dietrich, W. E., Montgomery, D. R., Torres, R., and Anderson, S. P. (2007b). Near-surface hydrologic response for steep, unchanneled catchment near Coos Bay, Oregon: 2. Physics-based simulations. *American Journal of Science*, 307(4):709–748.

Eli, R. N. and Lamont, S. J. (2010). Curve Numbers and Urban Runoff ModelingApplication Limitations. In *Low Impact Development 2010*, pages 405–418, Reston, VA. American Society of Civil Engineers.

Floris, M., D'Alpaos, A., Squarzoni, C., Genevois, R., and Marani, M. (2010). Recent changes in rainfall characteristics and their influence on thresholds for debris flow triggering in the Dolomitic area of Cortina d'Ampezzo, northeastern Italian Alps. *Natural Hazards and Earth System Science*, 10(3):571–580.

Foglia, L., Hill, M. C., Mehl, S. W., and Burlando, P. (2009). Sensitivity analysis, calibration, and testing of a distributed hydrological model using error-based weighting and one objective function. *Water Resources Research*, 45:1–18.

Fowler, H. J. and Kilsby, C. G. (2003). Implications of changes in seasonal and annual extreme rainfall. *Geophysical Research Letters*, 30(13):1720.

Frank, F., McArdell, B. W., Huggel, C., and Vieli, A. (2015). The importance of entrainment and bulking on debris flow runout modeling: examples from the Swiss Alps. *Natural Hazards and Earth System Sciences*, 15(11):2569–2583.

Frei, C. and Schär, C. (2001). Detection probability of trends in rare events: Theory and application to heavy precipitation in the Alpine region. *Journal of Climate*, 14(7):1568–1584.

Garbrecht, J., Ogden, F. L., DeBarry, P. A., and Maidment, D. R. (2001). GIS and Distributed Watershed Models. I: Data Coverages and Sources. *Journal of Hydrologic Engineering*, 6(6):506–514.

Genevois, R., Tecca, P. R., Berti, M., and Simoni, A. (2000). Pore pressure distribution in the initiation area of a granular debris flow. In Bromhead, E., Dixon, N., and Ibsen, M., editors, *Proceedings of the 8th International Symposium on Landslides*, pages 615–620, Cardiff, UK.

Germann, U., Galli, G., Boscacci, M., and Bolliger, M. (2006). Radar precipitation measurement in a mountainous region. *Quarterly Journal of the Royal Meteorological Society*, 132(618):1669–1692.

Godt, J. W., Baum, R. L., and Chleborad, A. F. (2006). Rainfall characteristics for shallow landsliding in Seattle, Washington, USA. *Earth Surface Processes and Landforms*, 31(1):97–110.

Godt, J. W. and McKenna, J. P. (2008). Numerical modeling of rainfall thresholds for shallow landsliding in the Seattle, Washington, area. In Baum, R. L., Godt, J. W., and Highland, L. M., editors, *Landslides and Engineering Geology of the Seattle, Washington, Area - Geological Society of America Reviews in Engineering Geology*, volume XX, chapter 07, pages 121–135. Geological Society of America.

Gregoretti, C., Adams, M. S., Hagen, K., Laigle, D., Liébault, F., Degetto, M., Andrich, A., and Tiranti, D. (2012). Forecast System Guidelines - Debris Flow. Guidelines for the implementation of Forecast System against debris flow hazard (WP6). Projekt Alpine Space - Paramount. Technical report, European Regional Development Fund, Bruxelles.

Gregoretti, C. and Dalla Fontana, G. (2007). Rainfall threshold for the initiation of debris flows by channel-bed failure in the Dolomites. In Chen, C. and Major, J. J., editors, *Debris-flow mitigation: mechanics, prediction and assessment*, pages 11–21. Milpress.

Gregoretti, C. and Dalla Fontana, G. (2008). The triggering of debris flow due to channel-bed failure in some alpine headwater basins of the Dolomites: analyses of critical runoff. *Hydrological Processes*, 22(13):2248–2263.

Gregoretti, C., Degetto, M., and B oreggio, M. (2016a). GIS-based cell model for simulating debris flow runout on a fan. *Journal of Hydrology*, 534:326–340.

Gregoretti, C., Degetto, M., Bernard, M., Crucil, G., Pimazzoni, A., De Vido, G., Berti, M., Simoni, A., and Lanzoni, S. (2016b). Runoff of small rocky headwater catchments: Field observations and hydrological modeling. *Water Resources Research*, 52(10):8138–8158.

Gregoretti, C., Maltauro, A., and Lanzoni, S. (2010). Laboratory Experiments on the Failure of Coarse Homogeneous Sediment Natural Dams on a Sloping Bed. *Journal of Hydraulic Engineering*, 136(11):868–879.

Grimaldi, S., Petroselli, A., and Nardi, F. (2012). A parsimonious geomorphological unit hydrograph for rainfallrunoff modelling in small ungauged basins. *Hydrological Sciences Journal*, 57(1):73–83.

Grimaldi, S., Petroselli, A., and Romano, N. (2013). Green-Ampt Curve-Number mixed procedure as an empirical tool for rainfall-runoff modelling in small and ungauged basins. *Hydrological Processes*, 27(8):1253–1264.

Guzzetti, F., Peruccacci, S., Rossi, M., and Stark, C. P. (2007). Rainfall thresholds for the initiation of landslides in central and southern Europe. *Meteorology and Atmospheric Physics*, 98(3-4):239–267.

Guzzetti, F., Peruccacci, S., Rossi, M., and Stark, C. P. (2008). The rainfall intensity-duration control of shallow landslides and debris flows: An update. *Landslides*, 5(1):3–17.

Han, X., Chen, J., Xu, P., and Zhan, J. (2017). A well-balanced numerical scheme for debris flow run-out prediction in Xiaojia Gully considering different hydrological designs. *Landslides*, (June):1–10.

Hawkins, R. H., Ward, T. J., Woodward, D. E., and Van Mullem, J. A., editors (2008). *Curve Number Hydrology*. American Society of Civil Engineers, Reston, VA.

Hawkins, R. H., Ward, T. J., Woodward, E., and Van Mullem, J. a. (2010). Continuing evolution of rainfall-runoff and the curve number precedent. *2nd Joint Federal Interagency Conference*, pages 2–12.

Horton, R. E. (1938). The interpretation and application of runoff plot experiments with reference to soil erosion problems. In *Soil Science Society of America Proceedings*, volume 3, pages 340–349.

Hungr, O., Evans, S. G., Bovis, M. J., and Hutchinson, J. N. (2001). A review of the classification of landslides of the flow type. *Environmental & Engineering Geoscience*, 7(3):221–238.

Hungr, O., Leroueil, S., and Picarelli, L. (2014). The Varnes classification of landslide types, an update. *Landslides*, 11(2):167–194.

Hürlimann, M., Abancó, C., Moya, J., and Vilajosana, I. (2014). Results and experiences gathered at the Rebaixader debris-flow monitoring site, Central Pyrenees, Spain. *Landslides*, 11(6):939–953.

Hürlimann, M., Copons, R., and Altimir, J. (2006). Detailed debris flow hazard assessment in Andorra: A multidisciplinary approach. *Geomorphology*, 78(3-4):359–372.

Hürlimann, M., Rickenmann, D., and Graf, C. (2003). Field and monitoring data of debris-flow events in the Swiss Alps. *Canadian Geotechnical Journal*, 40(1):161–175.

Hutchinson, J. N. (1968). *Mass movement*, pages 688–696. Encyclopedia of Earth Science. Springer Berlin Heidelberg, Dordrecht.

Hutchinson, J. N. (1989). General report: morphological and geotechnical parameters of landslides in relation to geology and hydrogeology: Proc 5th International Symposium on. *International Journal of Rock Mechanics and Mining . . . .*

Innes, J. L. (1983). Debris flows. *Progress in Physical Geography*, 7(4):469–501.

Iverson, R. M. (1997). The physics of debris flows. *Reviews of Geophysics*, 35(3):245.

Iverson, R. M. (2003). The debris-flow rheology myth. *3rd International Conference on Debris-Flow Hazards Mitigation: Mechanics, Prediction, and Assessment*, pages 303–314.

Iverson, R. M. (2005). *Debris-flow mechanics*, pages 105–134. Springer Berlin Heidelberg, Berlin, Heidelberg.

Iverson, R. M., Reid, M. E., Logan, M., LaHusen, R. G., Godt, J. W., and Griswold, J. P. (2011). Positive feedback and momentum growth during debris-flow entrainment of wet bed sediment. *Nature Geoscience*, 4(2):116–121.

Iverson, R. M. and Vallance, J. W. (2001). New views of granular mass flows. *Geology*, 29(2):115.

Jakob, M. (2005). A size classification for debris flows. *Engineering Geology*, 79(3-4):151–161.

Jakob, M. and Hungr, O. (2005). *Debris-flow Hazards and Related Phenomena*. Springer Praxis Books. Springer Berlin Heidelberg, Berlin, Heidelberg.

Johnson, A. and Rodine, J. (1984). Debris flows. *Slope instability*, pages 257–361.

Julien, P. Y. and Paris, A. (2010). Mean Velocity of Mudflows and Debris Flows. *Journal of Hydraulic Engineering*, 136(9):676–679.

Kean, J. W., McCoy, S. W., Tucker, G. E., Staley, D. M., and Coe, J. A. (2013). Runoff-generated debris flows: Observations and modeling of surge initiation, magnitude, and frequency. *Journal of Geophysical Research: Earth Surface*, 118(4):2190–2207.

Kean, J. W., Staley, D. M., and Cannon, S. H. (2011). In situ measurements of post-fire debris flows in southern California: Comparisons of the timing and magnitude of 24 debris-flow events with rainfall and soil moisture conditions. *Journal of Geophysical Research*, 116(F4):F04019.

Kean, J. W., Staley, D. M., Leeper, R. J., Schmidt, K. M., and Gartner, J. E. (2012). A low-cost method to measure the timing of postfire flash floods and debris flows relative to rainfall. *Water Resources Research*, 48(5):n/a–n/a.

Koren, V., Finnerty, B., Schaake, J., Smith, M., Seo, D.-J., and Duan, Q.-Y. (1999). Scale dependencies of hydrologic models to spatial variability of precipitation. *Journal of Hydrology*, 217(3-4):285–302.

Lange, J., Greenbaum, N., Husary, S., Ghanem, M., Leibundgut, C., and Schick, A. P. (2003). Runoff generation from successive simulated rainfalls on a rocky, semi-arid, Mediterranean hillslope. *Hydrological Processes*, 17(2):279–296.

Lanzoni, S., Gregoretti, C., and Stancanelli, L. M. (2017). Coarse-grained debris flow dynamics on erodible beds. *Journal of Geophysical Research: Earth Surface*, 122(3):592–614.

Lauterjung, H. and Schmidt, G. (1989). *Planning of Water intake structures for irrigation or hydropower*. GTZ-Postharvest Project.

Leopold, L. B. and Maddock, T. J. (1953). The Hydraulic Geomtry of Stream Channels and Some Physiographic Implications. *Geological Survey Professional Paper 252*, page 57.

Li, X. Y., Contreras, S., Solé-Benet, A., Cantón, Y., Domingo, F., Lázaro, R., Lin, H., Van Wesemael, B., and Puigdefábregas, J. (2011). Controls of infiltration-runoff processes in Mediterranean karst rangelands in SE Spain. *Catena*, 86(2):98–109.

Lin, X. (1999). Flash floods in arid and semi-arid zones. Technical Report 23, UNESCO, Paris.

Liu, Y. and Gupta, H. V. (2007). Uncertainty in hydrologic modeling: Toward an integrated data assimilation framework.

Mantovani, F., Pasuto, A., and Silvano, S. (2002). Definition of the elements at risk and mitigation measures of the Cancia debris flow (Dolomites, Northeastern Italy). In J. L. van Rooy and C. A. Jermy, editor, *Engineering Geology for Developing Countries 9th Congress of the International Association for Engineering Geology and the Environment*, number 0, pages 1201–1209, Durban, South Africa.

Marchi, L. and D'Agostino, V. (2004). Estimation of debris-flow magnitude in the Eastern Italian Alps. *Earth Surface Processes and Landforms*, 29(2):207–220.

Marchi, L., Dalla Fontana, G., Cavalli, M., and Tagliavini, F. (2008). Rocky Headwaters in the Dolomites, Italy: Field Observations and Topographic Analysis. *Artic, Antartic, and Alpine Research*, 40(4):685–694.

Marra, F., Nikolopoulos, E. I., Creutin, J.-D., and Borga, M. (2014). Radar rainfall estimation for the identification of debris-flow occurrence thresholds. *Journal of Hydrology*, 519:1607–1619.

Masih, I., Maskey, S., Uhlenbrook, S., and Smakhtin, V. (2011). Assessing the Impact of Areal Precipitation Input on Streamflow Simulations Using the SWAT Model1. *JAWRA Journal of the American Water Resources Association*, 47(1):179–195.

McCoy, S. W., Kean, J. W., Coe, J. A., Staley, D. M., Wasklewicz, T. a., and Tucker, G. E. (2010). Evolution of a natural debris flow: In situ measurements of flow dynamics, video imagery, and terrestrial laser scanning. *Geology*, 38(8):735–738.

McDonnell, J. J. and Beven, K. (2014). Debates-The future of hydrological sciences: A (common) path forward? A call to action aimed at understanding velocities, celerities and residence time distributions of the headwater hydrograph. *Water Resources Research*, 50(6):5342–5350.

McGuire, L. A., Rengers, F. K., Kean, J. W., and Staley, D. M. (2017). Debris flow initiation by runoff in a recently burned basin: Is grain-by-grain sediment bulking or en masse failure to blame? *Geophysical Research Letters*, 44(14):7310–7319.

Montanari, A. and Brath, A. (2004). A stochastic approach for assessing the uncertainty of rainfall-runoff simulations. *Water Resources Research*, 40(1).

Montanari, A. and Toth, E. (2007). Calibration of hydrological models in the spectral domain: An opportunity for scarcely gauged basins? *Water Resources Research*, 43(5).

Montgomery, D. R. and Foufoula-Georgiou, E. (1993). Channel network source representation using digital elevation models. *Water Resources Research*, 29(12):3925–3934.

Moody, J. A., Martin, D. A., Haire, S. L., and Kinner, D. A. (2008). Linking runoff response to burn severity after a wildfire. *Hydrological Processes*, 22(13):2063–2074.

Moser, M. and Hohensinn, F. (1983). Geotechnical aspects of soil slips in Alpine regions. *Engineering Geology*, 19(3):185–211.

Nikolopoulos, E. I., Destro, E., Maggioni, V., Marra, F., and Borga, M. (2017). Satellite Rainfall Estimates for Debris Flow Prediction: An Evaluation Based on Rainfall AccumulationDuration Thresholds. *Journal of Hydrometeorology*, 18(8):2207–2214.

Onda, Y., Tsujimura, M., Fujihara, J.-i., and Ito, J. (2006). Runoff generation mechanisms in high-relief mountainous watersheds with different underlying geology. *Journal of Hydrology*, 331(3-4):659–673.

Orlandini, S. and Lamberti, A. (2000). Effect of Wind on Precipitation Intercepted by Steep Mountain Slopes. *Journal of Hydrologic Engineering*, 5(4):346–354.

Orlandini, S. and Morlini, I. (2000). Artificial neural network estimation of rainfall intensity from radar observations. *Journal of Geophysical Research: Atmospheres*, 105(D20):24849–24861.

Orlandini, S. and Rosso, R. (1996). Diffusion Wave Modeling of Distributed Catchment Dynamics. *Journal of Hydrologic Engineering*, 1(3):103–113.

Peruccacci, S., Brunetti, M. T., Gariano, S. L., Melillo, M., Rossi, M., and Guzzetti, F. (2017). Rainfall thresholds for possible landslide occurrence in Italy. *Geomorphology*, 290(January):39–57.

Ponce, V. M. (1991). Kinematic Wave Controversy. *Journal of Hydraulic Engineering*, 117(4):511–525.

Pudasaini, S. P. (2012). A general two-phase debris flow model. *Journal of Geophysical Research*, 117(F3):F03010.

Quinn, P., Beven, K., Chevallier, P., and Planchon, O. (1991). The prediction of hillslope flow paths for distributed hydrological modelling using digital terrain models. *Hydrological Processes*, 5(1):59–79.

Reid, M. E., LaHusen, R. G., and Iverson, R. M. (1997). Debris-Flow Initiation Experiments Using Diverse Hydrologic Triggers. *Debris-Flow Hazards Mitigation: Mechanics, Prediction and Assessment*, pages 1–11.

Remaître, A., Malet, J. P., Maquaire, O., Ancey, C., and Locat, J. (2005). Flow behaviour and runout modelling of a complex debris flow in a clay-shale basin. *Earth Surface Processes and Landforms*, 30(4):479–488.

Rengers, F. K., McGuire, L. A., Kean, J. W., Staley, D. M., and Hobley, D. E. J. (2016). Model simulations of flood and debris flow timing in steep catchments after wildfire. *Water Resources Research*, 52(8):6041–6061.

Rickenmann, D. (1999). Empirical relationships for debris flows. *Natural Hazards*, 19(1):47–77.

Rickenmann, D., Laigle, D., McArdell, B. W., and Hübl, J. (2006). Comparison of 2D debris-flow simulation models with field events. *Computational Geosciences*, 10(2):241–264.

Rickenmann, D. and Zimmermann, M. (1993). The 1987 debris flows in Switzerland: documentation and analysis. *Geomorphology*, 8(2-3):175–189.

Rinaldo, A., Marani, A., and Rigon, R. (1991). Geomorphological dispersion. *Water Resources Research*, 27(4):513–525.

Robinson, J. S., Sivapalan, M., and Snell, J. D. (1995). On the relative roles of hillslope processes, channel routing, and network geomorphology in the hydrologic response of natural catchments. *Water Resources Research*, 31(12):3089–3101.

Rodríguez-Iturbe, I. and Valdés, J. B. (1979). The geomorphologic structure of hydrologic response. *Water Resources Research*, 15(6):1409–1420.

Saco, P. M. and Kumar, P. (2002a). Kinematic dispersion in stream networks 1. Coupling hydraulic and network geometry. *Water Resources Research*, 38(11):26–1–26–14.

Saco, P. M. and Kumar, P. (2002b). Kinematic dispersion in stream networks 2. Scale issues and self-similar network organization. *Water Resources Research*, 38(11):27–1–27–15.

Saco, P. M. and Kumar, P. (2004). Kinematic dispersion effects of hillslope velocities. *Water Resources Research*, 40(1).

Salciarini, D., Tamagnini, C., Conversini, P., and Rapinesi, S. (2012). Spatially distributed rainfall thresholds for the initiation of shallow landslides. *Natural Hazards*, 61:229–245.

Sattler, K., Keiler, M., Zischg, A., and Schrott, L. (2011). On the Connection between Debris Flow Activity and Permafrost Degradation: A Case Study from the Schnalstal, South Tyrolean Alps, Italy. *Permafrost and Periglacial Processes*, 22(3):254–265.

Schaefer, J. T. (1990). The Critical Success Index as an Indicator of Warning Skill. *Weather and Forecasting*, 5(4):570–575.

Schulz, K., Beven, K., and Huwe, B. (1999). Equifinality and the problem of robust calibration in nitrogen budget simulations. *Soil Science Society of America Journal*, 63(6):1934–1941.

Seibert, J. and Beven, K. J. (2009). Gauging the ungauged basin: how many discharge measurements are needed? *Hydrology and Earth System Sciences Discussions*, 6(2):2275–2299.

Shannon, J., Richardson, R., and Thornes, J. (2002). Modelling event-based uxes in Ephemeral streams. In Bull, J. and Kirkby, M. J., editors, *Dryland Rivers: Hydrology and Geomorphology*, pages 129–172. John Wiley, Chichester, UK.

Sheridan, G. J., Lane, P. N., and Noske, P. J. (2007). Quantification of hillslope runoff and erosion processes before and after wildfire in a wet Eucalyptus forest. *Journal of Hydrology*, 343(1-2):12–28.

Sherman, L. R. K. (1932). The relation of hydrographs of runoff to size and character of drainage-basins. *Eos, Transactions American Geophysical Union*, 13(1):332–339.

Sillmann, J. and Roeckner, E. (2008). Indices for extreme events in projections of anthropogenic climate change. *Climatic Change*, 86(1-2):83–104.

Sivapalan, M. (1993). Linking hydrologic parameterizations across a range of scales: hillslope to catchment to region. In *Exchange processes at the land surface for a range of space and time scales. Proc. international symposium*, pages 115–123, Yokohama. IAHS; Publication, 212.

Soil Conservation Service (1972). National Engineering Handbook (NEH4). Technical report, U.S. Department of Agriculture, Washington DC.

Staley, D. M., Kean, J. W., Cannon, S. H., Schmidt, K. M., and Laber, J. L. (2013). Objective definition of rainfall intensity-duration thresholds for the initiation of post-fire debris flows in southern California. *Landslides*, 10(5):547–562.

Staley, D. M., Negri, J. A., Kean, J. W., Laber, J. L., Tillery, A. C., and Youberg, A. M. (2017). Prediction of spatially explicit rainfall intensityduration thresholds for post-fire debris-flow generation in the western United States. *Geomorphology*, 278:149–162.

Takahashi, T. (2007). *Debris Flow: Mechanics, Prediction and Countermeasures*. CRC Press.

Takahashi, T. (2009). A Review of Japanese Debris Flow Research. *International Journal of Erosion Control Engineering*, 2(1):1–14.

Tarboton, D. G. (1997). A new method for the determination of flow directions and upslope areas in grid digital elevation models. *Water Resources Research*, 33(2):309–319.

Taylor, J. R. (1997). *Introduction to Error Analysis - the Study of Uncertainties in Physical Measurements*. University Science Books, Sausalito, CA, USA, 2nd edition.

Tecca, P. R., Galgaro, A., Genevois, R., and Deganutti, A. M. (2003). Development of a remotely controlled debris flow monitoring system in the Dolomites (Acquabona, Italy). *Hydrological Processes*, 17(9):1771–1784.

Tecca, P. R. and Genevois, R. (2009). Field observations of the June 30, 2001 debris flow at Acquabona (Dolomites, Italy). *Landslides*, 6(1):39–45.

Theule, J. I., Liébault, F., Loye, a., Laigle, D., and Jaboyedoff, M. (2012). Sediment budget monitoring of debris-flow and bedload transport in the Manival Torrent, SE France. *Natural Hazards and Earth System Science*, 12(3):731–749.

Tiranti, D. and Deangeli, C. (2015). Modeling of debris flow depositional patterns according to the catchment and sediment source area characteristics. *Frontiers in Earth Science*, 3(March):1–14.

Turner, A. K. and Schuster, R. L. (1996). *Landslides: investigation and mitigation.* Number 247. National Academy Press, Washinton.

Uchida, T., Tromp-van Meerveld, I., and McDonnell, J. J. (2005). The role of lateral pipe flow in hillslope runoff response: an intercomparison of non-linear hillslope response. *Journal of Hydrology*, 311(1-4):117–133.

Underwood, S. J., Schultz, M. D., Berti, M., Gregoretti, C., Simoni, A., Mote, T. L., and Saylor, A. M. (2016). Atmospheric circulation patterns, cloud-to-ground lightning, and locally intense convective rainfall associated with debris flow initiation in the Dolomite Alps of northeastern Italy. *Natural Hazards and Earth System Sciences*, 16(2):509–528.

Varnes, D. J. (1978). Slope movement types and processes. In Schuster, R. L. and Krizek, R. J., editors, *Landslides -Analysis and Control - Transportation Research Board Special Report*, number 176, chapter 2, pages 11–33. National Academy of Science, Washington DC.

Wagener, T., Boyle, D. P., Lees, M. J., Wheater, H. S., Gupta, H. V., and Sorooshian, S. (2001). A framework for development and application of hydrological models. *Hydrology and Earth System Sciences*, 5(1):13–26.

Wagener, T. and Montanari, A. (2011). Convergence of approaches toward reducing uncertainty in predictions in ungauged basins. *Water Resources Research*, 47(6):W06301.

Wei, Z., Shang, Y., Zhao, Y., Pan, P., and Jiang, Y. (2017). Rainfall threshold for initiation of channelized debris flows in a small catchment based on in-site measurement. *Engineering Geology*, 217:23–34.

Wilson, E. (1990). *Engineering hydrology.* MacMillan, London.

Wooding, R. (1965). A hydraulic model for the catchment-stream problem: II. Numerical solutions. *Journal of Hydrology*, 3(3-4):268–282.

Woolhiser, D. A. and Liggett, J. A. (1967). Unsteady, one-dimensional flow over a plane-The rising hydrograph. *Water Resources Research*, 3(3):753–771.

Zoccatelli, D., Borga, M., Viglione, A., Chirico, G. B., and Blöschl, G. (2011). Spatial moments of catchment rainfall: rainfall spatial organisation, basin morphology, and flood response. *Hydrology and Earth System Sciences*, 15(12):3767–3783.

Appendix A

Building-up and maintenance of the sharp-crested weir facility

A.1 Summer 2011

Figure A.1: Selection of the rocky channel for the setting up of sharp-crested weir (25$^{\text{th}}$ of June 2011) and emptying.

Figure A.2: Sharp-crested weir construction: initial operations (August 2011).

Figure A.3: Setting down of the cable of the pressure transducers to be placed upstream the sharp-crested weir.

Figure A.4: Building of the facility (August 2011): rock cutting for positioning the steel plate.

Figure A.5: Building of the facility (August 2011): preparation of the upstream basin.

A.2   Summer 2013

Figure A.6: Removal of the huge boulder obstructing the facility. On the left, the situation found after the rockfall occurred on August 2011; the central panel shows the drilling of the huge boulder above the stilling basin for using the expansive mortar; on the right, the cracked boulder, before removal.

Figure A.7: Consolidation of the torrent bed. On the left, the channel after the removal of the huge boulder; on the right, the dug channel before building the gabions upstream the stilling basin.

Figure A.8: Re-positioning of the sharp crested weir. The upper panel exhibits the building-up of the gabions upstream the stilling basin. The lower panels show the finished stilling basin, without/with the sharp-crested weir (respectively on the left and the right).

A.3   Summer 2014

Figure A.9: Monitoring station after the repeated snow avalanches occurred during Winter 2014.

A.4 Summer 2015

Figure A.10: Stilling basin after the sediment transport events occurred on June 7th (upper panel), and on July 29th, 2015 (lower panel).

A.5   Summer 2016

Figure A.11: Stilling basin before starting the monitoring season on 2016 (upper and central panel). In the lower panel, the restoration of the facility, with the replacement of the damaged sharp-crested weir.